



HAL
open science

Fluid-structure interaction in human vocal folds

Petr Sidlof

► **To cite this version:**

Petr Sidlof. Fluid-structure interaction in human vocal folds. Sciences de l'ingénieur [physics]. ENSTA ParisTech, 2007. Français. NNT: . pastel-00002366

HAL Id: pastel-00002366

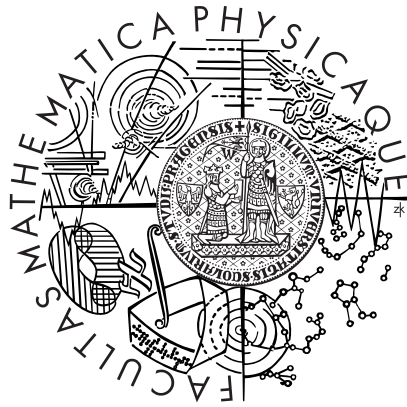
<https://pastel.hal.science/pastel-00002366>

Submitted on 18 Apr 2007

HAL is a multi-disciplinary open access archive for the deposit and dissemination of scientific research documents, whether they are published or not. The documents may come from teaching and research institutions in France or abroad, or from public or private research centers.

L'archive ouverte pluridisciplinaire **HAL**, est destinée au dépôt et à la diffusion de documents scientifiques de niveau recherche, publiés ou non, émanant des établissements d'enseignement et de recherche français ou étrangers, des laboratoires publics ou privés.

CHARLES UNIVERSITY IN PRAGUE
FACULTY OF MATHEMATICS AND PHYSICS



Fluid-structure interaction in human vocal folds

(PhD thesis)

Petr Šidlof

Department of Numerical Mathematics

Head of department: Doc. RNDr. Vít Dolejší, Ph.D.

Branch: Scientific and technical calculations

Supervisor: Ing. Jaromír Horáček, DrSc.

(Institute of Thermomechanics, Academy of Sciences of the Czech Republic)

Consultant: Prof. RNDr. Miloslav Feistauer, DrSc., dr. h. c.

(Department of Numerical Mathematics, Faculty of Mathematics and Physics of the Charles University in Prague)

I would like to express many thanks to my supervisor Jaromír Horáček for his skilled advice and suggestions, reading of the manuscript and above all for his kind and helpful approach during the supervision of this work. I am also very grateful to Miloslav Feistauer and to Petr Sváček, who provided me with valuable information, help and comments.

A great deal of the work was done during my one-year research stay at École Nationale Supérieure de Techniques Avancées, Paris. I owe much to Antoine Chaigne, who organized all the scientific and administrative aspects of the project. The cooperation with the scientists and personnel from ENSTA, namely Olivier Doaré, Olivier Cadot, Lahcène Cherfa, Eric Lunéville, Colin Chambeyron, Nicolas Baudet and Thierry Pichon was an extremely rewarding and pleasant experience.

My special thanks go to Petra Nováková for the English corrections, to my sister Terezie Šidlofová for the text revisions and to Katka Záhorová and to all my family for their patience and support.

The research was supported by the Grant Agency of the Academy of Sciences of the Czech Republic by Project No. IAA2076401 *Mathematical modeling of human vocal fold oscillations*.

The stay at ENSTA Paris was co-financed by the Mobility Funds of Charles University, by the French Ministry of Foreign Affairs and French Ministry of Defense.

I declare that this PhD thesis is my own work and that I cited all the used references. The document can be freely reproduced for educational purposes.

Prague, February 26, 2007

Petr Šidlof

Abstract

The velocity and pressure fields in the proximity of the vocal folds were studied by means of numerical modeling and experimental investigation. The mathematical model, based on the 2D incompressible Navier-Stokes equations in arbitrary Lagrangian-Eulerian formulation discretized by the finite element method, was programmed in the Fortran language, using numerical library Mélima. The results of the numerical simulations show the development of the supraglottal jet and evolution of the recirculation vortices within one vocal fold oscillation cycle. The physical model, scaled 4 : 1, yields the acceleration, supraglottal pressure and acoustic signals emitted by an elastic body vibrating in the wall of a wind tunnel due to coupling with the flow. The velocity fields in the supraglottal domain were measured on this model by a PIV system synchronized with the vibration.

Résumé

Le champ de vitesse et de pression le long des cordes vocales vibrantes était étudié à l'aide d'un modèle numérique et par observation expérimentale. Le modèle mathématique, basé sur les équations de Navier-Stokes 2D incompressibles discrétisées avec la méthode des éléments finis en formulation d'Euler-Lagrange arbitraire, était programmé dans le langage Fortran, à l'aide de la librairie numérique Mélima. Dans les résultats des simulations numériques on peut observer le développement du jet derrière la glotte et l'évolution des tourbillons de recirculation lors du cycle d'oscillation des cordes vocales. Le modèle physique en échelle 4 : 1 fournit les signaux d'accélération, pression supraglottale et le signal acoustique émis par un corps élastique, qui vibre dans le paroi du canal aérodynamique grâce au couplage avec l'écoulement. Sur le même modèle, le champ de vitesse dans le domaine supraglottale était mesuré par la PIV synchronisée avec les oscillations.

Abstrakt

Pomocí numerického modelu a měření na fyzikálním modelu byla zkoumána rychlostní a tlaková pole v blízkosti kmitajících hlasivek. Matematický model, založený na 2D nestlačitelných Navier-Stokesových rovnicích diskretizovaných metodou konečných prvků ve formulaci ALE (Arbitrary Lagrange-Euler), byl implementován v jazyce Fortran, při využití numerické knihovny Mélima. Výsledky numerických simulací ukazují vývoj proudění v hlasivkové štěrbině a vznik recirkulačních vírů během periody kmitání hlasivek. Na fyzikálním modelu v měřítku 4 : 1 bylo naměřeno zrychlení, subglotický tlak a akustický signál vyzařovaný za pružným tělesem kmitajícím ve stěně aerodynamického kanálu díky interakci s proudícím vzduchem. Na stejném modelu byla vyhodnocena rychlostní pole v supraglotické oblasti metodou PIV synchronizovanou s kmitáním hlasivky.

Contents

1	Introduction	7
1.1	Principles of voice production	8
1.2	Objectives of the study	9
1.3	Overview of existing vocal fold models	11
2	Mathematical modeling	12
2.1	Mathematical description	14
2.1.1	Equations of motion of the mechanical system	14
2.1.2	Formulation of the coupled problem	17
2.1.3	Arbitrary Lagrangian-Eulerian method	18
2.1.4	Navier-Stokes equations in ALE formulation	21
2.1.5	Initial and boundary conditions	24
2.1.6	Dimensionless variables	25
2.2	Numerical solution	27
2.2.1	Solution of the coupled problem	27
2.2.2	Time discretization of the Navier-Stokes equations	29
2.2.3	Linearization of the convective term - Oseen iterations	30
2.2.4	Weak formulation of the Navier-Stokes equations	31
2.2.5	FE discretization of the Navier-Stokes equations	35
2.2.6	ALE mapping	38
2.2.7	Mesh generation and adaptive refinement	39
2.2.8	Algorithmic and technical remarks	40
2.3	Results	43

3	Experimental investigation	52
3.1	Principles of Particle Image Velocimetry	53
3.2	Concept and design of the physical vocal fold model	54
3.3	Experimental setup	58
3.4	Results of the dynamic and acoustic measurements	62
3.5	Results of the PIV measurements	70
4	Discussion and conclusions	81
	References	84

Chapter 1

Introduction

At the current speed of technology progress, fluid-structure interaction affects an increasing number of technical applications – airfoil and helicopter rotor blade vibration, stability of suspension bridges, towers, smokestacks and skyscrapers, vibration of turbine blades or flow in heat exchangers and nuclear reactors. Thorough investigations of catastrophic disasters caused by wind-induced vibrations, such as ruptures of aircraft wings, collapse of the Tacoma Narrows bridge on November 7, 1940 or breakdown of the cooling towers in Ferrybridge on November 1, 1965 lead to the development of a new scientific and technical discipline: the aeroelasticity.

The aeroelastic calculations need to combine the methods of three classical branches of mechanics: dynamics of rigid bodies and structures, fluid dynamics and elasticity. In the majority of cases, the consequences of the aeroelastic effects are rather undesirable – the flow-induced vibration may affect negatively the operation of the systems, lead to material fatigue or induce excessive noise generation. However, there are processes where the fluid-structure interaction plays a crucial role; this is the case of voice production in human vocal folds, which is the subject of this thesis.

Since the complete equations describing aeroelastic processes are extremely difficult to solve, a classical approach in aeroelasticity is to reduce the mechanical part of the problem into a small system of rigid masses, springs and dampers, which is further coupled with a simplified flow model. The models often comprise semiempirical relations and constants. An illustrative case study is demonstrated in Dowel's monography [10]: the airfoil instability is studied using a model which consists of a rigid plate fixed on a torsion spring, subjected to flow described by the Bernoulli equation. Although such methods are still widely used and make part of standardized and state-certified procedures e.g. in civil engineering, aeronautics and space applications, some more complex techniques have also been employed in recent years. These are related mainly to the boom of finite element and finite volume codes, which allow realistic modeling both of the flow and of the elastic deformations. Mathematical modeling of the flow in human vocal folds using the finite element method, as well as measurements on a self-vibrating mechanical vocal fold model, will be addressed within this thesis.

When modeling flow-induced vocal fold oscillation, it is indispensable to understand the basic principles of voice production in humans and to acquire a basic knowledge about physiological structures involved. Hence, the most important facts are summarized in the following introductory section.

1.1 Principles of voice production

The human voice is created by passage of the airflow between vocal folds, which are located in the upper part of larynx (see Fig. 1.1, left). The vocal folds (formerly called vocal cords) are two symmetric soft tissue structures fixed between the thyroid cartilage and arytenoid cartilages (which are paired); basically they are composed of the thyroarytenoid (TA) muscle and ligament covered by mucosa (see Fig. 1.1, right). In fact, this three-layer model of vocal folds is only a simplified description; more detailed information can be found e.g. in Titze’s monographs [45] or [46]. Fig. 1.2 shows the laryngoscopic view of vocal folds when respiring and in phonatory position.

When air is expired from lungs, the constriction formed by the vocal folds (which is called *glottis*) induces acceleration of the flow and creates underpressure; under certain circumstances (subglottal pressure, glottal width, longitudinal tension in the TA and ligament) the fluid-structure interaction may invoke vocal fold oscillations. Note that the vibration is a passive process – when voicing, people do not perform any sort of periodic muscle contraction, they only adjust the initial configuration and let the vocal folds vibrate by the airflow.

The creation of voice by vocal fold vibration is usually referred to as phonation. In regular loud phonation, the vocal folds collide and close the channel completely; the duration of the glottis closure may span a considerable part of the vibration period. When whispering or in breathy phonation, the vocal folds may vibrate without collisions.

Even in the case of normal loud phonation, the vocal folds are capable of vibrating in different modes – from the vocologist’s point of view, the resulting voice is then classified into different *registers*, the two most important of them being the *modal (chest)* and *falsetto* registers. Independently of the voice pitch, we sing in the first two octaves (up to 350 Hz in men, approximately) in the modal register, where the vocal folds vibrate as a whole, including the TA muscle and where the voice has ample, rich “color” (spectrum). When trying to reach higher frequencies, the vocal folds suddenly switch to falsetto register, where most of the vibration concentrates to the ligament and mucosa; the resulting voice color is rather “flat”. In training of the professional western-culture singers, a considerable effort is devoted to smooth out the modal-falsetto transition – the subject tries to make the register switching as little audible as possible. In some other singing techniques like yodeling, on the contrary, the singer exploits the register transitions deliberately for artistic purposes.

In normal vocal fold vibration, there is a typical phase shift along the vertical axis: the inferior part of the vocal fold collides prior to the superior segment. In some rather irregular or pathological cases, longitudinal modes (2-0, 3-0 and higher, see [45]) can be observed. These higher eigenmodes of vibration were measured and reported e.g. in [41]. For regular phonation, however, the vocal folds usually vibrate symmetrically and as a whole, i.e. in the 1-0 mode, with vibrational nodes at the anterior and posterior commissures and with the sole antinode in the middle.

The frequency of vibration is influenced by many factors, primarily by the longitudinal tension in the TA muscle and in the ligament. The periodical glottal closure modulates the airflow and generates a sound with the fundamental frequency denoted usually F_0 . The spectrum of the acoustic signal contains harmonic frequencies $f_k = k \cdot F_0$, $k = 2, 3 \dots$ and to certain extent also other frequencies which manifest as noise.

The sound produced by the vocal folds themselves, which can be observed for example in experiments on excised larynges [18], does not resemble human voice at all; it can be compared to the

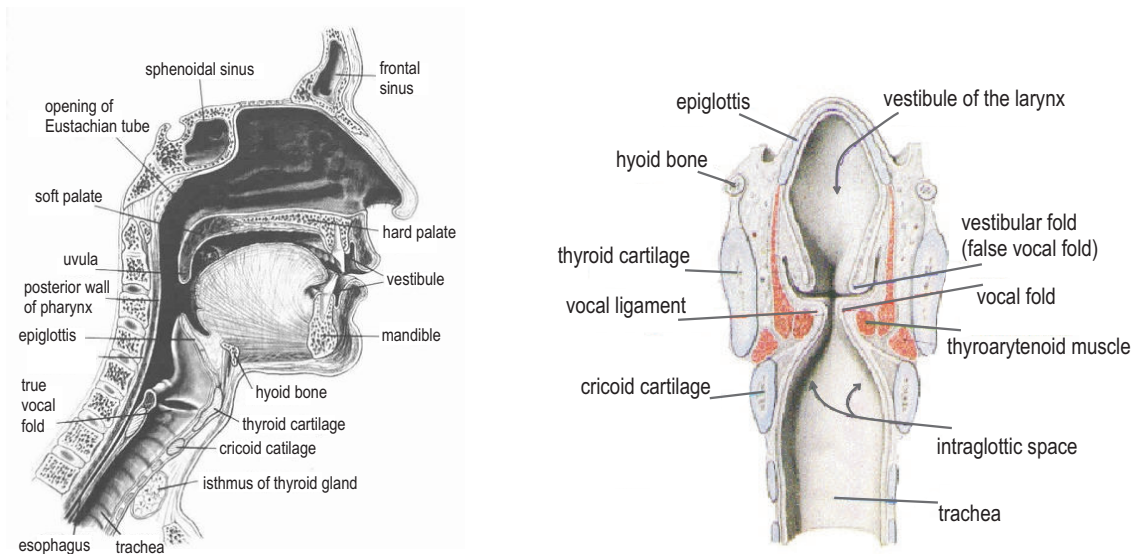


Figure 1.1: Scheme of the vocal tract in sagittal section (left) – the vocal folds are located in the region of the cricoid and thyroid cartilages. Detailed view of the larynx with termination of the trachea in coronal section (right) reveals some of the complicated physiological structures forming the vocal instrument. In the left picture, the anterior-posterior axis is oriented from left to right. In the right one, it is perpendicular to the picture plane. Figures adapted from [4, 21].

sound produced when blowing a bird-call. The human voice results from the acoustic filtering of the original signal by the vocal tract. Based on the actual geometry of the vocal tract, which can be modified mainly by the position of the tongue (see Fig. 1.1), certain frequencies in the spectrum are amplified and other suppressed: in this way, different vowels are generated from the same source signal. When pronouncing the vowels [a:] and [i:], for example, the sound generated by the vocal folds is exactly the same; the difference is that for [a:] the tongue is lowered and the lips wide open, which creates a large resonance cavity with a large round radiator. When producing the [i:] vowel, on the contrary, the tongue reduces the oral acoustic volume to minimum, which changes the resonance frequencies of the vocal tract completely. The vocal tract can be hence regarded as an acoustic resonator, whose frequency response is determined by its dimensions and actual geometry.

1.2 Objectives of the study

There is no doubt that the possibility to produce voice is crucial for human communication, although many people do not realize this until they lose their voice temporarily (due to common respiratory inflammations) or permanently (e.g. after laryngeal cancers). Good knowledge and understanding of the processes and mechanisms which lead to self-sustained vibration of vocal folds is thus important and has extensive applications. The Institute of Thermomechanics has been, for example, involved in the European project Eureka E!2614 *NewVoice* on the development of new voice prostheses for patients after total laryngectomy (surgical removal of larynx necessary after certain cancers, approximately 30 000 patients per year worldwide). The results of the Czech research team were summarized in report [31] and presented in [32].

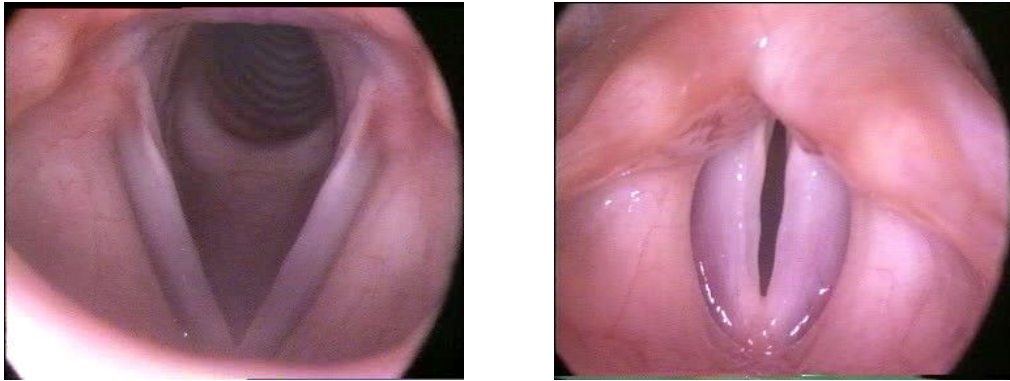


Figure 1.2: Laryngoscopic view of the vocal folds in respiratory (left) and phonatory (right) position. During respiration, abduction of the arytenoid cartilages moves the vocal folds far apart. When phonating, the vocal folds are adducted close together to leave only a narrow glottal opening. Anterior-posterior axis is oriented vertically, with the anterior commissure at the bottom. Images provided by courtesy of Medical Healthcom Ltd., Prague.

The central subject of this study was mathematical modeling and experimental investigation of the glottal velocity fields during flow-induced vocal fold vibration. In the first approximation, it can be assumed that the flow field in the glottal region does not change significantly along the anterior-posterior axis (see Figs. 1.1, 1.2). Thus, it seems reasonable to investigate only 2D flow fields in the coronal plane. In the mathematical model, this approach facilitates substantially the numerical computation: the 3D and 2D models do not differ in principle, but the latter one requires much less computational power. As regards the physical model, Particle Image Velocimetry (PIV) is a method which examines the flow field in a selected 2D plane – hence it is perfectly suitable for 2D examination.

In regular phonation both vocal folds vibrate symmetrically. For the purposes of mathematical or physical modeling, a simplified approach is often used: the symmetry is assumed *ad hoc* and only one half of the channel is modeled. This setup, sometimes called "hemilarynx configuration", is useful to avoid complexity, time consumption of the algorithms and difficulties with unsymmetric vibrations, related rather to pathological voice production. It is necessary, however, to keep in mind that the symmetry is in general not warranted, and in some aspects even not realistic (as an example one may take vortex shedding and jet attachment upstream the glottis, which are definitely not symmetric phenomena).

The approach presented in this thesis tries to take advantage of the hemilarynx configuration, while avoiding untenable assumptions: since the subject of the study is the 2D flow field within glottal space, the whole channel is modeled, but one of the vocal folds is fixed to the channel wall and does not move at all. This approach can be regarded as a simplified starting point for further, more complex analysis. Physiologically, it might be related to voice production in subjects with unilateral vocal fold paralysis.

1.3 Overview of existing vocal fold models

The mathematical model of Ishizaka & Flanagan [20] is usually regarded as the cornerstone of vocal fold modeling; it has been widely used (in various modifications) until present. In this model, the vocal fold was modeled by a system comprising two masses of rectangular shape connected with springs and dampers, the aerodynamics was based on the Bernoulli equation. It is interesting that such a trivial model, which neglects a large majority of the real system features, gave surprisingly good results.

The model of Pelorson and Hirschberg [28] includes more realistic, rounded vocal fold shape and concentrates on the flow separation point. To simplify the equations, the aerodynamic forces which act on the second mass are neglected. Steinecke and Herzel [36] used a similar model to investigate the influence of vocal fold asymmetry. A slightly different two-mass model, featuring translational and rotational motion, was developed by Liljencrants [23]. When studying the Hopf bifurcations using the original Ishizaka & Flanagan's model combined with Story's model of surface waves [37], Lucero showed [25], that by a proper choice of model parameters it is possible to model the falsetto-type vocal fold oscillations, too. Horáček et al. [17] proposed a three-mass 2-degrees-of-freedom model with smooth shape, coupled with quasi-1D flow described by non-stationary Euler equations. A multi-mass model was first introduced by Titze [43, 44]. The main drawback of all lumped-parameter models was pointed out in the work of Story and Titze [37]: there is no clear relation between the model parameters and the anatomy of real vocal folds.

Calculation of the aerodynamic forces in the models summarized above is usually based on the Bernoulli equation, the models mostly do not respect the real vocal fold shape. In some cases (Pelorson and Hirschberg [28]) a variable flow separation point is modeled; in other studies (e.g. Liljencrants [23], Lous et al. [24]), this parameter is assumed to be constant.

In recent years, a completely different approach to glottal flow modeling has been tried: instead of simplified 1-D flow models, the 2D flow fields have been calculated using finite volume or finite element methods, for example in the studies of Alipour and Titze [1] or Thomson et al. [42]. The main drawbacks of this approach are obviously the computational costs, and the difficulties in supplying geometrical and structural parameters for the model.

Regarding the physical vocal fold models, notable results were reported by Deverge, Pelorson et al. [8], who modeled the vocal folds by two flexible latex tubes filled with water, self-vibrating in a wind tunnel. Barney et al. [2] and Kob et al. [22] used vocal fold replicas, which were driven externally: two plane shutters closing a wind tunnel in the first case, and rotating cams in a hydrodynamical channel in the latter. Recently, remarkable studies have been published by Thomson et al. [42], who managed to design a true-scaled self-vibrating vocal fold model fabricated from a highly flexible polyurethane rubber compound.

Chapter 2

Mathematical modeling

In previous works of the author (summarized in detail in master thesis [30] and published in [17]) the system was thoroughly examined from the mechanical point of view: the vocal folds were modeled by a two-degree-of-freedom oscillator, placed in the wall of a channel and coupled with quasi-1D flow of ideal fluid, described by the non-stationary Euler equations. The coupled equations were solved by a semi-analytical method – in this case it was possible to integrate the governing equations analytically over the spatial variable and proceed with numerical solution of a system of ordinary differential equations with respect to the time variable, i.e. to perform numerical simulations of the vocal fold vibration in time. Another possibility was to linearize the equations, transform the system into an eigenvalue problem and carry out stability analysis in frequency domain.

Later on, the algorithm was modified to reflect more accurately the conditions occurring for narrow glottal apertures in order to model more precisely processes accompanying glottis closure. The modified model included variable flow separation point in terms of a moving boundary condition, specified according to a semiempirical criterion. The partial differential equations were discretized by the finite difference method and solved using an explicit scheme. However, this method, reported in [33], did not bring substantial improvement.

The approaches described above, which use rather simplified, one-dimensional fluid model, can be very useful to reveal critical flow values, observe the influence of various model parameters and examine the mechanical phenomena related to vocal fold vibration, such as the displacement, velocity and acceleration waveforms or impact intensity; and all this without requiring excessive computing power. They do not, however, tell much about the fluid-mechanical part of the problem, and some important effects like flow separation, vortex shedding or recirculation cannot be modeled this way at all. Within this thesis, a completely different mathematical model is presented. The flow is described by incompressible non-stationary Navier-Stokes equations in 2D, solved by the finite element method (FEM).

The main advantage of the finite element method is its capability to handle problems with complex geometries. Unlike the finite difference method, which is still popular thanks to simplicity of its implementation and effectiveness of the algorithms, FEM is well suited even for unstructured meshes – one can use meshes with very fine elements in the domains, where high gradients of the solution are expected, and coarser elements elsewhere to spare computer resources. In comparison with the finite volume method, which approximates the solution by a piecewise constant function, the finite element method (using a piecewise polynomial approximation) leads to higher-order, more accurate

numerical schemes [13].

The finite element method, which is widely used for numerical solution of elliptic and parabolic partial differential equations, for example in structural mechanics, seems to be somewhat less popular in computational fluid dynamics (CFD); actually most of the commercial CFD codes employ some variant of the finite volume method. This might be caused by the computational costs of the FEM (with the same number of mesh elements, lower-order methods – such as the finite volume method – offer less accurate, but less computationally expensive solutions), but also by the fact, that for high Reynolds numbers the standard finite element method does not give reliable results. To understand this unfavorable feature, it is necessary to realize that for high-velocity flows the viscous term in the Navier-Stokes equations becomes insignificant against the convective term. It is well known, that for such systems with dominating convection (sometimes also called singularly perturbed problems), standard finite element method is not suitable as it produces nonphysical, “spurious” oscillations in the solution [12]. There exist several stabilization concepts, which can help overcome this numerical problem, namely streamline diffusion method (alias streamline upwind Petrov-Galerkin method, SUPG) or Galerkin least-squares method. These methods, however, require a very careful choice of the stabilization parameters. Since the Reynolds numbers of typical glottal flows do not usually exceed values of $Re = 1000 - 5000$, the standard, non-stabilized finite element numerical scheme was used in this study.

When modeling flow past vibrating vocal folds, yet another, substantial complication is encountered: due to vocal fold vibration, the computational domain Ω changes in time (which implies that the mesh is deformed, too); this makes the straightforward FE discretization impossible. Therefore, the Navier-Stokes equations were first reformulated in arbitrary Lagrangian-Eulerian (ALE) approach. Based on a special mapping $A(t)$ of the fixed, reference configuration Ω_0 (e.g. domain occupied by the fluid at time $t = 0$) onto the deformed, actual configuration Ω_t (domain in time $t > 0$), the ALE method makes possible to apply the finite element method on problems with time-variable geometry [27].

The Navier-Stokes equations are nonlinear; besides the proofs of the existence and uniqueness of the solution (which are available only for several simplified, rather academic cases), this also complicates the numerical solution. The direct FE discretization would lead to a system of nonlinear algebraic equations, which would be, due to the number of unknowns, extremely inconvenient to solve. This is why it is necessary to use a suitable linearization of the convective term. Within this work, the Oseen iteration process was used.

Numerical solution of partial differential equations, whether by the finite volume or finite element method, leads to a large system of linear equations; the efficiency of the whole algorithm is thus essentially affected by the linear solver used. Basically, one can choose between the direct methods, which are fast but become too memory demanding when employed on large matrices, and iterative methods, which are memory efficient, but much slower in general. Moreover, when using iterative methods, it is necessary to concern about convergence, which is not trivial. Most of the modern CFD codes on the market now feature an iterative linear solver based on multigrid acceleration – a concept, which can dramatically improve the time efficiency while preserving reasonable memory requirements. The numerical implementation, which shall be described here, uses a powerful direct linear solver UMFPACK [7].

The mathematical formulation and numerical solution of the problem in 3D and in 2D is, in principle, the same. The difference is that in 3D, it is much more complicated to specify the geometry;

actually, no complete 3D geometrical data regarding the vocal fold shape can be found in literature so far. In 3D, it is necessary to specify more structural and material properties of the system, which are generally not known. What is more, 3D modeling results in considerably increased element numbers and matrix sizes, requiring more time and memory to solve. Therefore, it seems reasonable to start with a 2D mathematical model, which can be in future extended into 3D without principal modifications.

The geometry of the problem, i.e. the 2D shape of the vocal folds and adjoining vocal tract, was specified according to measurements on excised human larynges, performed in the Institute of Thermomechanics [34]. More specifically, the geometry of the computational domain Ω_0 at zero displacement was modeled on the basis of the measurements of the mid-membranous coronal section of larynx No.8 (female, 72 years, phonated at the fundamental frequency $F_0 = 308$ Hz).

2.1 Mathematical description

2.1.1 Equations of motion of the mechanical system

From the mechanical point of view, real vocal folds constitute a very complex system. They consist of several tissue layers composed of diverse viscoelastic materials, whose mechanical properties are generally not known. Therefore it is often necessary to take up with simplified, lumped-parameter models and to try to match at least several fundamental dynamic properties (e.g. natural frequencies and damping factors) of real vocal folds. To illustrate the method, the equations of motion will be derived for a simple two-degrees-of-freedom dynamic system.

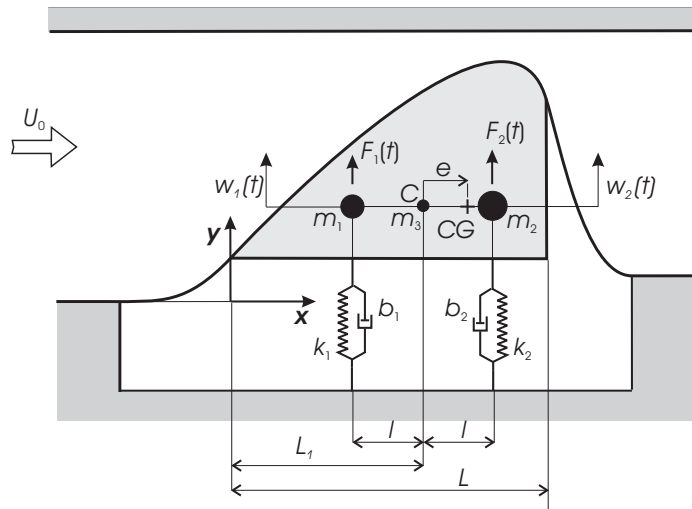


Figure 2.1: Geometric definitions in the mathematical model (hemilarynx configuration). Rigid body of mass m and moment of inertia J (with respect to the center of gravity CG), supported by springs and dampers. For the derivation of the equations of motion, the rigid body can be replaced by a dynamically equivalent three-mass system m_1, m_2, m_3 .

The real, continuously elastic vocal fold is first replaced by a rigid body supported by two springs and dampers (see Fig. 2.1). The kinematic model reflects two basic modes of the vocal fold motion:

vertical shift along the y-axis and rotation with respect to C. For the generalized coordinates one may take vertical displacements w_1 and w_2 at the locations of m_1 and m_2 , respectively. Note that within such system, the third mode – horizontal motion of the vocal fold, which is important in real voice production, too – is blocked; this is however necessary to preserve simplicity and to avoid the necessity to supply additional parameters, which are not known.

To derive the equations of motion, the rigid body of mass m , static moment $m \cdot e$ (with respect to the location of m_3) and moment of inertia J (with respect to the center of gravity CG) can be temporarily replaced by a dynamically equivalent three-mass system m_1, m_2, m_3 . The conditions of equal mass, static moment and moment of inertia

$$\begin{aligned} m_1 + m_2 + m_3 &= m \\ -m_1 l + m_2 l &= m e \\ m_1 l^2 + m_2 l^2 &= J + m e^2 \end{aligned} \quad (2.1)$$

yield

$$\begin{aligned} m_1 &= \frac{1}{2 l^2} (m e^2 - m e l + J) \\ m_2 &= \frac{1}{2 l^2} (m e^2 + m e l + J) \\ m_3 &= m \left[1 - \left(\frac{e}{l} \right)^2 \right] - \frac{J}{l^2}. \end{aligned} \quad (2.2)$$

Now it is easy to write the linearized Lagrange function L for the equivalent undamped system (assuming small amplitudes):

$$L = \frac{1}{2} m_1 \dot{w}_1^2 + \frac{1}{2} m_3 \left(\frac{\dot{w}_1 + \dot{w}_2}{2} \right)^2 + \frac{1}{2} m_2 \dot{w}_2^2 - \left[\frac{1}{2} k_1 w_1^2 + \frac{1}{2} k_2 w_2^2 \right]. \quad (2.3)$$

Application of the Lagrange equations on (2.3)

$$\frac{d}{dt} \left(\frac{\partial L}{\partial \dot{w}_i} \right) - \frac{\partial L}{\partial w_i} = F_i \quad i = 1, 2, \quad (2.4)$$

where F_i are the (generalized) excitation forces, gives the equations of motion for the undamped system

$$\begin{aligned} m_1 \ddot{w}_1 + \frac{m_3}{4} (\ddot{w}_1 + \ddot{w}_2) + k_1 w_1 &= F_1 \\ m_2 \ddot{w}_2 + \frac{m_3}{4} (\ddot{w}_1 + \ddot{w}_2) + k_2 w_2 &= F_2. \end{aligned} \quad (2.5)$$

Using matrix notation and introducing the displacement vector $\mathbf{W}(t) = (w_1(t), w_2(t))^T$, one may rewrite (2.5) as

$$\mathbb{M} \ddot{\mathbf{W}} + \mathbb{K} \mathbf{W} = \mathbf{F}, \quad (2.6)$$

where \mathbb{M} , \mathbb{K} are the mass and stiffness matrices and $\mathbf{F} = (F_1, F_2)^T$ is the vector of excitation forces. The spring stiffnesses k_1, k_2 in (2.5), which were not specified so far, can be set in such a way that the natural frequencies of the model match the first two resonance frequencies measured on real vocal folds (such experiments were performed in the Institute of Thermomechanics and reported in [41]). The first step is to substitute a harmonic solution $\mathbf{W}(t) = \mathbf{A} e^{\omega t}$, where $\omega \in \mathbb{C}$ is the complex angular frequency and \mathbf{A} the amplitude vector, into the equations of motion (2.6) with zero excitation $\mathbf{F} = \mathbf{0}$, which gives

$$(\omega^2 \mathbb{M} + \mathbb{K}) \mathbf{A} = \mathbf{0}. \quad (2.7)$$

This equation is usually exploited to determine the circular eigenfrequencies of a system when the mass and stiffness matrices are known. However, it can be used in a reversed way – to calculate the unknown stiffness constants k_1, k_2 from known (measured) eigenfrequencies ω_1, ω_2 . In order to obtain a nontrivial solution, the determinant of the matrix (2.7) must be zero:

$$|\omega^2 \mathbb{M} + \mathbb{K}| = \left(k_1 + \left(m_1 + \frac{m_3}{4}\right) \omega^2\right) \left(k_2 + \left(m_2 + \frac{m_3}{4}\right) \omega^2\right) - \frac{m_3^2}{16} \omega^4 = 0. \quad (2.8)$$

Substituting the experimental angular resonance frequencies ω_1, ω_2 into (2.8) yields a system of two quadratic equations for stiffnesses k_1, k_2 , which can be easily solved.

So far, we were concerned with the undamped system. The equations of motion of the damped system read

$$\mathbb{M} \ddot{\mathbf{W}} + \mathbb{B} \dot{\mathbf{W}} + \mathbb{K} \mathbf{W} = \mathbf{F}. \quad (2.9)$$

The damping matrix \mathbb{B} is generally not easy to specify; one possible approach is to use the proportional damping model, which assumes

$$\mathbb{B} = \epsilon_1 \mathbb{M} + \epsilon_2 \mathbb{K}. \quad (2.10)$$

The coefficients of the proportional damping ϵ_1, ϵ_2 can be calculated according to approximate formulas [19]

$$\epsilon_1 = 2\pi \frac{\Delta f_1 f_2^2 - \Delta f_2 f_1^2}{f_2^2 - f_1^2}, \quad \epsilon_2 = \frac{1}{2\pi} \frac{\Delta f_1 - \Delta f_2}{f_1^2 - f_2^2}, \quad (2.11)$$

where $f_i = \frac{1}{2\pi} \omega_i$ are the measured resonance frequencies and Δf_i stand for the experimental 3dB half-power widths of the corresponding resonance peaks.

Once the excitation forces $\mathbf{F}(t)$ are known, the equations of motion (2.9) represent a system of two linear second-order ordinary differential equations, which can be easily transformed into four first-order equations and solved numerically e.g. by the Runge-Kutta method.

Using a different model with more degrees of freedom does not change anything in the principles and methods described, it just complicates technically the derivation of the equations and makes necessary to supply more structural constants. There is even no need to linearize the Lagrange function – for the numerical solution in time the equations of motion need not be linear.

2.1.2 Formulation of the coupled problem

Once the equations of motion of the mechanical system are known, it is possible to proceed to the formulation of the coupled problem, i.e. to derive equations describing jointly the flow and the vocal fold motion, which are in interaction. In our case, the coupling is realized by aerodynamic forces (determined by the flow pressure field), which act on the surface of the vocal folds and induce their motion; from the other side, the moving vocal folds modify the shape of the flow domain thus affecting back the velocity and pressure fields.

As for the fluid model, we shall describe the flow of an incompressible viscous Newtonian fluid in a bounded 2D domain. In what follows, vector-valued quantities will be in bold, tensors and matrices double-struck. Numerical indices denote vector components.

Let $\Omega_t \subset \mathbb{R}^2$ be the domain occupied by the fluid at time $t \in (0, T)$. The boundary $\Gamma = \partial\Omega$ is composed of four non-intersecting parts (see Fig. 2.2): $\Gamma = \Gamma_{in} \cup \Gamma_{out} \cup \Gamma_{wall} \cup \Gamma_{VF}$, where Γ_{in} and Γ_{out} are virtual boundaries representing the inlet and outlet, $\Gamma_{wall} = \Gamma_{wall}^{b1} \cup \Gamma_{wall}^{b2} \cup \Gamma_{wall}^{u1} \cup \Gamma_{wall}^{u2}$ is the fixed wall, which is not a function of time, and $\Gamma_{VF} = \Gamma_{VF}^b \cup \Gamma_{VF}^u$ stands for the surface of the moving vocal folds. The superscripts 'b' and 'u' denote the bottom and upper parts, respectively.

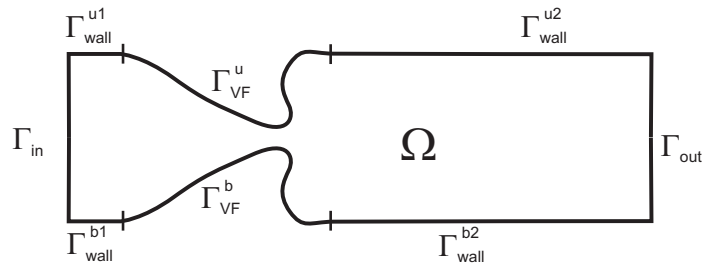


Figure 2.2: Sketch of the computational domain and definition of its boundary parts. Inlet Γ_{in} , outlet Γ_{out} , fixed wall Γ_{wall} and moving vocal folds Γ_{VF} .

Let $q_i^b(t)$ and $q_j^u(t)$ be the generalized coordinates specifying uniquely the position of the bottom and upper vocal fold, respectively. According to the mechanical vocal fold model used, the indices i, j may be equal to 1 for a one degree-of-freedom (1-DOF) system, they may run from 1–2 in the case of the 2-DOF model described in section 2.1.1 (in this case, we have simply $q_1^b = w_1$, $q_2^b = w_2$), from 1–3 for a generally moving rigid body in 2D with three DOF or from 1– n when a discrete multi-mass system is used. The number of generalized coordinates might be even infinite in the case of continuous elastic vocal fold modeling. In any case, the shape of the domain is an

explicit function of the generalized coordinates only, $\Omega_t = F(q_i^b, q_j^u)$, $i = 1..N_{DOF}^b$, $j = 1..N_{DOF}^u$.

Our goal is to find the flow velocity $\mathbf{u}(t, \mathbf{x})$, kinematic pressure $p(t, \mathbf{x})$ and generalized coordinates of the vocal folds $q_i^b(t)$, $q_j^u(t)$, $t \in (0, T)$, $\mathbf{x} \in \Omega_t$, $i = 1..N_{DOF}^b$, $j = 1..N_{DOF}^u$. Kinematic pressure is the pressure (in Pascals) divided by the fluid density.

Incompressible flow of a Newtonian fluid in a non-deforming domain Ω is described by the incompressible Navier-Stokes equations and by the continuity equation:

$$\begin{aligned} \frac{\partial \mathbf{u}}{\partial t} + (\mathbf{u} \cdot \nabla) \mathbf{u} + \nabla p - \nu \Delta \mathbf{u} &= 0 & \text{in } (0, T) \times \Omega \\ \text{div } \mathbf{u} &= 0 & \text{in } (0, T) \times \Omega \end{aligned} \quad , \quad (2.12)$$

where ν denotes the kinematic fluid viscosity. However, since the Eulerian time derivative $\partial/\partial t$ is not well defined in a time-dependent computational domain Ω_t , the standard, Eulerian form (2.12) of the governing equations is not suitable for description of the flow in a domain that deforms in time. Therefore it will be reformulated using the arbitrary Lagrangian-Eulerian approach.

2.1.3 Arbitrary Lagrangian-Eulerian method

Before we proceed to the derivation of the Navier-Stokes equations in ALE approach, let us remind two basic time derivatives, which are used in fluid dynamics. The first one is the **Eulerian** derivative $\partial/\partial t$, which represents the rate of change of some quantity in a fixed point. The **material** (substantive, Lagrangian) derivative

$$\frac{D}{Dt} = \frac{\partial}{\partial t} + (\mathbf{u} \cdot \nabla) \quad , \quad (2.13)$$

on the other hand, reflects the rate of change of some property of a specific fluid particle, moving with the fluid. Further, yet another time derivative – the ALE derivative – shall be introduced.

The fundamental concept of the ALE method, used in CFD problems with time-variable geometry (such as wave propagation on free surface, fluids containing floating bodies, fluid-structure interaction problems), is to relate the equations defined in the actual, “deformed” configuration – the domain Ω_t at time t – to a reference configuration Ω_0 , which is usually the domain at $t = 0$ (see Fig. 2.3). This is realized using the ALE mapping $A_t : \Omega_0 \mapsto \Omega_t$, which is for each $t \in [0, T]$ a smooth bijection (one-to-one mapping of Ω_0 onto Ω_t with continuous first partial derivatives).

For the coordinates in the actual configuration, space coordinates, we will use small letters; the coordinates in the reference configuration – reference coordinates – will be in uppercase. Hence we may write $\mathbf{x} = \mathbf{x}(t, \mathbf{X}) = A_t(\mathbf{X})$, $\mathbf{X} = A_t^{-1}(\mathbf{x})$. In what follows, by Φ we will denote the domain, where the velocity and pressure fields $\mathbf{u}(t, \mathbf{x})$ and $p(t, \mathbf{x})$ are defined:

$$\Phi = \left\{ (t, \mathbf{x}) : t \in (0, T), \mathbf{x} \in \Omega_t \right\} . \quad (2.14)$$

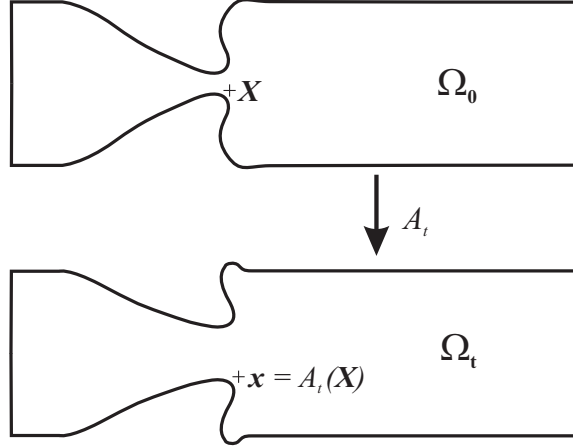


Figure 2.3: Illustration of the ALE mapping A_t - a smooth mapping of the reference configuration Ω_0 onto the actual configuration Ω_t . Reference coordinates \mathbf{X} and space coordinates \mathbf{x} .

A function $f : \Phi \mapsto \mathbb{R}$, defined in the actual configuration, can be transformed into the reference configuration, where it will be referred to as \tilde{f} :

$$\tilde{f}(t, \mathbf{X}) = f(t, \mathbf{x}), \quad \mathbf{x} = A_t(\mathbf{X}). \quad (2.15)$$

Let us define the **domain velocity**

$$\tilde{\mathbf{w}}(t, \mathbf{X}) = \frac{\partial}{\partial t} A_t(\mathbf{X}) = \frac{\partial}{\partial t} \mathbf{x}(t, \mathbf{X}), \quad (2.16)$$

or in space coordinates

$$\mathbf{w}(t, \mathbf{x}) = \tilde{\mathbf{w}}(t, \mathbf{X}), \quad \mathbf{X} = A_t^{-1}(\mathbf{x}). \quad (2.17)$$

Now we can proceed to the definition of the **ALE derivative** $\frac{D^A}{Dt} : \Phi \mapsto \mathbb{R}$:

$$\frac{D^A}{Dt} f(t, \mathbf{x}) = \frac{\partial}{\partial t} \tilde{f}(t, \mathbf{X}), \quad \mathbf{X} = A_t^{-1}(\mathbf{x}). \quad (2.18)$$

Lemma 2.1. Let Ω_0 be a bounded domain, $\Omega_t = A_t(\Omega_0)$. Let $f : \Phi \mapsto \mathbb{R}$ be a function with continuous partial derivatives of order 1, $f \in C^1(\Phi)$. Then

$$\frac{D^A}{Dt} f = \frac{\partial f}{\partial t} + (\mathbf{w} \cdot \nabla) f$$

Proof. Using the ALE velocity definition (2.18), the domain velocity definition (2.16), relation (2.15) and applying the chain rule, for a fixed $\mathbf{x} = A_t(\mathbf{X})$ we can write

$$\begin{aligned} \frac{D^A}{Dt} f(t, \mathbf{x}) &= \frac{\partial}{\partial t} \tilde{f}(t, \mathbf{X}) = \frac{d}{dt} f(t, A_t(\mathbf{X})) = \frac{\partial f}{\partial t}(t, \mathbf{x}) + \sum_{i=1}^2 \frac{\partial f}{\partial x_i}(t, \mathbf{x}) \underbrace{\left(\frac{d}{dt} A_t(X) \right)_i}_{\tilde{w}_i(t, \mathbf{X}) = w_i(t, \mathbf{x})} = \\ &= \frac{\partial f}{\partial t}(t, \mathbf{x}) + (\mathbf{w} \cdot \nabla) f(t, \mathbf{x}) . \end{aligned}$$

□

We see that the ALE derivative $D^A/Dt = \partial/\partial t + (\mathbf{w} \cdot \nabla)$ is analogous to the material derivative $D/Dt = \partial/\partial t + (\mathbf{u} \cdot \nabla)$ in Lagrangian approach. The difference is that in Lagrangian description we track the particles with velocity \mathbf{u} ; the ALE approach, on the other hand, follows the “deformation” of the particles of the reference configuration (the vertices of the computational mesh for example), whose velocity is the domain velocity \mathbf{w} .

Lemma 2.1 holds also for vector-valued functions $\mathbf{f}(\mathbf{x}, t)$. In this case, $(\mathbf{w} \cdot \nabla) \mathbf{f}$ is a vector with components

$$\left((\mathbf{w} \cdot \nabla) \mathbf{f} \right)_i = \sum_{j=1}^2 w_j \frac{\partial f_i}{\partial x_j} . \quad (2.19)$$

The next quantity, which will be important in following derivations, is the Jacobi determinant of the ALE mapping J^{A_t} :

$$J^{A_t}(\mathbf{x}) = \left| \frac{\partial A_t(\mathbf{X})}{\partial \mathbf{X}} \right| = \begin{vmatrix} \frac{\partial A_{t,1}}{\partial X_1}(\mathbf{X}) & \frac{\partial A_{t,1}}{\partial X_2}(\mathbf{X}) \\ \frac{\partial A_{t,2}}{\partial X_1}(\mathbf{X}) & \frac{\partial A_{t,2}}{\partial X_2}(\mathbf{X}) \end{vmatrix}, \quad \mathbf{X} = A_t^{-1}(\mathbf{x}) . \quad (2.20)$$

Due to the fact that the ALE mapping A_t is surjective $\forall t \in [0, T]$ and that $A_t(\mathbf{X}) = \text{Id}(\mathbf{X}) = \mathbf{X}$ for $t = 0$, it can be proven [29] that

$$J^{A_t} > 0 . \quad (2.21)$$

Furthermore, the following relation holds [11, 29]:

$$\frac{D^A}{Dt} J^{A_t}(\mathbf{x}) = J^{A_t}(\mathbf{x}) \text{div } \mathbf{w}(t, \mathbf{x}) . \quad (2.22)$$

Theorem 2.2. (transport theorem in ALE formulation)

Let $V_t \subset \Omega_t$ be a bounded domain, $f \in C^1(\Phi)$. Then

$$\frac{d}{dt} \int_{V_t} f \, d\mathbf{x} = \int_{V_t} \left(\frac{D^A}{Dt} f + f \operatorname{div} \mathbf{w} \right) d\mathbf{x} . \quad (2.23)$$

Proof. Let us denote $V_0 = A_t^{-1}(V_t)$. By the substitution theorem, the integral can be rewritten as

$$\frac{d}{dt} \int_{V_t} f(t, \mathbf{x}) \, d\mathbf{x} = \frac{d}{dt} \int_{V_0} \tilde{f}(t, \mathbf{X}) \tilde{J}^{A_t}(\mathbf{X}) \, d\mathbf{X} .$$

Since the integration domain V_0 is no longer dependent on time, we can apply the theorem on differentiation of an integral with respect to a parameter. Using the definition (2.18) of the ALE derivative, equation (2.22) and performing the inverse substitution we get

$$\begin{aligned} \frac{d}{dt} \int_{V_0} \tilde{f}(t, \mathbf{X}) \tilde{J}^{A_t}(\mathbf{X}) \, d\mathbf{X} &= \int_{V_0} \left(\underbrace{\frac{\partial \tilde{f}}{\partial t}(t, \mathbf{X})}_{\frac{D^A}{Dt} f(t, \mathbf{x})} \tilde{J}^{A_t}(\mathbf{X}) + \tilde{f}(t, \mathbf{X}) \underbrace{\frac{\partial \tilde{J}^{A_t}(\mathbf{X})}{\partial t}}_{\frac{D^A}{Dt} J^{A_t}(\mathbf{x})} \right) d\mathbf{X} = \\ &= \int_{V_t} \left(\frac{D^A}{Dt} f(t, \mathbf{x}) + f(t, \mathbf{x}) \operatorname{div} \mathbf{w}(t, \mathbf{x}) \right) d\mathbf{x} . \end{aligned}$$

□

2.1.4 Navier-Stokes equations in ALE formulation

The incompressible Navier-Stokes equations can be derived from the principles of conservation of mass, momentum and angular momentum. Additionally, it is necessary to assume a constitutive relation for the fluid, which relates the stress and strain tensors. In Eulerian description, the principle of conservation of mass for an incompressible fluid expresses as the continuity equation

$$\operatorname{div} \mathbf{u}(t, \mathbf{x}) = 0 \quad \text{in } \Phi . \quad (2.24)$$

The continuity equation does not include any time derivatives and can be discretized in a standard way; therefore it will be used in this form even in the ALE formulation.

Now we will exploit the momentum equation. Let us consider an arbitrary non-material volume V with a boundary ∂V , moving with a velocity \mathbf{v} . The momentum equation (the second Newton's law) states that the material time derivative of momentum is equal to the sum of external forces:

$$\frac{D}{Dt} (\rho \mathbf{u}) = \frac{\partial}{\partial t} (\rho \mathbf{u}) + [\mathbf{u} \cdot \nabla] (\rho \mathbf{u}) = \nabla \cdot \mathbb{T} + \rho \mathbf{f} , \quad (2.25)$$

where \mathbb{T} is the Cauchy stress tensor, representing the effects of surface forces, and \mathbf{f} is the density of volume forces.

For further derivations, we will need the Reynolds transport theorem, which expresses the time derivative of an integral form. The standard Reynolds transport theorem deals with integrals over material volumes, containing permanently the same particles of continuum. In our case, however, V is not a material volume; hence we will need the general form of Reynolds transport theorem (see [35] for detailed derivation)

$$\frac{d}{dt} \int_V f \, d\mathbf{x} = \int_V \frac{\partial f}{\partial t} \, d\mathbf{x} + \int_{\partial V} f \, \mathbf{v} \cdot \mathbf{n} \, d\sigma, \quad (2.26)$$

where \mathbf{n} stands for the unit outer normal. The theorem states that the rate of change of the integral of a function $f(t, \mathbf{x})$ over an arbitrary time-variable volume V is equal to the change of f inside V and the flux of f across the boundary ∂V . Note that in the surface integral, the velocity \mathbf{v} of the boundary ∂V is involved, instead of the velocity \mathbf{u} of the boundary of a material volume (equal to the flow velocity), which figures in standard Reynolds transport theorem.

Specifically, the transport theorem (2.26) for the momentum $\rho \mathbf{u}$, for the volume V_t and the boundary ∂V_t whose velocity is \mathbf{w} gives

$$\int_{V_t} \frac{\partial(\rho \mathbf{u})}{\partial t} \, d\mathbf{x} = \frac{d}{dt} \int_{V_t} \rho \mathbf{u} \, d\mathbf{x} - \int_{\partial V_t} (\rho \mathbf{u}) \, \mathbf{w} \cdot \mathbf{n} \, d\sigma. \quad (2.27)$$

Substituting (2.27) into the momentum equation (2.25) integrated over V_t yields

$$\begin{aligned} \mathbf{F} = \int_{V_t} (\nabla \cdot \mathbb{T} + \rho \mathbf{f}) \, d\mathbf{x} &= \frac{d}{dt} \int_{V_t} \rho \mathbf{u} \, d\mathbf{x} - \int_{\partial V_t} (\rho \mathbf{u}) \, \mathbf{w} \cdot \mathbf{n} \, d\sigma + \\ &\int_{V_t} [\mathbf{u} \cdot \nabla](\rho \mathbf{u}) \, d\mathbf{x}, \end{aligned} \quad (2.28)$$

where \mathbf{F} is the resultant of the forces acting on V_t . When applying the ALE transport theorem (2.23) to express the first integral on the right hand side of (2.28), we get

$$\begin{aligned} \mathbf{F} = \int_{V_t} \left(\frac{D^A}{Dt} (\rho \mathbf{u}) + (\rho \mathbf{u}) \operatorname{div} \mathbf{w} \right) \, d\mathbf{x} &- \int_{\partial V_t} (\rho \mathbf{u}) \, \mathbf{w} \cdot \mathbf{n} \, d\sigma + \\ &\int_{V_t} [\mathbf{u} \cdot \nabla](\rho \mathbf{u}) \, d\mathbf{x}. \end{aligned} \quad (2.29)$$

Using the Green's theorem, for the i -th component of the surface integral in (2.29) we can write

$$\begin{aligned}
\int_{\partial V_t} (\rho u_i) \mathbf{w} \cdot \mathbf{n} \, d\sigma &= \int_{\partial V_t} (\rho u_i \mathbf{w}) \cdot \mathbf{n} \, d\sigma = \int_{V_t} \operatorname{div} (\rho u_i \mathbf{w}) \, d\mathbf{x} = \\
&= \int_{V_t} w_1 \frac{\partial(\rho u_i)}{\partial x_1} + w_2 \frac{\partial(\rho u_i)}{\partial x_2} + w_3 \frac{\partial(\rho u_i)}{\partial x_3} + \rho u_i \operatorname{div} \mathbf{w} \, d\mathbf{x} = \\
&= \int_{V_t} [\mathbf{w} \cdot \nabla] (\rho u_i) + \rho u_i \operatorname{div} \mathbf{w} \, d\mathbf{x} ,
\end{aligned} \tag{2.30}$$

which gives

$$\int_{\partial V_t} (\rho \mathbf{u}) \mathbf{w} \cdot \mathbf{n} \, d\sigma = \int_{V_t} [\mathbf{w} \cdot \nabla] (\rho \mathbf{u}) + \rho \mathbf{u} \operatorname{div} \mathbf{w} \, d\mathbf{x} . \tag{2.31}$$

For the incompressible fluid $\rho(\mathbf{x}, t) = \text{const}$, substituting (2.31) into (2.29) finally yields

$$\mathbf{F} = \rho \int_{V_t} \left(\frac{D^A}{Dt} \mathbf{u} + [(\mathbf{u} - \mathbf{w}) \cdot \nabla] \mathbf{u} \right) d\mathbf{x} . \tag{2.32}$$

As seen in (2.28), the vector of the outer forces $\mathbf{F} = \mathbf{F}_V + \mathbf{F}_S$ is composed of the volume forces

$$\mathbf{F}_V = \int_{V_t} \rho \mathbf{f}(t, \mathbf{x}) \, d\mathbf{x} \tag{2.33}$$

and the surface forces

$$\mathbf{F}_S = \int_{V_t} \nabla \cdot \mathbb{T} \, d\mathbf{x} = \int_{\partial V_t} \mathbb{T}(t, \mathbf{x}) \cdot \mathbf{n} \, d\sigma = \int_{\partial V_t} \boldsymbol{\tau}(t, \mathbf{x}, \mathbf{n}) \, d\sigma , \tag{2.34}$$

where \mathbb{T} is the stress tensor and $\boldsymbol{\tau} = \mathbb{T} \cdot \mathbf{n}$ is the stress vector (density of the surface forces). Now it is necessary to include the constitutive relation. Supposing Newtonian fluid, in which the shear stress is linearly proportional to the velocity gradient, the constitutive relation states that

$$\mathbb{T}_{ij} = -P \delta_{ij} + \mu \left(\frac{\partial u_i}{\partial x_j} + \frac{\partial u_j}{\partial x_i} \right) , \tag{2.35}$$

where δ_{ij} stands for the Kronecker delta, P is pressure and μ the dynamic fluid viscosity. The rest of the derivation is identical with that of the standard Navier-Stokes equations, and shall be only briefly outlined here: using the constitutive relation (2.35) it can be easily shown that

$$\nabla \cdot \mathbb{T} = -\nabla P + \mu \Delta \mathbf{u} . \tag{2.36}$$

Neglecting the volume forces \mathbf{f} , introducing the kinematic pressure $p = P/\rho$, kinematic viscosity $\nu = \mu/\rho$ and combining (2.32), (2.34) and (2.36) immediately yields the ALE-formulation of the Navier-Stokes equations, defined in Φ :

$$\begin{aligned} \frac{D^A}{Dt} \mathbf{u} + [(\mathbf{u} - \mathbf{w}) \cdot \nabla] \mathbf{u} + \nabla p - \nu \Delta \mathbf{u} &= 0 \\ \operatorname{div} \mathbf{u} &= 0 \quad . \end{aligned} \quad (2.37)$$

Note that if we are not interested in the detailed derivation of the Navier-Stokes equations, the ALE-formulation (2.37) can be obtained immediately by substituting the result of Lemma 2.1 for $f = \mathbf{u}$ into the standard Navier-Stokes equations (2.12).

2.1.5 Initial and boundary conditions

To solve the Navier-Stokes equations (2.37), it is necessary to supply suitable boundary conditions on the boundary $\partial\Omega_t$ of the computational domain Ω_t . The boundary is composed of several different parts (see Fig. 2.2) – the inlet Γ_{in} , the fixed walls Γ_{wall} , the moving vocal fold surfaces Γ_{VF} and the outlet Γ_{out} .

The inlet flow, coming through Γ_{in} , is imposed as needed. In the computations presented within this work a parabolic profile of the vertical velocity component was used,

$$\mathbf{u}(t, \mathbf{x}) = \begin{pmatrix} -4 U_0 \frac{(x_2 - x_2^{TL})(x_2 - x_2^{BL})}{(x_2^{TL} - x_2^{BL})^2} \\ 0 \end{pmatrix} \quad \text{for } \mathbf{x} \in \Gamma_{in}, t \in [0, T], \quad (2.38)$$

where U_0 is the maximum flow velocity at the channel axis and \mathbf{x}^{TL} , \mathbf{x}^{BL} represent the coordinates of the top and bottom left domain corners, respectively.

Since we use a viscous model, the “no-slip condition” is prescribed on the fixed walls Γ_{wall} :

$$\mathbf{u}(t, \mathbf{x}) = \mathbf{0} \quad \text{for } \mathbf{x} \in \Gamma_{wall}, t \in [0, T]. \quad (2.39)$$

On the moving vocal fold surfaces, the velocity of the fluid particles must be equal to the velocity of the moving surface, which is given by the ALE-velocity \mathbf{w} . Hence,

$$\mathbf{u}(t, \mathbf{x}) = \mathbf{w}(t, \mathbf{x}) \quad \text{for } \mathbf{x} \in \Gamma_{VF}, t \in [0, T]. \quad (2.40)$$

Finally, some condition has to be specified on the outlet Γ_{out} . Unlike the previous cases, this represents a rather delicate question – we need to set a sufficiently “unrestrictive” formula. One possible choice is the “do-nothing condition” [47]

$$-\nu \frac{\partial \mathbf{u}}{\partial \mathbf{n}}(t, \mathbf{x}) + p(t, \mathbf{x}) \mathbf{n}(\mathbf{x}) = p_{ref} \mathbf{n}(\mathbf{x}) \quad \text{for } \mathbf{x} \in \Gamma_{out}, t \in [0, T], \quad (2.41)$$

where ν is the fluid viscosity, $\partial/\partial \mathbf{n}$ denotes the normal derivative, $\mathbf{n}(\mathbf{x})$ is the unit outer normal to Γ_{out} and p_{ref} is a reference pressure, which can be set to zero. The physical meaning of the reference pressure becomes clear when the do-nothing condition is set on Γ_{in} , too, instead of prescribing the parabolic velocity profile. Then, the value $(p_{ref}^{in} - p_{ref}^{out})$ determines the pressure difference between Γ_{in} and Γ_{out} which drives the flow. In phoniatric terms, this difference is called *transglottal pressure* and is approximately equal to the lung pressure during phonation.

The origins of the do-nothing condition, which are not obvious at the moment, actually arise from the weak formulation of the Navier-Stokes equations. This matter will be discussed more thoroughly in section 2.2.4.

Since the non-stationary Navier-Stokes equations include time derivative, suitable initial conditions

$$\mathbf{u}^0(\mathbf{x}) = \mathbf{u}(0, \mathbf{x}), \quad p^0(\mathbf{x}) = p(0, \mathbf{x}) \quad (2.42)$$

must be supplied, too. One possibility is to solve the stationary Navier-Stokes equations

$$\begin{aligned} [(\mathbf{u}(\mathbf{x}) - \mathbf{w}(\mathbf{x})) \cdot \nabla] \mathbf{u}(\mathbf{x}) + \nabla p(\mathbf{x}) - \nu \Delta \mathbf{u}(\mathbf{x}) &= 0 & \forall x \in \Omega_0 \\ \operatorname{div} \mathbf{u}(\mathbf{x}) &= 0 & \forall x \in \Omega_0 \end{aligned} \quad (2.43)$$

and to use the stationary solution as the initial condition. This approach is applicable only for low Reynolds numbers (which is our case) – for higher flow velocities, the numerical solution of the stationary system does not usually converge.

2.1.6 Dimensionless variables

When describing physical processes by mathematical equations, it is often advantageous to pass from dimensional quantities towards dimensionless variables. Firstly, in the dimensionless form of the governing equations, the relative importance of the terms becomes more evident. The dimensional analysis allows to create scaled, but dynamically similar models, thus predicting the behavior of the original system on the basis of the results from the scaled model. Moreover, the dimensionless form of the equations is more suitable for the numerical solution due to the computer arithmetics properties.

In the Navier-Stokes equations (2.37) we shall introduce dimensionless space coordinate, velocity, time and pressure denoted \mathbf{x}' , \mathbf{u}' , t' and p' . These will be defined using suitable scales X^* , U^* , T^* and P^* as follows:

$$\mathbf{x} = L^* \mathbf{x}', \quad \mathbf{u} = U^* \mathbf{u}', \quad t = T^* t', \quad p = P^* p'. \quad (2.44)$$

The length scale L^* can be chosen as the length of the vocal fold (denoted L in Fig. 2.6). Based on the geometric data available [34], the length scale used in the computations was

$$L^* = 43.11 \cdot 10^{-3} \text{ m} . \quad (2.45)$$

It is convenient to take the velocity scale U^* as the flow velocity at the channel axis on Γ_{in} , $U^* = U_0$ (see 2.38), according to the boundary condition which is prescribed there. Henceforth, it is not possible to choose neither the time nor the pressure scale arbitrarily – it is necessary to set

$$T^* = \frac{L^*}{U^*} \quad (2.46)$$

$$P^* = (U^*)^2 . \quad (2.47)$$

Note that P^* is the scale of the *kinematic* pressure (dynamic pressure divided by the fluid density), whose physical dimension is $\frac{N m^3}{m^2 kg} = \frac{kg m, m^3}{s^2 m^2 kg} = m^2/s^2$.

Differentiating (2.44) yields

$$\begin{aligned} \frac{d}{dx'} &= L^* \frac{d}{dx} , \quad \text{i.e. } \nabla' = L^* \nabla , \\ \frac{d}{dt'} &= T^* \frac{d}{dt} . \end{aligned} \quad (2.48)$$

By substituting (2.44), (2.46), (2.47) and (2.48) into the dimensional Navier-Stokes and continuity equations (2.37) we get

$$\begin{aligned} \frac{U^*}{L^*} \frac{D^A}{Dt'} \mathbf{u}' U^* + \left[U^* (\mathbf{u}' - \mathbf{w}') \cdot \frac{1}{L^*} \nabla' \right] \mathbf{u}' U^* + \frac{1}{L^*} \nabla' p' P^* - \nu \frac{1}{L^{*2}} \Delta' \mathbf{u}' U^* &= 0 \\ \frac{1}{L^*} \text{div}' \mathbf{u}' U^* &= 0 . \end{aligned} \quad (2.49)$$

Now, if we multiply the first equation by L^*/U^{*2} , introduce the dimensionless Reynolds number

$$Re = \frac{L^* U^*}{\nu} \quad (2.50)$$

and drop the primes to simplify notation, we immediately obtain the dimensionless Navier-Stokes equations defined on Φ :

$$\begin{aligned} \frac{D^A}{Dt} \mathbf{u} + \left[(\mathbf{u} - \mathbf{w}) \cdot \nabla \right] \mathbf{u} + \nabla p - \frac{1}{Re} \Delta \mathbf{u} &= 0 \\ \text{div } \mathbf{u} &= 0 . \end{aligned} \quad (2.51)$$

2.2 Numerical solution

The Navier-Stokes equations were solved using the finite element method. All the code was programmed in Fortran77, making use of the free, open-source numerical library *Mélima*, developed at Université de Rennes and Unité de Mathématiques Appliquées, ENSTA Paris.

2.2.1 Solution of the coupled problem

The Navier-Stokes equations (2.37) together with the equations of motion (2.9) form a full coupled system describing the fluid-structure interaction in the vocal folds. Since such mixed system of partial and ordinary differential equations is not suitable to be solved directly by some standard numerical scheme, it is convenient to begin with the time-semidiscretization of the Navier-Stokes equations and discretization of the equations of motion, both with the same timestep τ . In our case, the ALE-derivative in the Navier-Stokes equations was approximated by a second-order backward difference, and the equations of motion were discretized using the fourth-order Runge-Kutta method. Further, the following procedure is applied:

Assuming that the solution of the Navier-Stokes equations (2.37) on a specific time level t and domain Ω_t is known (or using the data specified in the initial condition for $t = 0$), the generalized excitation forces are calculated. In the case of the simple 2-DOF system described in section 2.1.1, the horizontal motion is blocked and the generalized forces are represented by the vertical forces F_1, F_2 (see Fig. 2.1). These forces can be calculated from the force and momentum conditions

$$F_1 + F_2 = F_f \quad (2.52)$$

$$F_1 (L_1 - l) + F_2 (L_1 + l) = M_f, \quad (2.53)$$

which immediately yield

$$F_1 = \frac{F_f (l + L_1) - M_f}{2l} \quad (2.54)$$

$$F_2 = \frac{F_f (l - L_1) + M_f}{2l} . \quad (2.55)$$

The total vertical force F_f and momentum M_f , by which the fluid acts on the bottom vocal fold, is given by the integration of the stress vector $\boldsymbol{\tau}$, similarly as in (2.34):

$$F_f = \int_{\Gamma_{VF}^b} \tau_2 d\sigma = \int_{\Gamma_{VF}^b} \sum_{j=1}^2 \mathbb{T}_{2j} n_j d\sigma, \quad (2.56)$$

$$\begin{aligned} M_f &= \int_{\Gamma_{VF}^b} \sum_{j,k=1}^2 \epsilon_{3jk} \tau_j x_k d\sigma = \int_{\Gamma_{VF}^b} \sum_{j,k,l=1}^2 \epsilon_{3jk} \mathbb{T}_{jl} n_l x_k d\sigma = \\ &= \int_{\Gamma_{VF}^b} \sum_{l=1}^2 \left(\mathbb{T}_{1l} n_l x_2 - \mathbb{T}_{2l} n_l x_1 \right) d\sigma. \end{aligned} \quad (2.57)$$

Here \mathbb{T} is the stress tensor, \mathbf{n} the unit outer normal to the vocal fold surface and ϵ_{ijk} the Levi-Civita symbol. For the definition of the integration domain Γ_{VF}^b see Fig. 2.2. The stress tensor \mathbb{T} is calculated from the pressure and velocity fields $p(t, x)$ and $\mathbf{u}(t, x)$ on time level t , according to the constitutive relation (2.35) valid for Newtonian fluids.

Once the excitation forces F_1 and F_2 are known, we can proceed to the next time level $t + \tau$ by performing one step of the Runge-Kutta method in the time-discretized equations of motion. In this way, we get the new system coordinates $w_i(t + \tau)$, $i = 1..2$ (or $q_i(t + \tau)$, $i = 1..n$ in the general n -DOF case). These coordinates uniquely determine the shape of the domain $\Omega_{t+\tau}$. With the knowledge of the solution from the previous two time levels, the Navier-Stokes equations can be solved on the new time level $t + \tau$ and new domain $\Omega_{t+\tau}$ using the finite element method.

It is evident that within this numerical scheme, there is no essential difference between the solution of the coupled system (fluid-structure interaction), and the solution in the case of externally driven vibrations, i.e. prescribed vocal fold motion. All, what is necessary in the coupled system, is to calculate the generalized forces and solve numerically an additional small system of ordinary differential equations, which is not so complicated in comparison to the difficulties encountered in finite element solution of the nonlinear Navier-Stokes equations. Though, modeling of the coupled oscillations brings several technical challenges, which are not easy to overcome:

First, it is not obvious which kinematic vocal fold model to use. Obviously, the more degrees of freedom modeled, the closer to reality the model can be, but the more elastic and damping constants are needed to design the dynamic model. However, these constants are not known, and very difficult or even impossible to obtain experimentally.

What is more, it is by no means guaranteed, that the model actually encounters the self-oscillation regime. Unlike many technical systems, where flow-induced vibrations represent an undesirable phenomenon which is rather difficult to suppress (e.g. bridge-deck wind-induced vibrations, airfoil flutter), the vibration of vocal folds is a result of a long-term evolution and occurs only in very special conditions. It has been experienced in the measurements on physical vocal fold models [33] and excised human larynges [41] that it is indeed not trivial to adjust the geometry, elastic properties and other parameters so that the oscillations occur.

Taking all this into account, it seems reasonable to perform the first computations using the model with externally driven vibration. The results shown within this study were calculated in this mode – with prescribed motion of the vocal fold.

2.2.2 Time discretization of the Navier-Stokes equations

The time discretization is based on the works of Sváček, Feistauer and Horáček [38, 39]. A constant timestep τ will be used. Let us define the discrete time level $t_i = i \tau$ and the approximate flow velocity, pressure and domain velocity on this time level

$$\mathbf{u}^i(\mathbf{x}) \approx \mathbf{u}(t_i, \mathbf{x}), \quad p^i(x) \approx p(t_i, \mathbf{x}), \quad \mathbf{w}^i(x) \approx \mathbf{w}(t_i, \mathbf{x}), \quad \mathbf{x} \in \Omega_{t_i}. \quad (2.58)$$

The Eulerian time derivative $\partial \mathbf{u} / \partial t$ can be approximated by second-order backward difference

$$\frac{\partial \mathbf{u}}{\partial t}(t_{n+1}, \mathbf{x}) \approx \frac{3 \mathbf{u}(t_{n+1}, \mathbf{x}) - 4 \mathbf{u}(t_n, \mathbf{x}) + \mathbf{u}(t_{n-1}, \mathbf{x})}{2 \tau}. \quad (2.59)$$

On the basis of the solutions from previous time levels t_n and t_{n-1} , an explicit two-step scheme can be constructed. In the ALE-formulated Navier-Stokes equations (2.37), however, we use the ALE-derivative

$$\frac{D^A}{Dt} \mathbf{u}(t_{n+1}, \mathbf{x}) = \frac{\partial}{\partial t} \tilde{\mathbf{u}}(t_{n+1}, \mathbf{X}), \quad \mathbf{X} = A_{t_{n+1}}^{-1}(\mathbf{x}), \quad \mathbf{x} \in \Omega_{t_{n+1}}. \quad (2.60)$$

The point \mathbf{X} of the reference configuration will be helpful for the construction of the approximation of the ALE-derivative. Let us denote the ALE-maps of the reference point \mathbf{X} on the three time levels involved

$$\mathbf{x}^{n+1} = A_{t_{n+1}}(\mathbf{X}), \quad \mathbf{x}^n = A_{t_n}(\mathbf{X}), \quad \mathbf{x}^{n-1} = A_{t_{n-1}}(\mathbf{X}). \quad (2.61)$$

Then, similarly as in (2.59), the ALE-derivative can be approximated by the formula

$$\begin{aligned} \frac{D^A \mathbf{u}}{Dt}(t_{n+1}, \mathbf{x}_{n+1}) &\approx \frac{3 \mathbf{u}^{n+1}(\mathbf{x}_{n+1}) - 4 \mathbf{u}^n(\mathbf{x}_n) + \mathbf{u}^{n-1}(\mathbf{x}_{n-1})}{2 \tau} = \\ &= \frac{3 \mathbf{u}^{n+1}(\mathbf{x}_{n+1}) - 4 \mathbf{u}^n(A_{t_n}(A_{t_{n+1}}^{-1}(\mathbf{x}_{n+1}))) + \mathbf{u}^{n-1}(A_{t_{n-1}}(A_{t_{n+1}}^{-1}(\mathbf{x}_{n+1})))}{2 \tau}. \end{aligned} \quad (2.62)$$

Provided that the ALE-mappings on time levels t_{n+1} , t_n and t_{n-1} are known, the finite difference (2.62) is now well-defined on $\Omega_{t_{n+1}}$. When we introduce the notation

$$\hat{\mathbf{u}}^i(\mathbf{x}^{n+1}) = \mathbf{u}^i(A_{t_i}(A_{t_{n+1}}^{-1}(\mathbf{x}_{n+1}))), \quad (2.63)$$

by substituting (2.62) into (2.37) we get the semidiscrete Navier-Stokes equations for the functions $\mathbf{u}^{n+1} : \Omega_{t_{n+1}} \mapsto \mathbb{R}^2$ and $p^{n+1} : \Omega_{t_{n+1}} \mapsto \mathbb{R}$:

$$\begin{aligned} \frac{3 \mathbf{u}^{n+1}}{2 \tau} + [(\mathbf{u}^{n+1} - \mathbf{w}^{n+1}) \cdot \nabla] \mathbf{u}^{n+1} + \nabla p^{n+1} - \nu \Delta \mathbf{u}^{n+1} &= \frac{4 \hat{\mathbf{u}}^n - \hat{\mathbf{u}}^{n-1}}{2 \tau} \\ \operatorname{div} \mathbf{u}^{n+1} &= 0. \end{aligned} \quad (2.64)$$

2.2.3 Linearization of the convective term - Oseen iterations

Due to the presence of the convective term $[(\mathbf{u}^{n+1} - \mathbf{w}^{n+1}) \cdot \nabla] \mathbf{u}^{n+1}$ in the Navier-Stokes equations (2.64), the system cannot be solved in a straightforward way. Instead, it is first necessary to linearize the equations, i.e. to replace the first occurrence of the sought velocity vector \mathbf{u}^{n+1} by some vector \mathbf{u}^* , which is already known:

$$[(\mathbf{u}^{n+1} - \mathbf{w}^{n+1}) \cdot \nabla] \mathbf{u}^{n+1} \approx [(\mathbf{u}^* - \mathbf{w}^{n+1}) \cdot \nabla] \mathbf{u}^{n+1}. \quad (2.65)$$

As regards the approximation vector \mathbf{u}^* , one possible approach is to use the solution from the previous timestep \mathbf{u}^n , transformed to the actual configuration with the aid of the ALE-mapping (see 2.63):

$$\mathbf{u}^* = \hat{\mathbf{u}}^n. \quad (2.66)$$

This would be sufficient for quasi-steady flows; to increase precision for the non-stationary flow it is better to employ an iteration process, using (2.66) as the zero iteration. The m^{th} iteration of the so-called Oseen iteration process is performed by solving the system

$$\begin{aligned} \frac{3 \mathbf{u}_m^{n+1}}{2 \tau} + [(\mathbf{u}_m^{n+1} - \mathbf{w}^{n+1}) \cdot \nabla] \mathbf{u}_m^{n+1} + \nabla p^{n+1} - \nu \Delta \mathbf{u}_m^{n+1} &= \frac{4 \hat{\mathbf{u}}^n - \hat{\mathbf{u}}^{n-1}}{2 \tau} \\ \operatorname{div} \mathbf{u}_m^{n+1} &= 0. \end{aligned} \quad (2.67)$$

Using the notation

$$\mathbf{u} \equiv \mathbf{u}^{n+1}, \quad \mathbf{w} \equiv \mathbf{w}^{n+1}, \quad p \equiv p^{n+1}, \quad \Omega \equiv \Omega_{t_{n+1}} \quad (2.68)$$

to simplify the equations, the Oseen system can be formally rewritten as

$$\begin{aligned} \frac{3 \mathbf{u}}{2 \tau} + [(\mathbf{u}^* - \mathbf{w}) \cdot \nabla] \mathbf{u} + \nabla p - \nu \Delta \mathbf{u} &= \frac{4 \hat{\mathbf{u}}^n - \hat{\mathbf{u}}^{n-1}}{2 \tau} \\ \operatorname{div} \mathbf{u} &= 0. \end{aligned} \quad (2.69)$$

2.2.4 Weak formulation of the Navier-Stokes equations

The starting point for the finite element discretization of any system of partial differential equations is its weak formulation. The *weak solution* of a partial differential equation may be understood as a generalization of the concept of *classical solutions*, whose derivatives concerned must exist everywhere in the computational domain Ω . The weak solution, on the other hand, is defined in an “integral” sense. It should be stated that the concept of weak solutions remains consistent with the classical theory: it can be proven that a weak solution, which is sufficiently regular, is also a solution in the classical sense.

In order to derive the weak formulation of the Navier-Stokes equations, several spaces used in functional analysis shall be needed. First, let us recall the Lebesgue space of measurable square-integrable functions defined on $\Omega \equiv \Omega_{t_{n+1}} \subset \mathbb{R}^2$:

$$L^2(\Omega) = \left\{ f : \Omega \mapsto \mathbb{R} \text{ measurable} : \sqrt[2]{\int_{\Omega} |f|^2 d\mu} < \infty \right\}. \quad (2.70)$$

The Lebesgue space $L^2(\Omega)$ will be used for the pressure component of the solution. As regards the velocity, the solution will be sought in the Sobolev space $\mathbf{Y} = (H^1(\Omega))^2$, where

$$H^1(\Omega) = \left\{ f \in L^2(\Omega) : \frac{\partial f}{\partial x_i} \in L^2(\Omega), i = 1, 2 \right\}. \quad (2.71)$$

See e.g. [12] for details.

Now we will define the velocity and pressure test function space \mathbf{W} and Q , respectively. The velocity test functions are zero on the boundaries, where the Dirichlet condition is prescribed:

$$\mathbf{W} = \left\{ \mathbf{v} \in \mathbf{Y} : \mathbf{v}|_{\Gamma_{in} \cup \Gamma_{wall} \cup \Gamma_{VF}} = 0 \right\} \quad (2.72)$$

$$Q = L^2(\Omega). \quad (2.73)$$

The weak formulation of the equations is obtained by multiplying the classical formulation (2.69) by an arbitrary test function from the relevant space and integrating over Ω :

$$\begin{aligned} \frac{3}{2\tau} \int_{\Omega} \mathbf{u} \cdot \mathbf{v} d\mathbf{x} + \int_{\Omega} \left([(\mathbf{u}^* - \mathbf{w}) \cdot \nabla] \mathbf{u} \right) \cdot \mathbf{v} d\mathbf{x} + \int_{\Omega} \nabla p \cdot \mathbf{v} d\mathbf{x} - \\ \int_{\Omega} \nu \Delta \mathbf{u} \cdot \mathbf{v} d\mathbf{x} = \frac{1}{2\tau} \int_{\Omega} \left(4\hat{\mathbf{u}}^n - \hat{\mathbf{u}}^{n-1} \right) \cdot \mathbf{v} d\mathbf{x} \quad \forall \mathbf{v} \in \mathbf{W}, \end{aligned} \quad (2.74)$$

$$\int_{\Omega} q \operatorname{div} \mathbf{u} d\mathbf{x} = 0 \quad \forall q \in Q. \quad (2.75)$$

Using Green's theorem and the fact, that the test functions \mathbf{v} are zero on $\partial\Omega \setminus \Gamma_{out}$, we can rewrite the third and fourth term from (2.74)

$$\begin{aligned}
& \int_{\Omega} \nabla p \cdot \mathbf{v} \, d\mathbf{x} - \int_{\Omega} \nu \Delta \mathbf{u} \cdot \mathbf{v} \, d\mathbf{x} = \\
& = \int_{\partial\Omega} p \mathbf{v} \cdot \mathbf{n} \, d\sigma - \int_{\Omega} p \operatorname{div} \mathbf{v} \, d\mathbf{x} + \nu \sum_{j=1}^2 \int_{\Omega} \nabla u_j \cdot \nabla v_j \, d\mathbf{x} - \nu \sum_{j=1}^2 \int_{\partial\Omega} \nabla u_j \cdot \mathbf{n} v_j \, d\sigma = \\
& = \nu \int_{\Omega} \nabla \mathbf{u} \cdot \nabla \mathbf{v} \, d\mathbf{x} - \int_{\Omega} p \operatorname{div} \mathbf{v} \, d\mathbf{x} + \int_{\Gamma_{out}} \left(-\nu \frac{\partial \mathbf{u}}{\partial \mathbf{n}} + p \mathbf{n} \right) \cdot \mathbf{v} \, d\sigma. \tag{2.76}
\end{aligned}$$

The last surface integral in (2.76) reveals the origin of the boundary condition on the outlet of the channel (2.41); the do-nothing condition actually represents a natural condition coming from the weak formulation. In certain cases, however, this condition becomes too vague – it does not even prevent the flow returning to the domain Ω through Γ_{out} . Thus, the total influx into the domain Ω can grow infinite and the numerical scheme tends to diverge.

To suppress this inconvenience, the boundary condition on Γ_{out} can be slightly modified. First, it is necessary to apply Green's theorem on the second, convective term in (2.74). If we realize that

$$\mathbf{v} \Big|_{\partial\Omega \setminus \Gamma_{out}} = 0, \quad \mathbf{w} \Big|_{\partial\Omega \setminus \Gamma_{VF}} = 0, \tag{2.77}$$

we can write:

$$\begin{aligned}
& \int_{\Omega} \left(\left[(\mathbf{u}^* - \mathbf{w}) \cdot \nabla \right] \mathbf{u} \right) \cdot \mathbf{v} \, d\mathbf{x} = \sum_{i,j=1}^2 \int_{\Omega} (u_i^* - w_i) \frac{\partial u_j}{\partial x_i} v_j \, d\mathbf{x} = \\
& = \sum_{i,j=1}^2 \left[\frac{1}{2} \int_{\Omega} (u_i^* - w_i) \frac{\partial u_j}{\partial x_i} v_j \, d\mathbf{x} + \frac{1}{2} \int_{\Omega} (u_i^* - w_i) \frac{\partial u_j}{\partial x_i} v_j \, d\mathbf{x} \right] = \\
& = \sum_{i,j=1}^2 \left[\frac{1}{2} \int_{\Omega} (u_i^* - w_i) \frac{\partial u_j}{\partial x_i} v_j \, d\mathbf{x} + \frac{1}{2} \int_{\partial\Omega} v_j (u_i^* - w_i) u_j n_i \, d\sigma \right. \\
& \quad \left. - \frac{1}{2} \int_{\Omega} u_j \frac{\partial}{\partial x_i} \left[(u_i^* - w_i) v_j \right] \, d\mathbf{x} \right] = \\
& = \sum_{i,j=1}^2 \left[\frac{1}{2} \int_{\Omega} (u_i^* - w_i) \frac{\partial u_j}{\partial x_i} v_j \, d\mathbf{x} + \frac{1}{2} \int_{\Gamma_{out}} v_j u_i^* u_j n_i \, d\sigma \right. \\
& \quad \left. - \frac{1}{2} \int_{\Omega} u_j v_j \frac{\partial}{\partial x_i} (u_i^* - w_i) \, d\mathbf{x} - \frac{1}{2} \int_{\Omega} u_j (u_i^* - w_i) \frac{\partial v_j}{\partial x_i} \, d\mathbf{x} \right] =
\end{aligned}$$

$$\begin{aligned}
&= \frac{1}{2} \int_{\Omega} \left(\left[(\mathbf{u}^* - \mathbf{w}) \cdot \nabla \right] \mathbf{u} \right) \cdot \mathbf{v} \, d\mathbf{x} + \frac{1}{2} \int_{\Gamma_{out}} (\mathbf{u}^* \cdot \mathbf{n}) \mathbf{u} \cdot \mathbf{v} \, d\sigma \\
&\quad - \frac{1}{2} \int_{\Omega} \mathbf{u} \cdot \mathbf{v} \operatorname{div} (\mathbf{u}^* - \mathbf{w}) \, d\mathbf{x} - \frac{1}{2} \int_{\Omega} \left(\left[(\mathbf{u}^* - \mathbf{w}) \cdot \nabla \right] \mathbf{v} \right) \cdot \mathbf{u} \, d\mathbf{x} . \quad (2.78)
\end{aligned}$$

The continuity equation $\operatorname{div} \mathbf{u} = 0$ holds also for \mathbf{u}^* . Thus, with the aid of the Green's theorem, the third term in the result of (2.78) can be rewritten as

$$\begin{aligned}
&-\frac{1}{2} \int_{\Omega} \mathbf{u} \cdot \mathbf{v} \operatorname{div} (\mathbf{u}^* - \mathbf{w}) \, d\mathbf{x} = \frac{1}{2} \int_{\Omega} \sum_{i,j=1}^2 u_i v_i \frac{\partial w_j}{\partial x_j} = \\
&= \frac{1}{2} \sum_{i,j=1}^2 \left[\int_{\partial\Omega} u_i v_i w_j n_j \, d\sigma - \int_{\Omega} w_j \frac{\partial}{\partial x_j} (u_i v_i) \, d\mathbf{x} \right] = -\frac{1}{2} \int_{\Omega} \left[\mathbf{w} \cdot \nabla \right] (\mathbf{u} \cdot \mathbf{v}) \, d\mathbf{x} = \\
&= -\frac{1}{2} \int_{\Omega} \left(\left[\mathbf{w} \cdot \nabla \right] \mathbf{u} \right) \cdot \mathbf{v} \, d\mathbf{x} - \frac{1}{2} \int_{\Omega} \left(\left[\mathbf{w} \cdot \nabla \right] \mathbf{v} \right) \cdot \mathbf{u} \, d\mathbf{x} . \quad (2.79)
\end{aligned}$$

The boundary integral in (2.79) was dropped since on each part of the boundary $\partial\Omega$ either the flow velocity u_i , the velocity test functions v_i or the domain velocity w_j is zero. Substituting (2.79) back into (2.78) we finally receive

$$\begin{aligned}
&\int_{\Omega} \left(\left[(\mathbf{u}^* - \mathbf{w}) \cdot \nabla \right] \mathbf{u} \right) \cdot \mathbf{v} \, d\mathbf{x} = \\
&\quad \frac{1}{2} \int_{\Omega} \left(\left[(\mathbf{u}^* - 2\mathbf{w}) \cdot \nabla \right] \mathbf{u} \right) \cdot \mathbf{v} \, d\mathbf{x} - \frac{1}{2} \int_{\Omega} \left(\left[\mathbf{u}^* \cdot \nabla \right] \mathbf{v} \right) \cdot \mathbf{u} \, d\mathbf{x} + \frac{1}{2} \int_{\Gamma_{out}} (\mathbf{u}^* \cdot \mathbf{n}) \mathbf{u} \cdot \mathbf{v} \, d\sigma . \quad (2.80)
\end{aligned}$$

The new boundary integral which arose in (2.80) can be separated into the positive and negative parts:

$$\frac{1}{2} \int_{\Gamma_{out}} (\mathbf{u}^* \cdot \mathbf{n}) \mathbf{u} \cdot \mathbf{v} \, d\sigma = \frac{1}{2} \int_{\Gamma_{out}} (\mathbf{u}^* \cdot \mathbf{n})^+ \mathbf{u} \cdot \mathbf{v} \, d\sigma + \frac{1}{2} \int_{\Gamma_{out}} (\mathbf{u}^* \cdot \mathbf{n})^- \mathbf{u} \cdot \mathbf{v} \, d\sigma . \quad (2.81)$$

Since we wish to suppress the return flow, that is

$$(\mathbf{u}^* \cdot \mathbf{n})^- \Big|_{\Gamma_{out}} = 0 , \quad (2.82)$$

we add the negative part to the boundary condition and leave the positive term in the weak formulation. The new, more stable boundary condition on Γ_{out} , sometimes referred to as the *downstream boundary condition* [5, 16], now reads

$$-\nu \frac{\partial \mathbf{u}}{\partial \mathbf{n}}(t, \mathbf{x}) + p(t, \mathbf{x}) \mathbf{n}(\mathbf{x}) + \frac{1}{2} (\mathbf{u}^*(\mathbf{x}) \cdot \mathbf{n}(\mathbf{x}))^- \mathbf{u}(t, \mathbf{x}) = p_{ref} \mathbf{n}(\mathbf{x})$$

$$\text{for } \mathbf{x} \in \Gamma_{out}, t \in [0, T]. \quad (2.83)$$

If we substitute back all the results (2.76), (2.80), (2.81) into the equations (2.74), (2.75) and make use of the downstream boundary condition (2.83), we can express the ultimate form of the weak semidiscretized ALE Navier-Stokes equations:

$$\begin{aligned} & \frac{3}{2\tau} \int_{\Omega} \mathbf{u} \cdot \mathbf{v} \, d\mathbf{x} + \nu \int_{\Omega} \nabla \mathbf{u} \cdot \nabla \mathbf{v} \, d\mathbf{x} - \int_{\Omega} p \operatorname{div} \mathbf{v} \, d\mathbf{x} + \frac{1}{2} \int_{\Omega} \left([(\mathbf{u}^* - 2\mathbf{w}) \cdot \nabla] \mathbf{u} \right) \cdot \mathbf{v} \, d\mathbf{x} \\ & \quad - \frac{1}{2} \int_{\Omega} \left([\mathbf{u}^* \cdot \nabla] \mathbf{v} \right) \cdot \mathbf{u} \, d\mathbf{x} + \frac{1}{2} \int_{\Gamma_{out}} (\mathbf{u}^* \cdot \mathbf{n})^+ \mathbf{u} \cdot \mathbf{v} \, d\mathbf{x} = \\ & = \frac{1}{2\tau} \int_{\Omega} \left(4\hat{\mathbf{u}}^n - \hat{\mathbf{u}}^{n-1} \right) \cdot \mathbf{v} \, d\mathbf{x} - \int_{\Gamma_{out}} p_{ref} \mathbf{v} \cdot \mathbf{n} \, d\sigma \quad \forall \mathbf{v} \in \mathbf{W}, \end{aligned} \quad (2.84)$$

$$- \int_{\Omega} q \operatorname{div} \mathbf{u} \, d\mathbf{x} = 0 \quad \forall q \in Q. \quad (2.85)$$

The weak solution of the problem is defined as a couple $(\mathbf{u}, p) \in \mathbf{Y} \times Q$ such that the weak Navier-Stokes equations (2.84), (2.85) hold and that the boundary conditions (2.38), (2.39), (2.40) and (2.83) are satisfied in the sense of traces.

To simplify notation, we may introduce the forms

$$\begin{aligned} a(U^*, U, V) &= \frac{3}{2\tau} (\mathbf{u}, \mathbf{v}) + \nu ((\mathbf{u}, \mathbf{v})) - (p, \operatorname{div} \mathbf{v}) + (\operatorname{div} \mathbf{u}, q) + \frac{1}{2} \left([(\mathbf{u}^* - 2\mathbf{w}) \cdot \nabla] \mathbf{u}, \mathbf{v} \right) \\ & \quad - \frac{1}{2} \left([\mathbf{u}^* \cdot \nabla] \mathbf{v}, \mathbf{u} \right) + \frac{1}{2} \int_{\Gamma_{out}} (\mathbf{u}^* \cdot \mathbf{n})^+ \mathbf{u} \cdot \mathbf{v} \, d\mathbf{x}, \end{aligned} \quad (2.86)$$

$$f(V) = \frac{1}{2\tau} \left(4\hat{\mathbf{u}}^n - \hat{\mathbf{u}}^{n-1}, \mathbf{v} \right) - \int_{\Gamma_{out}} p_{ref} \mathbf{v} \cdot \mathbf{n} \, d\sigma, \quad (2.87)$$

where $U = \{\mathbf{u}, p\}$, $U^* = \{\mathbf{u}^*, p\}$, $V = \{\mathbf{v}, q\}$, where $(\mathbf{u}, \mathbf{v}) = \int_{\Omega} \mathbf{u} \cdot \mathbf{v} \, d\mathbf{x}$ denotes the scalar product in $(L^2(\Omega))^2$ and $((\mathbf{u}, \mathbf{v})) = \int_{\Omega} \nabla \mathbf{u} \cdot \nabla \mathbf{v} \, d\mathbf{x}$ is the scalar product in $(H_0^1(\Omega))^2$. Using this notation, the problem can be formulated as follows:

Find $U = \{\mathbf{u}, p\} \in \mathbf{Y} \times Q$ such that the boundary conditions (2.38), (2.39), (2.40) and (2.83) are satisfied in the sense of traces and that

$$a(U^*, U, V) = f(V) \quad \forall V = \{\mathbf{v}, q\} \in \mathbf{W} \times Q. \quad (2.88)$$

2.2.5 FE discretization of the Navier-Stokes equations

To find an approximate solution of the semidiscrete weak Navier-Stokes equations (2.88) we shall use the finite element method. Let us suppose that the domain Ω is polygonal and denote $\Omega_h \equiv \Omega$ (otherwise, it would be necessary to construct a polygonal approximation Ω_h of the domain Ω), and that the boundary $\partial\Omega$ is Lipschitz-continuous. Let $\mathcal{T}_h = \{K_i\}_{i \in \{1..n_h\}}$ be a regular finite element mesh over Ω_h , which means that the elements K_i are closed polygons with mutually disjoint interiors such that

$$\overline{\Omega}_h = \bigcup_{i \in \{1..n_h\}} K_i \quad (2.89)$$

and that an intersection of arbitrary two elements is either empty or their common vertex or edge (see [12] for details). The subscript h usually represents the maximum diameter of all the elements,

$$h = \max_{i \in \{1..n_h\}} (\text{diam } K_i). \quad (2.90)$$

The velocity constituent of the approximate solution will be sought in the finite-dimensional space

$$\mathbf{Y}_h = \left\{ \mathbf{v}_h \in \left(C(\overline{\Omega}_h) \right)^2 : \mathbf{v}_h|_K \in P^{k+1}(K) \quad \forall K \in \mathcal{T}_h \right\}, \quad (2.91)$$

where $P^m(K)$ is the set of all polynomials defined on K of degree less than or equal to m . Similarly, the pressure constituent of the solution comes from the finite-dimensional space

$$Q_h = \left\{ q_h \in C(\overline{\Omega}_h) : q_h|_K \in P^k(K) \quad \forall K \in \mathcal{T}_h \right\}. \quad (2.92)$$

This means that the solution is approximated by continuous piecewise-polynomial functions; in other words, the spaces \mathbf{Y}_h, Q_h represent finite-dimensional approximations of the functional spaces \mathbf{Y}, Q . It can be anticipated that when decreasing the size of elements, i.e. for $h \rightarrow 0$, the approximation error diminishes and the approximate solution may converge to the exact solution.

It can be proven that $\mathbf{Y}_h \subset \mathbf{Y}, Q_h \subset Q$. The spaces \mathbf{Y}_h, Q_h are called the *finite element spaces*, the functions $\mathbf{v}_h \in \mathbf{Y}_h, p_h \in Q_h$ are sometimes referred to as *finite elements*. In order to guarantee the numerical stability of the resulting scheme, the spaces \mathbf{Y}_h, Q_h cannot be chosen arbitrarily; they

must fulfill the Babuška-Brezzi condition (see [11]). For the P^{k+1}/P^k elements (called Taylor-Hood elements), this condition holds.

The test functions in the discretized equations come from spaces $\mathbf{W}_h \subset \mathbf{W}$ and Q_h , where

$$\mathbf{W}_h = \left\{ v_h \in \mathbf{Y}_h : \mathbf{v}_h|_{\Gamma_{in} \cup \Gamma_{wall} \cup \Gamma_{VF}} = 0 \right\}. \quad (2.93)$$

Now we are able to formulate the discrete problem: find a couple $U_h = \{\mathbf{u}_h, p_h\} \in \mathbf{Y}_h \times Q_h$ satisfying (in the sense of traces) a suitable approximation of the boundary conditions (2.38), (2.39), (2.40) and (2.83) such, that

$$a(U_h^*, U_h, V_h) = f(V_h) \quad \forall V_h = \{\mathbf{v}_h, q_h\} \in \mathbf{W}_h \times Q_h. \quad (2.94)$$

For the purpose of clarity, the rest of the discretization process will be outlined here (without any claims on completeness):

First, it is necessary to construct the bases of the spaces \mathbf{Y}_h, Q_h . The basis of a n_h -dimensional space \mathbf{Y}_h will be denoted by $\{\mathbf{w}_i\}_{i=1}^{n_h}$, $\{q_i\}_{i=1}^{m_h}$ is the basis of the space Q_h of dimension m_h . In order to produce sparse matrices, it is suitable to choose basis functions with small support, i.e. for example equal to one in one vertex of the mesh and zero elsewhere (in the case of linear P^1 -elements).

Once the basis functions are chosen, the approximate solution can be expressed as their linear combination

$$\mathbf{u}_h = \sum_{j=1}^{n_h} U_j \mathbf{w}_j, \quad p_h = \sum_{j=1}^{m_h} P_j q_j. \quad (2.95)$$

If a relation holds for an arbitrary element of a space, it must hold for all the elements of the basis and vice versa. Thus, using (2.95), we can equivalently rewrite the condition (2.94) as

$$a\left(U_h^*, \left\{ \sum_{j=1}^{n_h} U_j \mathbf{w}_j, \sum_{r=1}^{m_h} P_r q_r \right\}, \{\mathbf{w}_k, q_l\}\right) = f(\{\mathbf{w}_k, q_l\}) \quad \forall k \in \{1..n_h\} \quad \forall l \in \{1..m_h\}. \quad (2.96)$$

We can assume that the vector U^* is known from the previous iteration of the Oseen process. Looking back on the definitions (2.86), (2.87) of the (tri)linear forms $a(U^*, U, V)$ and $f(V)$, it is obvious that the equations (2.96) represent a system of linear algebraic equations for $(n_h + m_h)$ unknown real coefficients, which can be organized into vectors $\mathbf{U} = (U_1 \dots U_{n_h})^T$ and $\mathbf{P} = (P_1 \dots P_{m_h})^T$.

The linear system, which arises from the finite element discretization described above, has the block structure

$$\begin{pmatrix} \mathbb{A} + \mathbb{T} + \mathbb{C} + \mathbb{D} + \mathbb{E} & \mathbb{B} \\ \mathbb{B}^T & \emptyset \end{pmatrix} \begin{pmatrix} \mathbf{U} \\ \mathbf{P} \end{pmatrix} = \begin{pmatrix} \mathbf{F} \\ \emptyset \end{pmatrix}, \quad (2.97)$$

where

$$\begin{aligned}
\mathbb{A} &= (a_{ij})_{i,j=1}^{n_h} & a_{ij} &= \nu \int_{\Omega} \nabla \mathbf{w}_j \cdot \nabla \mathbf{w}_i \, d\mathbf{x} \, , \\
\mathbb{T} &= (t_{ij})_{i,j=1}^{n_h} & t_{ij} &= \frac{3}{2\tau} \int_{\Omega} \mathbf{w}_j \cdot \mathbf{w}_i \, d\mathbf{x} \, , \\
\mathbb{C} &= (c_{ij})_{i,j=1}^{n_h} & c_{ij} &= \frac{1}{2} \int_{\Omega} \left([(\mathbf{u}^* - 2\mathbf{w}) \cdot \nabla] \mathbf{w}_j \right) \cdot \mathbf{w}_i \, d\mathbf{x} \, , \\
\mathbb{D} &= (d_{ij})_{i,j=1}^{n_h} & d_{ij} &= -\frac{1}{2} \int_{\Omega} \left([\mathbf{u}^* \cdot \nabla] \mathbf{w}_i \right) \cdot \mathbf{w}_j \, d\mathbf{x} \, , \\
\mathbb{E} &= (e_{ij})_{i,j=1}^{n_h} & e_{ij} &= \frac{1}{2} \int_{\Gamma_{out}} (\mathbf{u}^* \cdot \mathbf{n})^+ \mathbf{w}_j \cdot \mathbf{w}_i \, d\sigma \, , \\
\mathbb{B} &= (b_{ij})_{i=1, j=1}^{n_h, m_h} & b_{ij} &= - \int_{\Omega} q_j \operatorname{div} \mathbf{w}_i \, d\mathbf{x} \, , \\
\mathbf{F} &= (f_1 \dots f_{n_h})^T & f_i &= \frac{1}{2\tau} \int_{\Omega} (4 \hat{\mathbf{u}}^n - \hat{\mathbf{u}}^{n-1}) \cdot \mathbf{w}_i \, d\mathbf{x} - \int_{\Gamma_{out}} p_{ref} \mathbf{w}_i \cdot \mathbf{n} \, d\sigma \, .
\end{aligned} \tag{2.98}$$

The matrices \mathbb{A} and \mathbb{T} , coming from the discretization of the viscous term and of the temporal derivative, are symmetric, while \mathbb{C} , \mathbb{D} (from the convective terms), \mathbb{E} and \mathbb{B} are generally nonsymmetric. By the symbol \emptyset we denote the zero matrix or vector.

Before solving the linear system (2.97) it is necessary to take into account the Dirichlet boundary conditions (2.38), (2.39), (2.40). The principle of the algorithm can be illustrated on a generic linear system

$$\mathbb{M}\boldsymbol{\varphi} = \mathbf{b} \tag{2.99}$$

with a matrix $\mathbb{M} = (m_{ij})_{i,j=1}^n$ and a second member $\mathbf{b} = (b_1 \dots b_n)^T$. Imposing the Dirichlet condition is equivalent to blocking some of the degrees of freedom, i.e. to setting

$$\varphi_j = g_j \quad \forall j \in \mathcal{D} \, , \tag{2.100}$$

where g_j are prescribed values and \mathcal{D} is an index set of the blocked (Dirichlet) nodes. We will assume that the linear system has already been organized in such a way, that the diagonal elements corresponding to non-Dirichlet nodes are non-zero, $m_{ii} \neq 0 \quad \forall i \notin \mathcal{D}$.

In order to satisfy the Dirichlet conditions, the original system (2.99) is modified as follows: first the components of the right-hand side vector \mathbf{b} corresponding to the non-Dirichlet nodes are replaced by the values

$$b_i := b_i - \sum_{j \in \mathcal{D}} m_{ij} g_j \quad \forall i \notin \mathcal{D} \, . \tag{2.101}$$

Then, the matrix elements in the relevant columns are set to zero,

$$m_{ij} := 0 \quad \forall i \quad \forall j \in \mathcal{D}. \quad (2.102)$$

Finally, the matrix rows corresponding to the Dirichlet nodes are modified as follows:

$$\begin{aligned} m_{ij} &:= 0 & \forall i \in \mathcal{D} \quad \forall j \neq i, \\ m_{ii} &:= 1 & \forall i \in \mathcal{D}, \\ b_i &:= g_i & \forall i \in \mathcal{D}. \end{aligned} \quad (2.103)$$

2.2.6 ALE mapping

There is still one term in the Navier-Stokes equations (2.84) which has not yet been discussed properly: the domain velocity w . According to the definitions (2.16), (2.17), the domain velocity is simply the time derivative of the ALE-mapping A_t . Our task is to determine the explicit form of the ALE-mapping $A_t(\mathbf{X})$ at time level t , provided that the generalized coordinates $q_i^b(t)$ and $q_i^u(t)$ of the bottom and upper vocal folds (and thus the shape of the domain Ω_t) are known.

Let us remind that A_t maps the reference, non-deformed domain Ω_0 onto the actual, deformed domain Ω_t . Looking on Figs. 2.2, 2.3, it is obvious that the ALE-mapping must satisfy following conditions on $\partial\Omega_0$:

$$A_t \Big|_{\Gamma_{in} \cup \Gamma_{wall} \cup \Gamma_{out}} = Id, \quad A_t \Big|_{\Gamma_{VF}} = F_t(\mathbf{X}), \quad (2.104)$$

where Id is the identity mapping (these boundaries do not move) and where F_t is a prescribed explicit function of the generalized coordinates $q_i^b, q_j^u, i = 1..N_{DOF}^b, j = 1..N_{DOF}^u$ modeling the motion of the vocal fold surface. In the case of the simple kinematic model shown in Fig. 2.1, the function F_t is given by shift and rotation of the rigid body in the central part, and by cubic spline interpolation on the side segments (membranes).

The second condition is that the mapping A_t must be smooth on Ω_t . Otherwise, however, the choice of A_t in the ALE approach is indeed arbitrary.

In simple cases, the form of the ALE-mapping may be guessed or derived on the basis of geometric considerations. Another possibility, which can be applied universally, is to seek the mapping A_t as a solution of an auxiliary boundary problem with a suitable operator. In the computations presented within this work, the ALE-mapping was defined as a solution of the Laplace's equation

$$\Delta A_t = 0 \quad \text{in } \Omega_0, \quad (2.105)$$

with the boundary conditions (2.104).

The system (2.105) must be numerically solved in each timestep of the computation. It might seem that this could slow down the algorithm considerably; however, it is necessary to realize that within one timestep, more Oseen iterations are performed, while the auxiliary problem (2.105) must be solved only once. Moreover, the finite element code programmed uses P^{k+1}/P^k elements for the velocity and pressure fields, resulting in much larger matrices than the P^k elements for the ALE-mapping A_t . Although the specific number depends on many factors, the practical computations show that the solution of the auxiliary problem takes at most 5-10% of the total computational time.

Fig. 2.4 shows the reference mesh in Ω_0 and two meshes deformed by the ALE-mapping A_t , which was calculated as the solution of the Laplace's equation (2.105). The deformed meshes correspond to two different time levels t_1, t_2 , near the maximum and minimum glottal aperture.

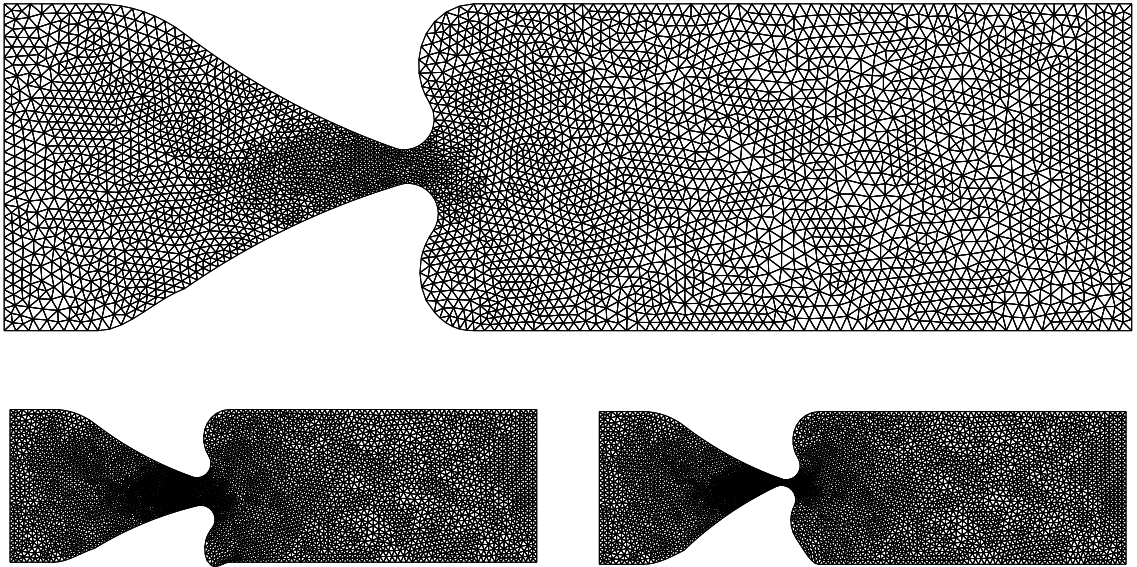


Figure 2.4: Reference (top) and deformed (bottom) computational meshes, 8246 elements.

2.2.7 Mesh generation and adaptive refinement

One of the advantages of the finite element method, against the finite difference method for example, is the possibility to use anisotropic or locally refined meshes in a straightforward way. It is obvious that in regions, where the solution is nearly constant, there is no need to apply a very fine mesh (the calculation times increase with the number of unknowns powered by a constant between 2-3, where the number of unknowns is a linear function of the number of mesh elements). In the domains where the solution is expected to have steep gradients and abrupt changes, on the contrary, a fine mesh is required in order to minimize the error of the discrete solution.

The adaptive mesh generator Angener [9] was used to create the meshes necessary for the finite element computations. The package Angener features triangular mesh generation on polygonal 2D domains. The solutions obtained with the primary, isotropic meshes can serve as a basis for adaptive mesh refinement, i.e. to create locally refined meshes, whose local element size is optimal

in the sense of minimizing the approximation error. Fig. 2.5 illustrates the difference between an isotropic and locally refined mesh.

In the case of vector-valued solutions, *Angener* requires to select one of the components, which will be used in the adaptive algorithm. For our calculations, the horizontal component of the velocity was chosen. Further, it was necessary to modify the *Angener* source code in order to obtain triangulation files in the format, which was required by the finite element library.

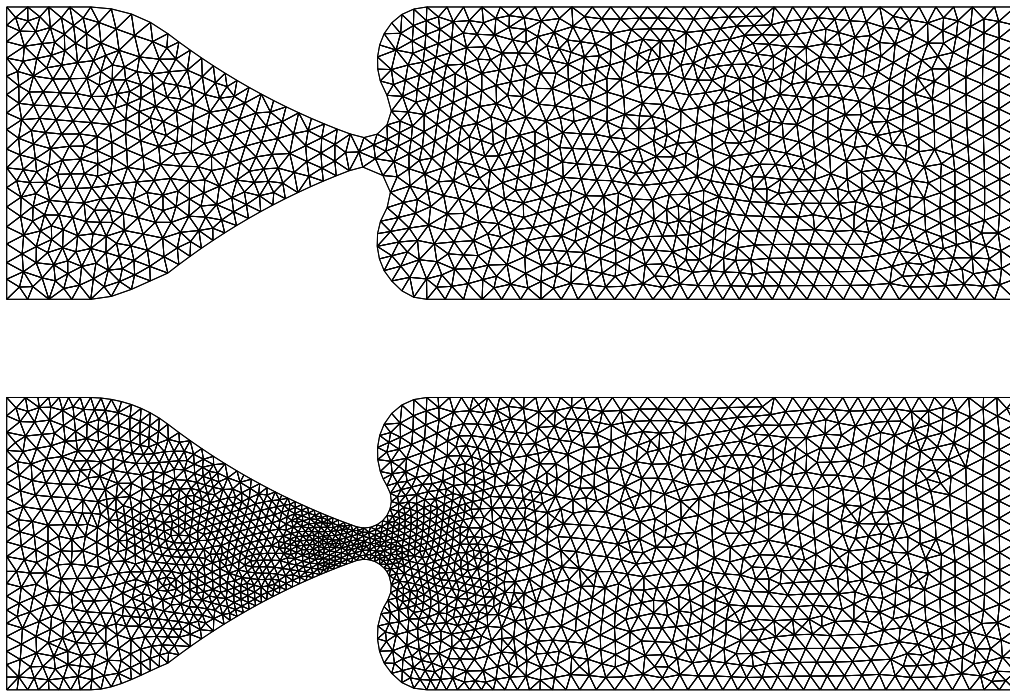


Figure 2.5: Isotropic and adaptively refined meshes, 2349 and 3988 elements, respectively. The mesh was adapted according to the horizontal component of the velocity vector from the solution obtained on the original mesh.

2.2.8 Algorithmic and technical remarks

The numerical solution of the discretized problem (2.94) was implemented using an open-source library *Mélina* [26] (the acronym comes from the French collocation for FEM – *Méthode des éléments finis*). The library, programmed under *Fortran77*, is not confined to a specific class of physical problems (like elasticity or viscous flow); it can deal with any partial differential problem. The initial point for the algorithm is the weak formulation of the governing equations. This can be specified in a file of directives together with the boundary conditions, physical constants involved, type of elements used (Lagrange/Gauss-Lobato P1 – P6, P1 & bubble P3, Q1 – Q20 interpolation supported) and link to the mesh file (triangular and quadrangular; tetrahedral, prismatic and hexahedral elements allowed).

The numerical library provides an extensive collection of high- and low-level routines, which allow to program the solution of simple problems without worrying about algorithmic details, such as discretization of the terms, assemblage of the matrices or even memory management. However, since all the source files are available and well-documented, the flow of execution is fully under control of the programmer and the routines can be modified to handle even non-standard problems – like, in our case, the Oseen iterations for the nonlinear term, the variable geometry and deforming mesh, additional boundary integrals arising from the modified convective term etc.

In outline, the flow chart of the code programmed is as follows:

- Execution of the *Mélina* initialization routines – import of the mesh file, parsing of the directives file, global numbering of the nodes
- Backup of the node coordinates for the reference (non-deformed) mesh
- Initialization of the matrix of the auxiliary problem (for the ALE-mapping)
- Beginning of the principal time loop – $i := 0$; $t := i * \tau$
 - Calculation of the coordinates of the vocal fold
 - Restoration of the reference mesh, assembly of the auxiliary problem matrix, resolution $\rightarrow A_t$
 - Deformation of the element vertices calculated on the basis of A_t , recalculation of the node coordinates
 - Beginning of the Oseen loop
 - * Recalculation of the convective and downstream-boundary terms based on the velocity vector field from last iteration
 - * Assemblage of the matrix of the Navier-Stokes problem
 - * Imposition of the Dirichlet boundary conditions
 - * Resolution of the linear problem
 - * Calculation of the residual in l^2 -norm
 - * Storage of the results into output files
 - End of the Oseen loop
 - Recalculation of the ALE-velocity and time derivative terms
- End of the principal time loop – $i := i + 1$

The direct linear solvers provided within *Mélina*, which use LU factorization, are not very efficient; this makes them applicable only on problems with small matrices. Therefore it was necessary to incorporate some more powerful external linear solver into *Mélina*.

The package *UMFPack* [7], which is used as a default sparse matrix solver in recent versions of *Matlab*, uses a direct multifrontal method, suitable for generally nonsymmetric sparse matrices.

Its performance may be further boosted by installation of a suitable BLAS (Basic Linear Algebra Subsystem) – for UMFPack the Goto’s version Goto BLAS [14] is recommended.

A new subroutine `umf.f` was developed to allow calling UMFPack within the Mélima code. This subroutine can simply replace built-in direct solvers `falu.f` and `fasv.f`, since it has identical input parameters. Basically, the interface works in the following way:

1. The matrix of the linear system is converted from the Mélima BiMorse format to the Nume-L format.
2. The Nume-L structure is converted to the zero-based compressed row format.
3. The matrix entries numerically equal to zero are suppressed to spare memory. Real values are stored in double precision in the superarray DST.
4. The matrix is passed through the Fortran interface of UMFPack, which performs the resolution itself in three steps (symbolic analysis, LU factorization, resolution of the factorized problem). UMFPack requires the compressed column matrix format, the matrix is supplied in compressed row format. Consequently, the solution is demanded for the transposed matrix (this is equivalent).
5. The solution is stored as a Mélima term.

In spite of the additional operations performed (matrix format conversions, array dislocations), the new method is essentially faster than the original subroutines, approximately by a factor of 100. On Intel processors, the overall performance of the binary code can be further improved by compiling UMFPack, Mélima libraries and the program source code with Intel Fortran Compiler (instead of GNU Fortran compiler, such as `f77` or `gfortran`), and by setting suitable optimization flags (on an Intel E6600 Core2 Duo system, `-xT -O3` flags were used).

2.3 Results

This chapter shows the sample results calculated within a numerical simulation using typical values of input parameters. These were as follows:

The channel geometry was based on the data measured on excised human larynges [34], scaled 1 : 4 to match the dimensions of the physical model. The glottal length in the model was $L_{02} = 67.22$ mm (see Fig. 2.6), the lengths of the channel $L_{01} = 0.25 \cdot L_{02} = 16.80$ mm, $L_{03} = 1.75 \cdot L_{02} = 117.63$ mm. The dimension L_{02} determines the part of the boundary, which changes in time: within the length of the vocal fold $L = 43.11$ mm, the boundary is given by the rotation and translation of the rigid body, outwards by smooth spline interpolation. The height of the channel was $H_0 = 37.50$ mm, the initial gap between the vocal folds $g = 4.00$ mm.

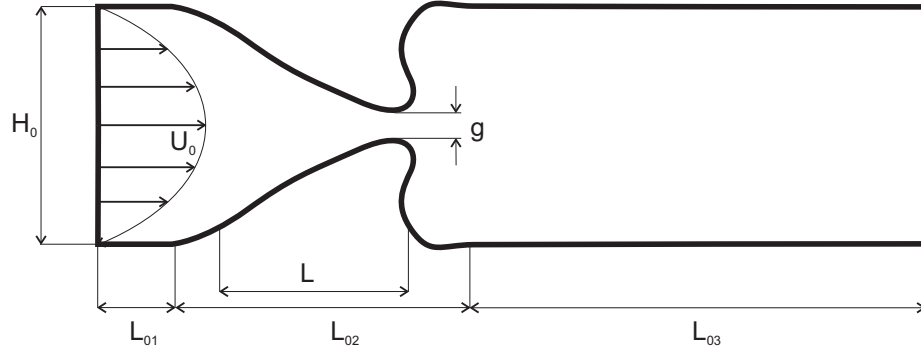


Figure 2.6: Dimensions in the mathematical model.

At the inlet Γ_{in} (see Fig. 2.2 for definitions of the boundary segments), the vertical component of the velocity vector was zero, $u_2 = 0$; the horizontal velocity component u_1 was prescribed as a parabolic profile with a maximum velocity $u_1^{max} = U_0 = 0.25$ m s⁻¹ at the channel axis, which gives a Reynolds number $Re = 680$. With the same mesh, the numerical scheme was stable for inlet flow velocities up to $U_0 = 1$ m s⁻¹. The reference pressure p_{ref} was set to zero, air viscosity $\nu = 1.583 \cdot 10^{-5}$ m² s⁻¹, air density $\rho = 1.1$ kg m⁻³.

The mesh was triangular and consisted of 16537 Taylor-Hood (P^2/P^1) elements. The upper vocal fold was fixed, the motion of the bottom one was prescribed as a harmonic oscillation of the vertical shift y and rotation ϕ around the center of the vocal fold

$$y = y_{max} \sin\left(y_0 + \frac{2\pi t}{T_y}\right), \quad \phi = \phi_{max} \sin\left(\phi_0 + \frac{2\pi t}{T_\phi}\right) \quad (2.106)$$

with amplitudes $y_{max} = 1.5$ mm, $\phi_{max} = 8$ deg, oscillation period $T_y = T_\phi = 100$ ms and phase difference $y_0 = 0$, $\phi_0 = -45$ deg. The timestep of the method was $\tau = 1$ ms; as regards the number of Oseen iterations, for typical Reynolds numbers $Re = 500 - 3000$ it was found sufficient to use a fixed number of iterations, usually two or three.

Fig. 2.7 demonstrates development of the velocity field in twelve phases over one vocal fold oscillation cycle of length T_c . We can observe the free jet, which is formed between the vocal folds and whose shear layer induces vortex shedding. It is quite common that the jet does not follow

the channel axis and that it adheres to the channel wall; this phenomenon is known as the Coanda effect. The flow is not perfectly periodical.

In Fig. 2.8 we can observe the development of the pressure field in the same phases of the oscillation cycle. The vortices appear as circular zones of low pressure, propagating towards the channel outlet.

Finally, a detailed view of the velocity field near the jet front, including the velocity vectors, is shown in Fig. 2.9. The figure reveals the large-scale vortices shedded from the jet boundary layer.

The mesh files, animations of the velocity and pressure fields generated from numerical simulations with $U_0 = 0.25, 0.5$ and 1.0 m/s and all the source code files can be found on the DVD enclosed to this thesis.

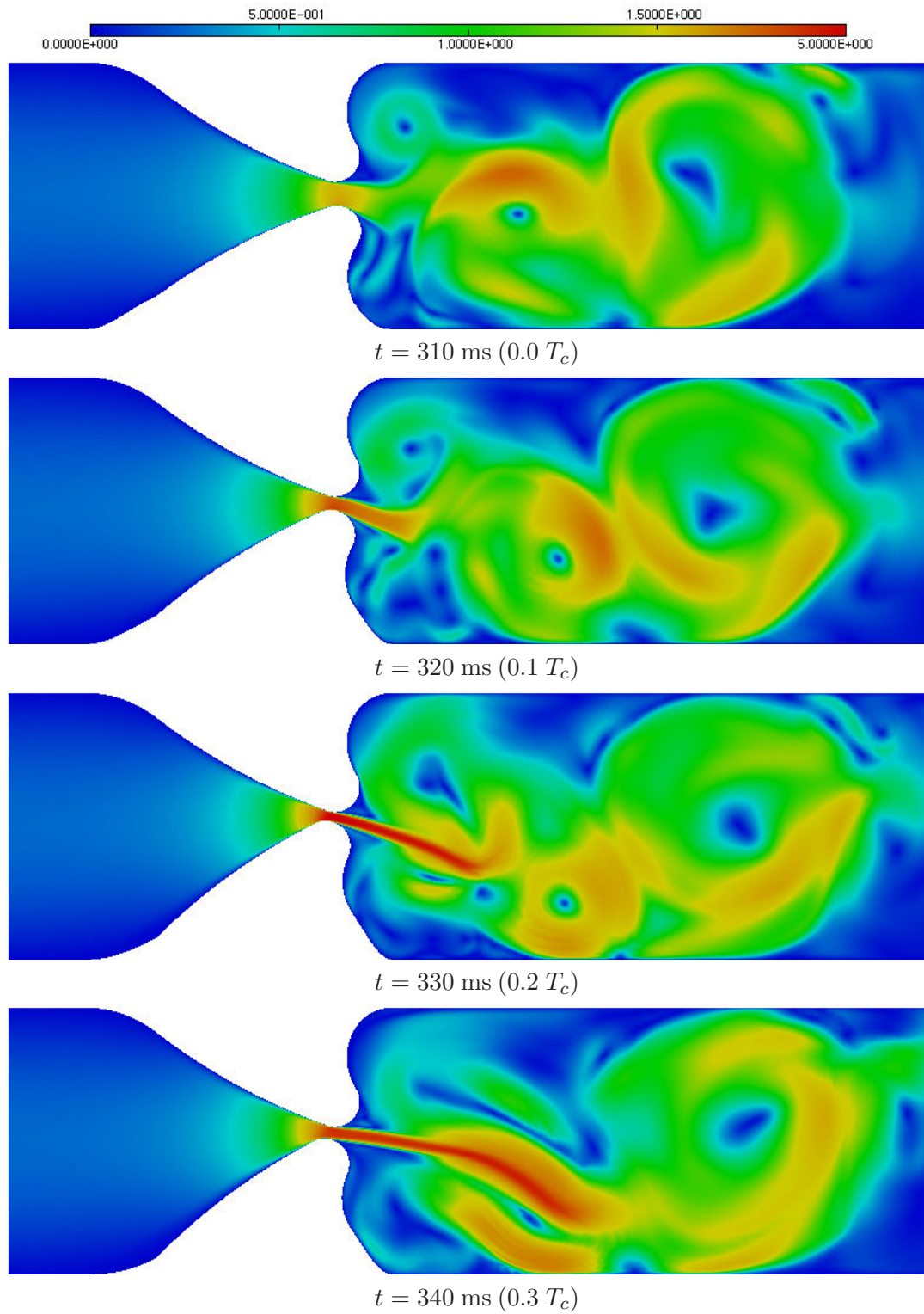


Figure 2.7: Development of the velocity field during the vocal fold vibration cycle – velocity magnitude [m/s].

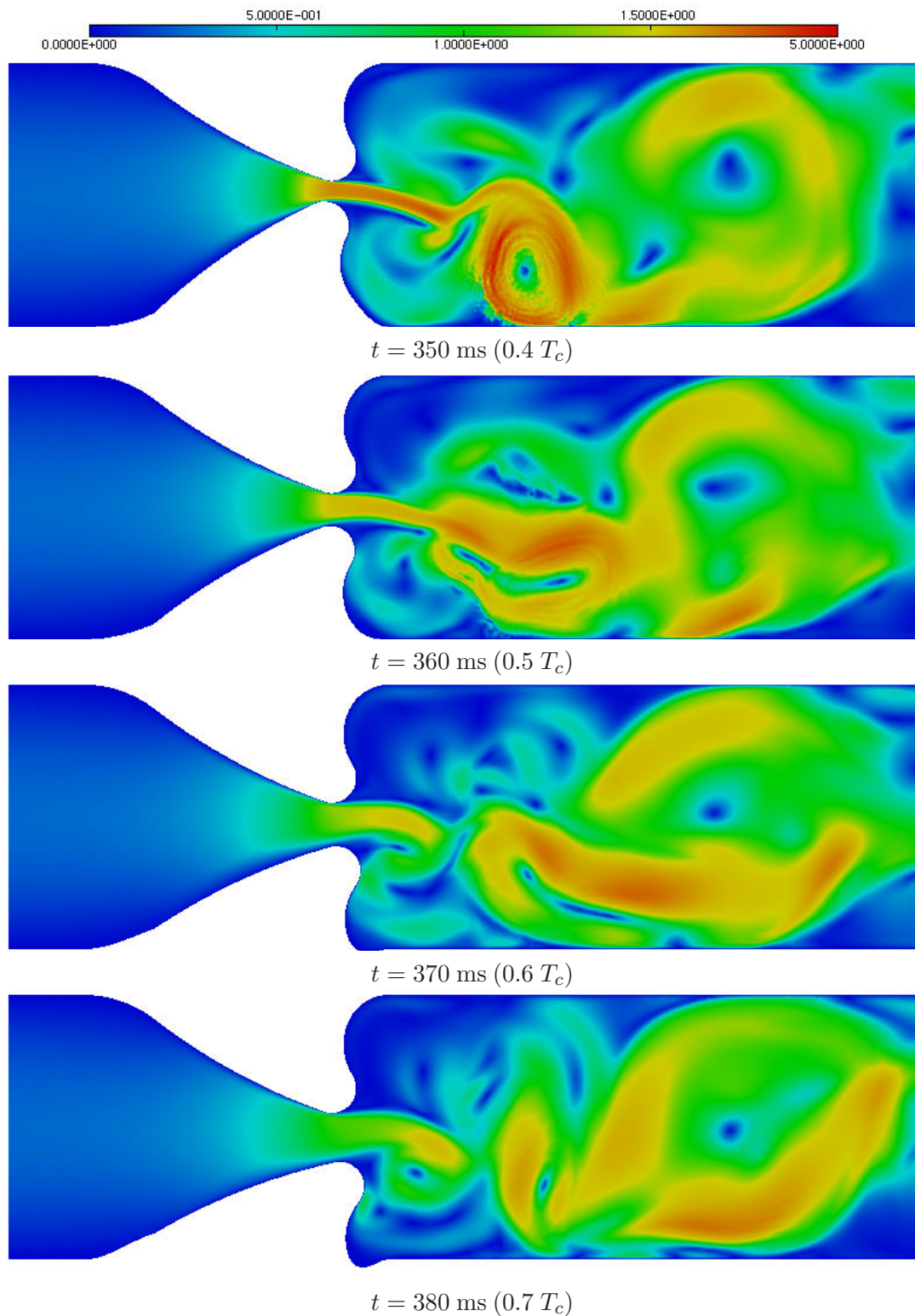


Figure 2.7: (continued) Development of the velocity field during the vocal fold vibration cycle – velocity magnitude [m/s].

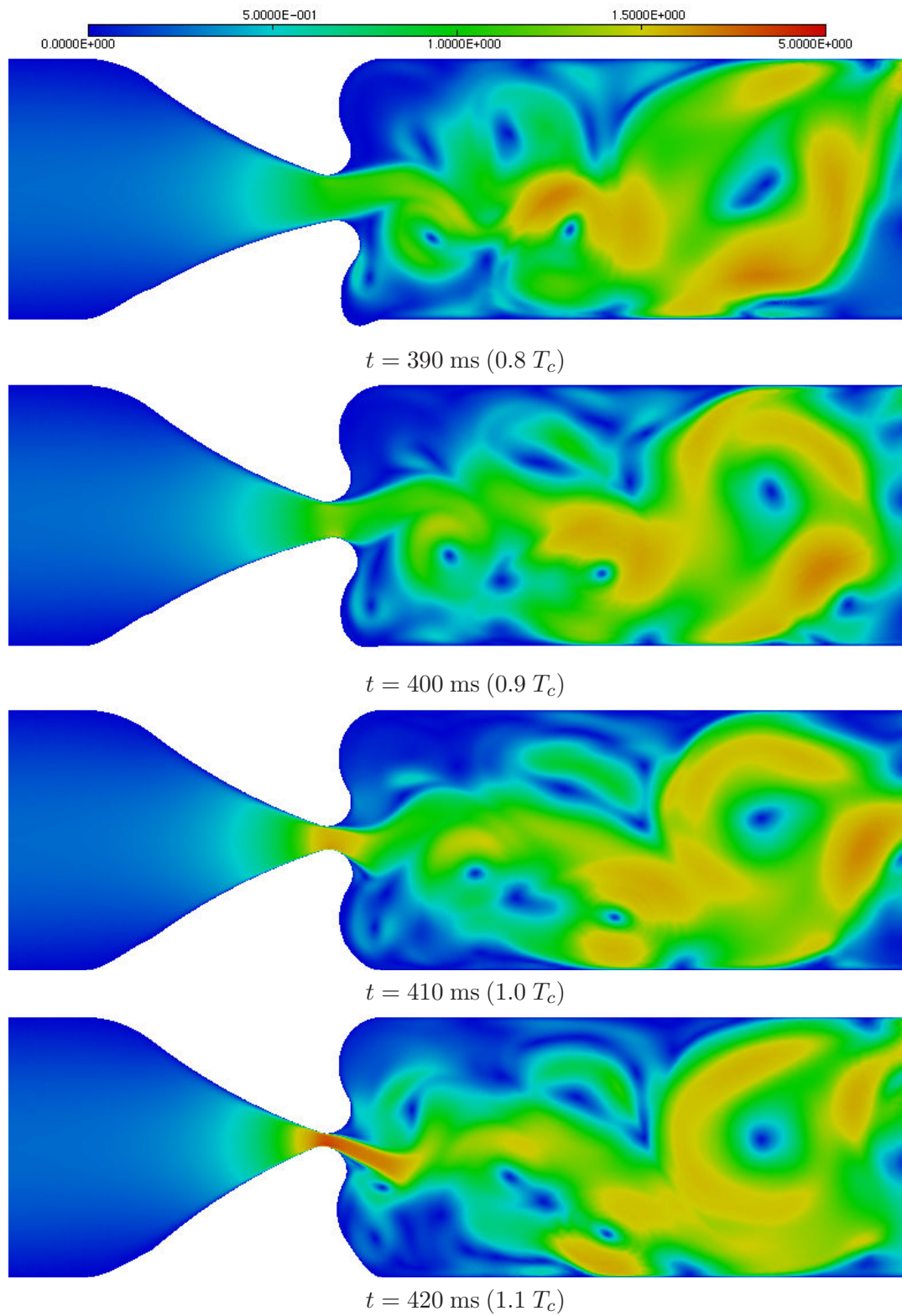


Figure 2.7: (continued) Development of the velocity field during the vocal fold vibration cycle – velocity magnitude [m/s].

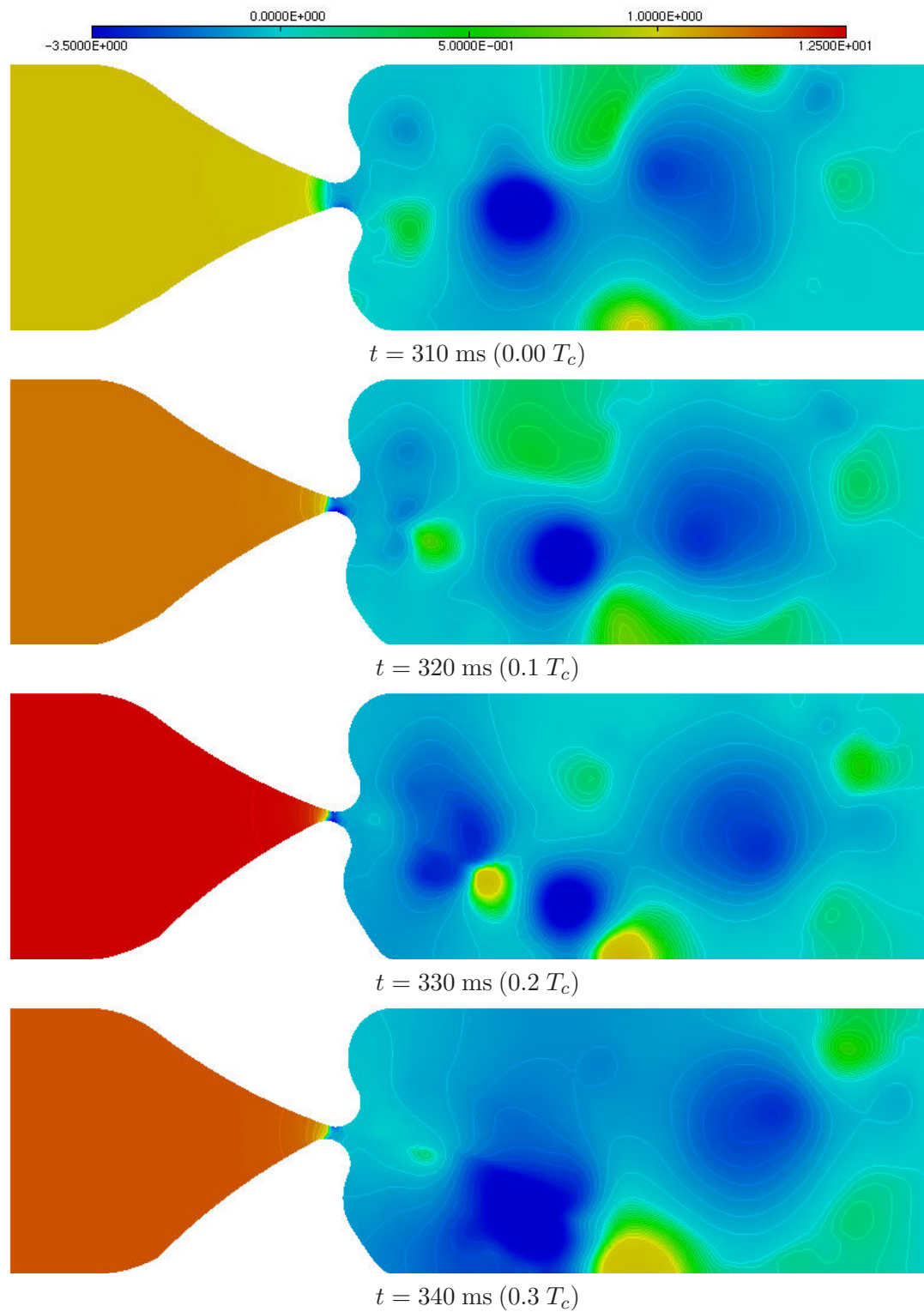


Figure 2.8: Development of the pressure field during the vocal fold vibration cycle – pressure [Pa].

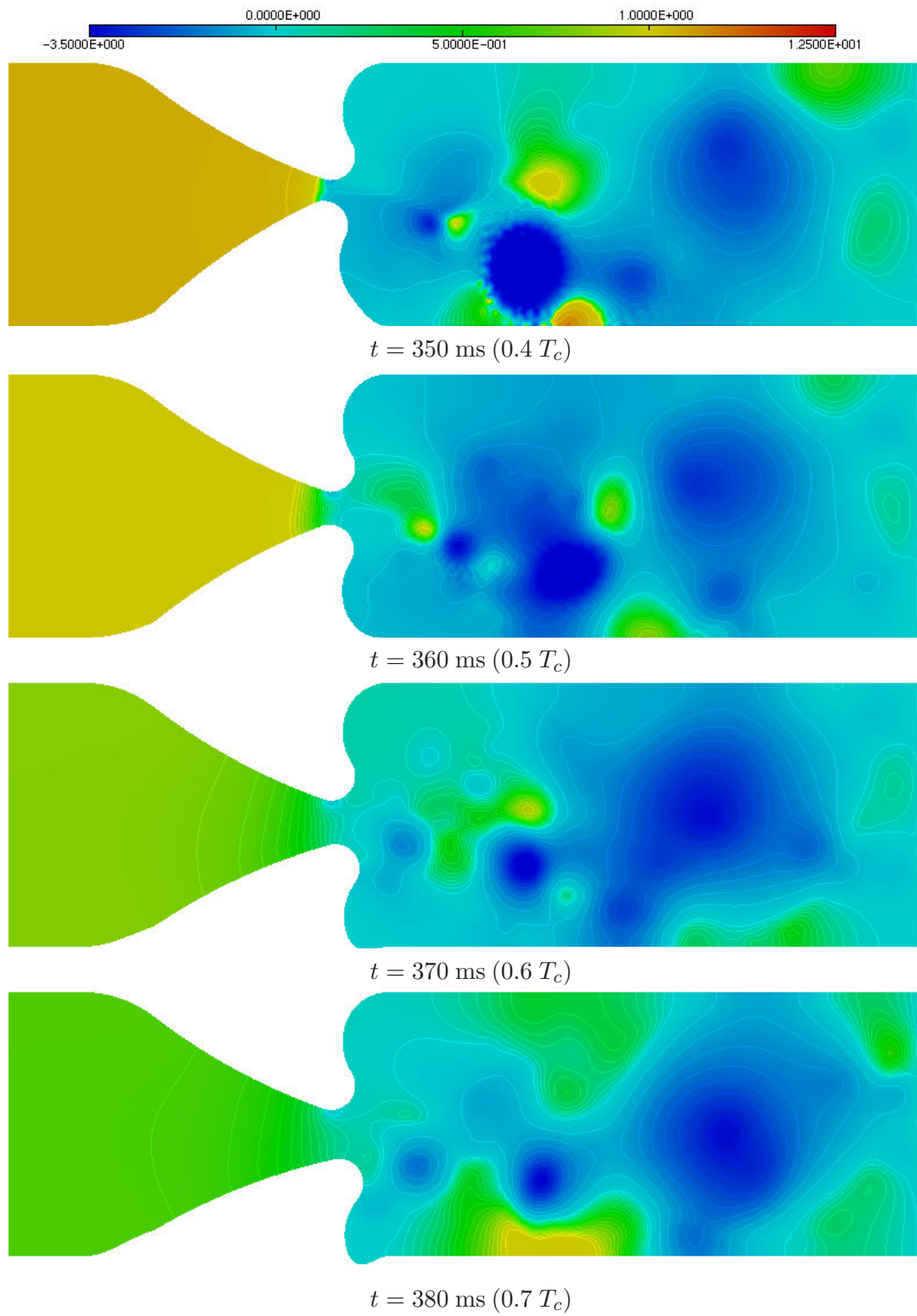


Figure 2.8: (continued) Development of the pressure field during the vocal fold vibration cycle – pressure [Pa].

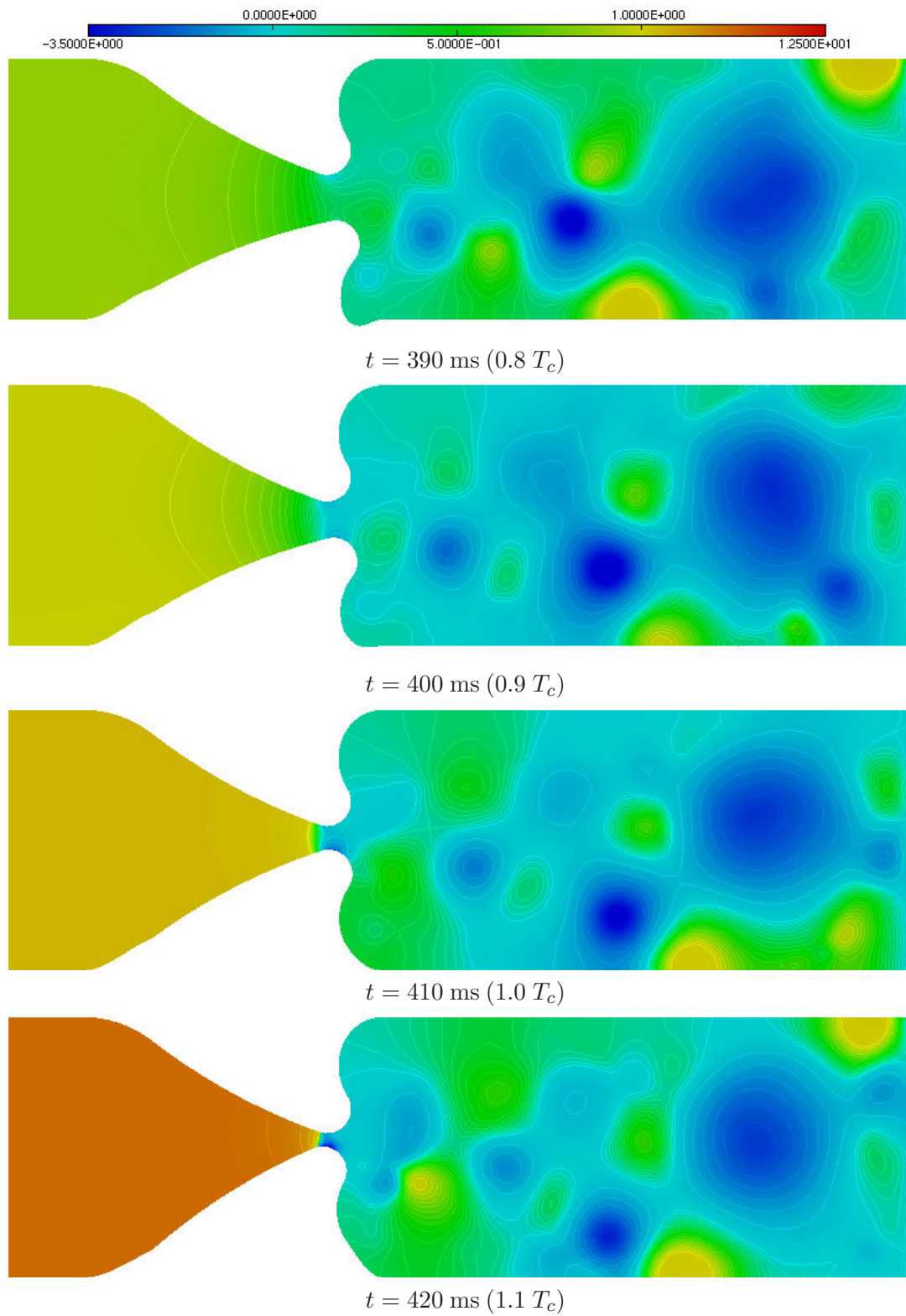


Figure 2.8: (continued) Development of the pressure field during the vocal fold vibration cycle – pressure [Pa].

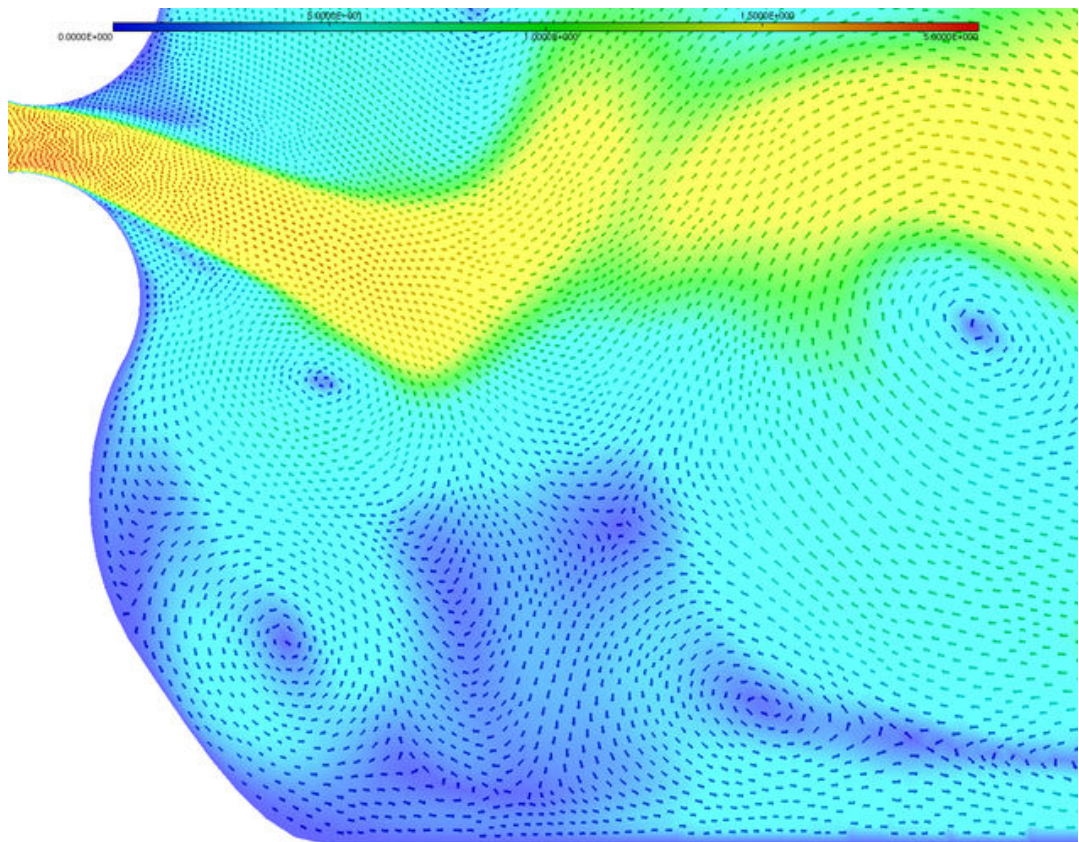


Figure 2.9: Detail of the velocity field near the jet front, $t=420$ ms. Velocity magnitude in color, vectors indicate the flow direction.

Chapter 3

Experimental investigation

Despite the numbers of sophisticated mathematical models of vocal fold vibration and glottal flow developed in recent years, experimental approaches still play an important role in vocal fold research. The computational models can supply very useful data; nevertheless, it is necessary to keep in mind that many models are based on important simplifications and that the results cannot be extrapolated beyond the parameter limits, for which they were designed. The models often cannot avoid to include several ad hoc assumptions. Moreover, in vocal fold modeling one needs to enter many geometrical and tissue parameters, whose numerical values are often not well known. Therefore, the results from the mathematical models should always be verified using experimental data.

The most relevant data regarding vocal fold vibration originate from measurements on living human subjects. However, since the human vocal folds are hardly accessible, the majority of processes occurring during phonation cannot be measured directly *in vivo*. The second possibility is to perform *in vitro* investigations, i.e. measurements on excised human or animal larynges. This approach provides improved accessibility to measured structures and tissues in better controlled laboratory conditions; yet many drawbacks of experiments on living tissues persist – technical complications, poor measurement reproducibility and also ethical concerns. This is why it is often useful to employ physical vocal fold models with well-defined and easily controllable parameters. Provided that the mechanical model reflects the important characteristics of real vocal folds, these measurements may help in understanding some of the fundamental physical processes in voice production.

Investigation of the supraglottal flow velocity field represents one of the cases, where both *in vivo* and *in vitro* measurements are hardly realizable. Therefore a self-vibrating mechanical model of human vocal folds was designed and fabricated during the stay of the author at ENSTA Paris. The principal goal was to study the conditions, where flow-induced vibrations of vocal folds occur and to investigate the velocity fields in the supraglottal channel immediately upstream the narrowest glottal gap. The measurements of the flow velocity fields were done by means of Particle Image Velocimetry, during different phases of vocal fold motion. The measured data were intended to be compared with the results from the FEM computational model.

3.1 Principles of Particle Image Velocimetry

Many areas of technical research and development require a measuring technique that can measure the flow velocity across a larger domain of the flow field. This can be achieved by scanning the domain with a point velocity probe (such as a Pitot tube or a hot-wire probe), however the instantaneous flow structure is lost and such procedure can be very time-consuming. Besides the qualitative and semiquantitative flow visualization methods (direct injection, optical and holographic interferometry), an optical non-intrusive quantitative technique has developed during last 30 years; this method is called Particle Image Velocimetry (PIV). PIV can measure the velocity field across a selected planar domain of the flow, providing the instantaneous velocity vectors.

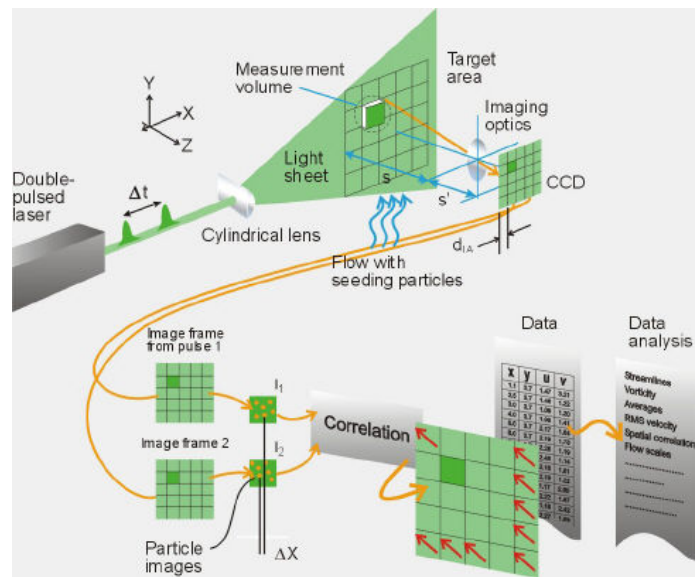


Figure 3.1: Principle of the PIV method (adapted from [6]). The position of the seeding particles, illuminated by a double-pulsed laser light sheet, is recorded into two frames. Cross-correlation of two corresponding interrogation windows I_1 and I_2 yields the flow velocity vector.

The basic principles of the method are demonstrated in Fig. 3.1. The flow is seeded with small particles, typically oil aerosols in gases and solid particles in fluids. Using a light sheet, formed by passing a double-pulsed laser beam through a cylindrical lens, the position of these particles is illuminated twice with a small time delay in between. A fast computer-shuttered CCD camera synchronized with the laser system records two frames.

These two images are then divided into small subsections called interrogation windows. The pixel by pixel cross-correlation

$$C(S) = \iint_{IW} I_1(X) \cdot I_2(X - S) dX \quad (3.1)$$

of the image signals $I_1(X)$ and $I_2(X)$ corresponding to the same interrogation window IW gives a correlation peak, which identifies the particle displacement vector. Assuming that the tracers follow the flow, the flow velocity vector is then calculated from the known time delay of the laser pulses.

The velocity vectors obtained from a standard PIV, using one camera with optical axis perpendicular to the light sheet, are only two-dimensional. This setup is suitable for the flow that can be assumed 2D (e.g. flow past airfoils, cylinder wakes). If the third velocity component is needed too, two CCD cameras in stereoscopic arrangement can be used.

3.2 Concept and design of the physical vocal fold model

The flow in human vocal folds can be in first approximation considered as two-dimensional – one may suppose that the flow velocity does not change significantly along the width of the vocal folds (i.e. along the anterior-posterior axis z , see Fig. 3.2). This encourages the development of 2D or quasi-1D mathematical flow models, and also permits to draw meaningful data from PIV measurements of the physical vocal fold models.

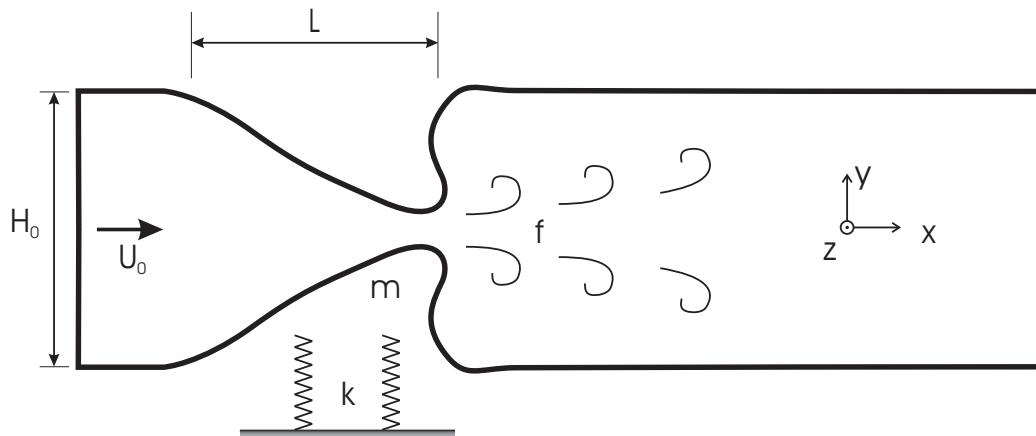


Figure 3.2: Basic design of the vocal fold model and overview of the important dimensional parameters: channel height H_0 , inlet flow velocity U_0 , characteristic length L and frequency f , mass m and stiffness k .

To reflect these facts, the physical model was proposed as a vocal-fold-shaped element vibrating in the rectangular channel wall, preferably in the x - y plane. The z -dimension (i.e. the width) of the vocal fold was intended to exceed considerably its length and depth, which is the case in true vocal folds, too¹. The shape of the vocal folds was specified according to measurements of excised human larynges, performed in the Institute of Thermomechanics [34]. The next issue to be determined was the overall dimension of the physical model.

There is no doubt that when trying to experimentally investigate complex real processes in laboratory conditions, the ideal setup is a physical model in true, i.e. 1:1 scale. However, from various reasons the development of a true scale model is often inconvenient or even impossible. In these cases one may try to use a scaled model, while conserving important dimensionless numbers relevant to the process involved. With the aid of dimensional analysis it is afterwards possible to relate the measured results to real, non-scaled conditions.

¹The terms 'length', 'width' and 'depth' are defined here in a natural way, to be consistent with the length, width and height of the wind tunnel. In vocal fold modeling, however, the vocal fold dimensions are standardly defined in a different way: length along the z -axis, thickness (width) in x -direction and depth along the y -axis.

The physical dimensions of real human vocal folds – width about 16 mm [46], length 9 mm and depth 5 mm – are rather small; this would make the construction of a mechanical vocal fold model in 1:1 scale and installation of the measuring devices very difficult. Further, the double-flash PIV laser system available had a maximum repetition frequency of 20 Hz, and due to synchronization it was preferable to design a system with the natural frequencies $f \leq 20$ Hz, too. This implies the necessity to increase the mass/stiffness ratio, i.e. again to increase the model dimensions. Moreover, the PIV camera was to acquire the images through a plexiglass channel wall; in these conditions and with the seeding particles used a larger image size results in much better image quality and resolution. Taking all this into account, it was necessary to design a model 2 – 5 times enlarged with respect to real vocal folds.

The most relevant dimensionless numbers pertinent to nonstationary flow past vibrating vocal folds are arguably the Reynold's number

$$Re = \frac{U_0 H_0}{\nu} \quad (3.2)$$

and the Strouhal number

$$St = \frac{fL}{U_0}, \quad (3.3)$$

which can be based on the channel height H_0 and mean flow velocity at inlet U_0 , kinematic air viscosity $\nu = 1.58 \cdot 10^{-5} \text{ m}^2 \text{ s}^{-1}$, frequency of vortex shedding f (supposed to be equal to the frequency of vibration of vocal folds), and vocal fold length L (see Fig. 3.2).

The Reynolds number Re represents the ratio between the convective and diffusive effects (i.e. the inertial and viscous forces) in the flow and determines in a crucial way the nature of the flow - development of the boundary layer, flow separation, vortex dynamics and turbulent effects in general. The Strouhal number, alias "reduced frequency", indicates the relationship between the characteristic time of convection L/U_0 and the frequency of flow fluctuations, which are in this case strongly coupled with the natural frequency of the mechanical system. In flow past stationary, non-vibrating bluff bodies, the Strouhal number is known to reach the values of approximately 0.2 (for the case of cylinders) [3]. For elastic structures capable to exhibit vibration, the issue is whether the vibration frequency of the structure gets close to the frequency of stationary vortex shedding. If so, the shedding frequency may "lock" to the vibration frequency, which has a strong effect on organizing the wake and amplifying the vibration amplitude. The Strouhal number of about 0.24, encountered in the physical model which was finally fabricated, could suggest that the conditions were favorable for this lock-in effect.

The natural frequencies of the first two modes of the mechanical model (lift and rotation in x - y plane, see Fig. 3.2) are determined by the ratio

$$f \propto \sqrt{\frac{m}{k_b}}, \quad (3.4)$$

where m is the mass and k_b the stiffness of the supporting springs. To ensure that these modal frequencies are lower than 20 Hz, considerably low stiffness in vertical direction is needed. For the proper function of the model, however, the torsional stiffness k_t should remain as high as possible (the term torsion is used here for the rotation with respect to the x-axis). Consequently, the springs were designed as four slender cantilever beams of length l_s , width w_s and thickness t_s . The bending and torsional stiffness of one beam, denoted k_b^1 and k_t^1 , respectively, can be calculated from the formulas

$$k_b^1 = \frac{E w_s t_s^3}{12 l_s^3 (1 - \mu^2)}, \quad k_t^1 = \frac{G t_s w_s^3}{3 l_s}. \quad (3.5)$$

One can note that rather than by the material properties – Young modulus E , shear modulus G and Poisson's ratio μ – the stiffnesses are influenced by the beam thickness and length (in flexion) and width (in torsion), which figure in third powers. Using the equations (3.4), (3.5), the requirements $f \leq 20$ Hz, $k_t \gg k_b$ and taking into account the technical constraints, the required spring dimensions were estimated as $l_s \approx 80$ mm, $w_s \approx 10$ mm, $t_s \approx 0.5$ mm. The cantilever beams, representing the springs, were fabricated from a brass alloy (which has lower elastic moduli than steel) and fixed with screws and shims. The physical model of the vocal folds, mounted in the measuring section of the wind tunnel, is shown in Fig. 3.3, additional images can be found on the accompanying DVD.

The vocal folds themselves were cast using a RTV-II two-compound silicone rubber type 69199. In the configuration presented here, the upper vocal fold was fixed to the channel wall. The second one, attached to a lightened square aluminum profile, was mounted on four brass flat springs into the wall of the channel. Two adjusting screws allowed to set the zero position of the vocal fold precisely.

Unfortunately, the mechanical system did not provide enough free parameters to preserve the Reynolds and Strouhal numbers (3.2), (3.3) exactly. Also due to dimensions of the wind tunnel available, a 1:4 scale was finally chosen for the physical model, which gives

$$\frac{H_0^{PM}}{H_0^{VF}} = \frac{L^{PM}}{L^{VF}} = 4 \quad (3.6)$$

(see Fig. 3.2, superscripts PM and VF denote the physical model and the real vocal fold, respectively). As described above, the natural frequencies of the system, supposed to be equal to the frequency of flow fluctuations (vortex shedding) cannot be chosen arbitrarily, neither; taking a typical fundamental frequency of male voice of $f^{VF} \approx 100$ Hz and the first natural frequency of the physical model of $f^{PM} \approx 13$ Hz yields the ratio

$$\frac{f^{PM}}{f^{VF}} \approx \frac{1}{8}. \quad (3.7)$$

In a system, whose vibrations are self-induced, the flow velocity U_0 is not a completely free parameter. Unlike externally excited vocal fold models (e.g. the hydrodynamical model of Kob et al.

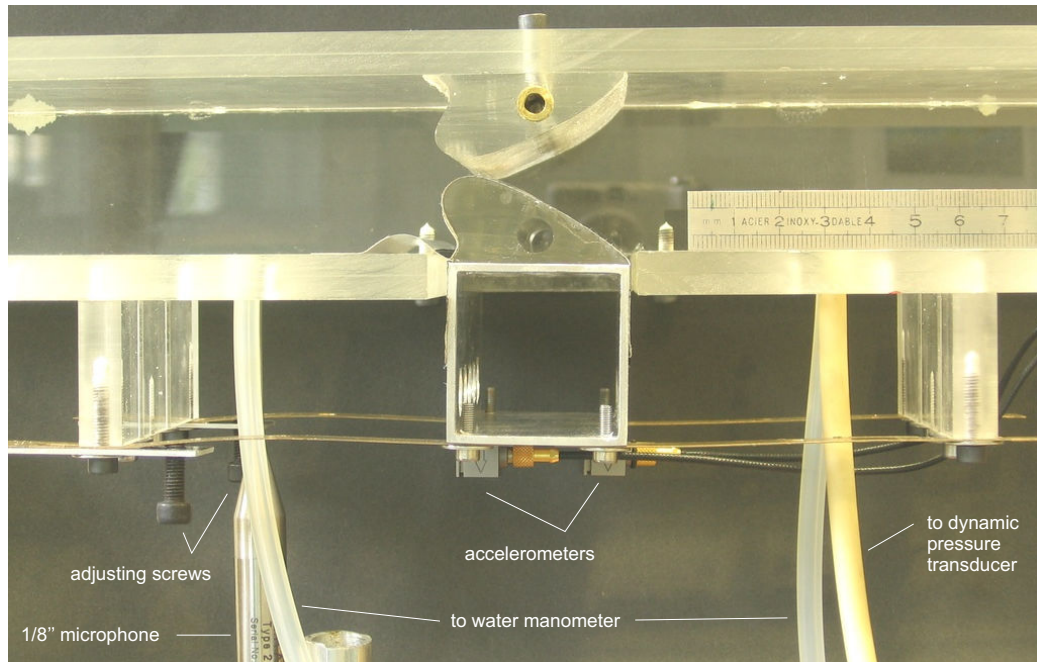


Figure 3.3: Design of the physical model of vocal folds (in configuration fixed upper - vibrating lower vocal fold). The vibrating elastic silicone rubber element is attached to an aluminum profile, supported by four adjustable brass flat springs. The system is equipped with two Brüel&Kjær 4507C accelerometers, a G.R.A.S. 1/8" measuring microphone type 2692, two hoses connected to a water manometer and inlet of the Validyne DP15TL pressure transducer. Available on the DVD in full resolution.

[22]), the flow rate must remain between the bounds given by the critical flow (the lowest flow able to excite vibrations) and the maximum flow (at which the vibrations either stop or become chaotic). Using a 1D mathematical model of Horáček & Šidlof [17, 30] some estimations have been performed prior to physical model fabrication to ensure that the Reynolds and Strouhal numbers stay approximately the same for the physical model as for the real vocal folds. The flow-induced vibrations of the vocal fold model, which was eventually fabricated, occurred for flow velocities ranging from $U_0^{PM} = 1.25 - 5$ m/s. Considering a typical mean subglottal flow velocity during phonation of $U_0^{VF} \approx 2.5$ m/s and using (3.6), (3.7), one may estimate that for the physical model, the Reynolds number $Re = 2000 - 3000$ was 2–6 times higher and the Strouhal number $St \approx 0.24$ was 1–3 times lower than those of real vocal folds. Hence, the physical model cannot be claimed to be perfectly dynamically similar; however, it can be assumed that the flow regime is not substantially different from the real situation.

3.3 Experimental setup

The vocal fold model was mounted into a plexiglass wind tunnel comprising a blower engine and a long circular channel with a diameter of 180 mm intended to suppress the inlet turbulence. Further, the channel cross-section contracts smoothly by factor $f \approx 6$ into a rectangular 100×40 mm inlet of the measuring section with the vocal folds, continues approximately 40 cm to simulate the vocal tract and terminates freely into ambient air. The overall view of the experimental setup is shown in Fig. 3.4.

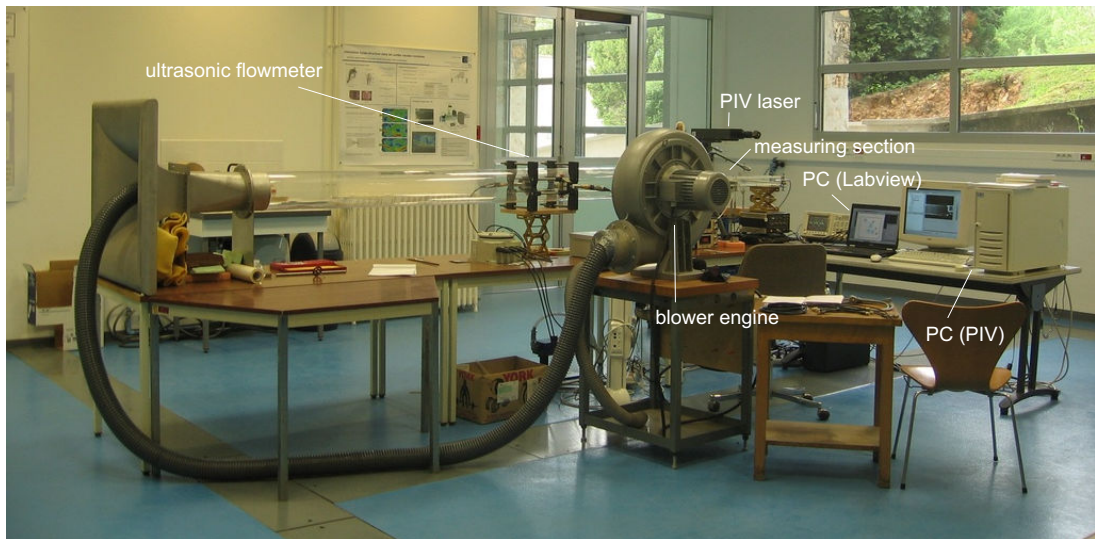


Figure 3.4: Overall view of the experimental setup. Available on the DVD in full resolution.

In addition to the PIV system installed to measure the supraglottal flow field, the model was also equipped with accelerometers, pressure transducers and microphones to measure and record vocal fold vibration. The diagram in Fig. 3.5 shows the locations and wiring of transducers used, the dimensions are specified in Fig. 3.6.

To measure the mean flow in the channel, an ultrasonic flowmeter was mounted near the downstream end of the circular channel. Unlike many other flow velocity measuring techniques, this device represents a non-invasive way to measure the stationary flux through the channel. It provides a digital value in liters per minute (LPM) and a calibrated analogue output signal. The measured values are, however, not very precise and even in the case of stationary flow the output often fluctuates up to ten percents. Moreover, the device performs one readout per two seconds and thus is completely unsuitable for dynamic flow measurements.

Two accelerometers, fixed under the vibrating vocal fold, were used to record mechanical vibration. The 1:4 scale of the model allowed to use the relatively large, but very sensitive type B&K 4507C without affecting the system significantly. The conditioning amplifier with built-in signal integration, supplied with the accelerometers, can in addition to acceleration provide also velocity or even displacement waveforms. Such signal integration may however introduce phase distortions, and since the phase was an important issue, no integration was selected.

The signal from the accelerometer was also used to trigger the PIV laser. Rectification using a pulse generator yields a rectangular signal, whose rising edge corresponds to a distinct phase of vocal fold

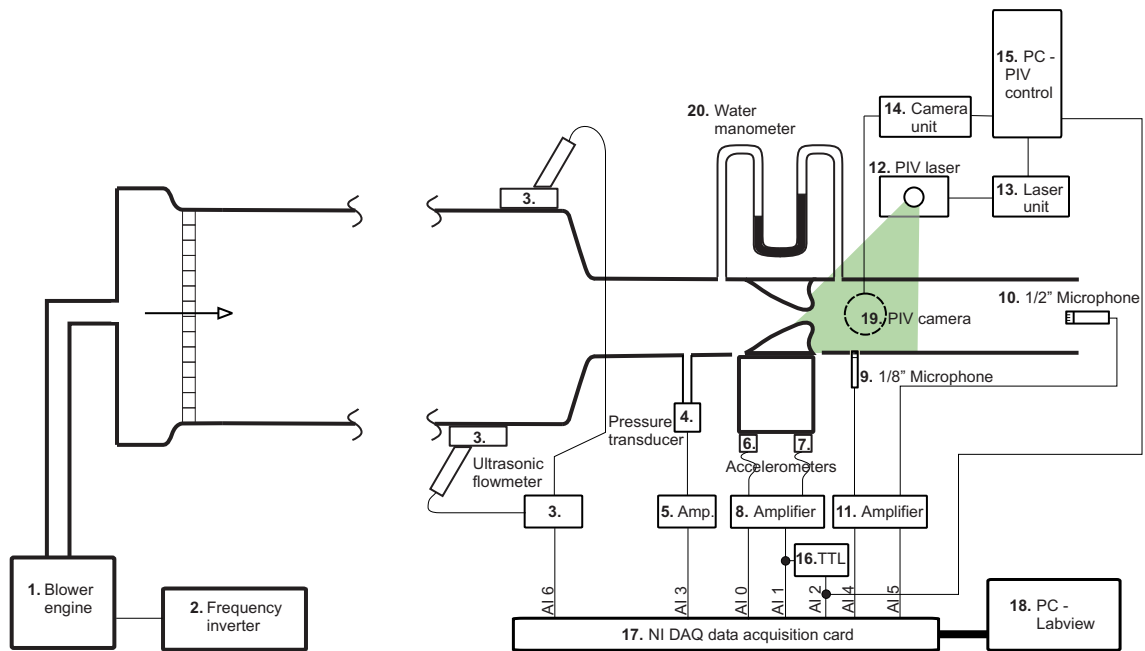


Figure 3.5: Diagram of the experimental setup used for the measurements of vocal fold vibration and for PIV investigation of the supraglottal flow.

1. Rietschle Thomas centrifugal blower engine (2200 W, $\Delta p_{max} = 29$ mbar, $Q_{max} = 2770$ m³/h). 2. Omron Sysdrive 3G3MV frequency inverter (380 V, 0 – 60 Hz). 3. GE Panametric GC 868 ultrasonic gas flowmeter. 4. Validyne DP15TL dynamic pressure transducer (steel membrane 0.125 PSI FS). 5. Validyne CD23 amplifier. 6., 7. Brüel&Kjær 4507C accelerometers. 8. Brüel&Kjær Nexus conditioning amplifier type 2692 (frequency bandpass 1 Hz – 1 kHz). 9. G.R.A.S. 1/8" condenser microphone type 4138, G.R.A.S. preamplifier type 26AJ. 10. G.R.A.S. 1/2" prepolarized free field microphone type 40BE, G.R.A.S. preamplifier type 26AJ. 11. Brüel&Kjær Nexus conditioning amplifier type 2690. 12. New Wave Research PIV laser SOLO 3-15. 13. New Wave Research SOLO III laser unit. 14. LaVision Imager PRO camera unit. 15. PC - 2proc Intel Xeon, software Davis v7. 16. Philips PM5715 TTL/pulse generator. 17. National Instruments NI DAQPad-6015 data acquisition card. 18. PC - software NI LabView v7.1. 19. LaVision Imager PRO camera (1600x1200 pixel, Nikon AF NIKKOR 50 mm 1:1.8 D lens, f-number 8). 20. Kimo water manometer (precision 0.5 mm H₂O (5 Pa)).

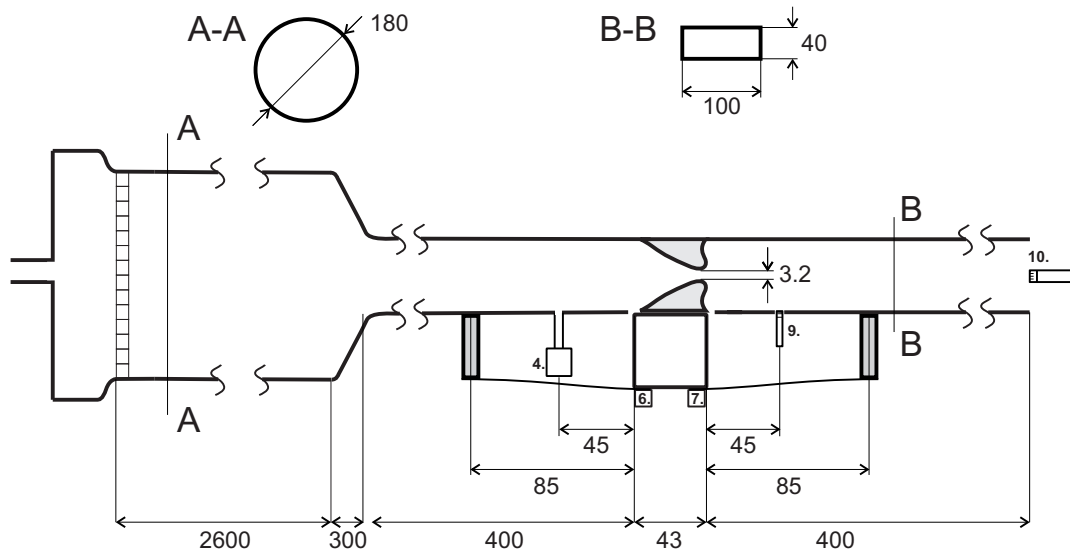


Figure 3.6: Dimensions of the wind tunnel and placement of the transducers

motion. Using the phase shift function of the generator (or of the PIV controlling software) allows to trigger the PIV at arbitrarily chosen vocal fold position, i.e. at a distinct glottal opening and jet formation phase.

In voice production, the pressure waveforms are obviously of high importance and interest. The pressure waves emitted to the ambient atmosphere represent the generated voice, while the supraglottal pressure waveform provides information on the acoustic signal generated by the vocal fold itself (one must take into account the vocal tract resonances). From the subglottal pressure one may calculate the mean transglottal pressure, an important parameter for voice onset, and also observe the subglottal vocal tract resonances. This is why three measurement spots were chosen: at the exit of the channel, and immediately downstream and upstream the glottis (see Fig. 3.5).

Due to the first natural frequency of the mechanical system $f \approx 13$ Hz, the fundamental acoustic frequency was out of the documented range of standard measuring microphones. Hence, dynamic pressure transducers were tried first. However, the transducers available (Validyne DPTL-family with changeable measuring membrane), in combination with the recommended amplifiers, gave poor signal-to-noise ratio and zero-level stability, and introduced spurious resonance frequencies. The measuring microphones, on the other hand, proved surprisingly good frequency response even in this infrasonic band, and provided much better signal. Finally, only one pressure transducer was used to record the subglottal pressure where non-zero DC component is present (this static value actually corresponds to the mean transglottal pressure, which could be also read out from the water manometer).

The amplifiers and the LabView measuring software were set up so that all the registered data were directly in SI units. In the case of the accelerometers and measuring microphones, manufacturer-specified calibration data were used. The pressure transducers were calibrated by the use of a water manometer. The calibration data are available on the DVD.

The spatial configuration of the PIV system is demonstrated in Fig. 3.7. This setup, with vertical laser sheet passing through the middle of the channel and a camera with horizontally situated optical

axis, allows to record the 2D flow field across the plexiglass channel wall. Due to oil particle deposition on the walls, frequent cleaning was necessary during measurements to preserve sufficient image sharpness.

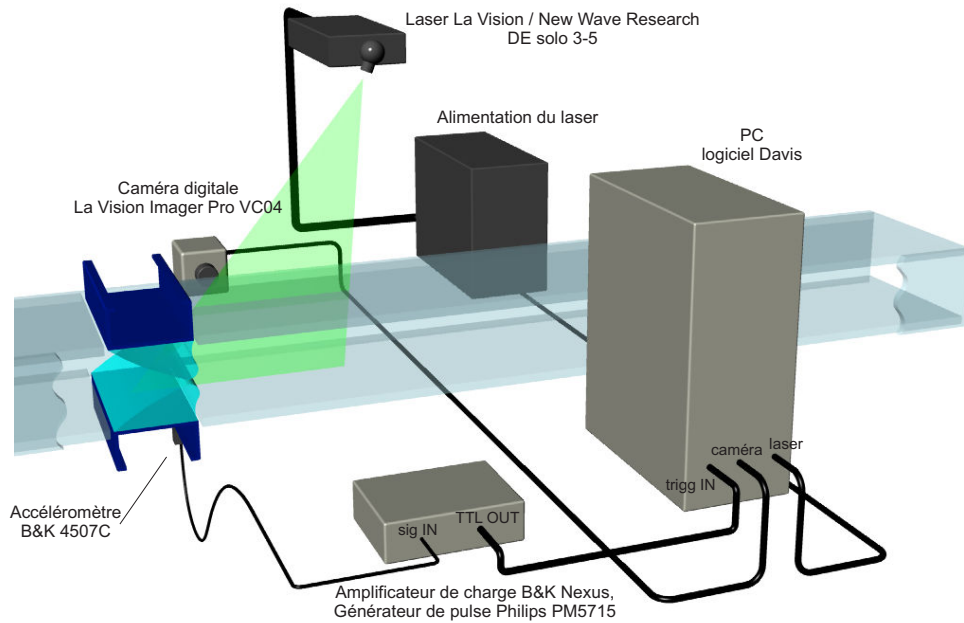


Figure 3.7: 3D diagram of the PIV setup. The signal from the accelerometer, rectified by a TTL/pulse generator, is used to trigger the PIV laser and the camera shutter. The laser sheet passes vertically through the middle of the channel so that the domain immediately downstream the glottis is illuminated.

3.4 Results of the dynamic and acoustic measurements

The primary purpose of the vibroacoustic measurements was to acquire supplementary data to the PIV records. Basically, the procedure consisted of setting the flow rate, taking one ten-second record of the accelerometer, pressure and acoustic signals (with a sampling rate of 2 kHz), and performing a series of PIV measurements for approximately 25 phases of the vocal fold motion (the latter will be explained in detail in section 3.5). This procedure was repeated for the flow rate values ranging from minimum flow able to sustain vocal fold vibration up to a maximum value, where either the vibrations ceased or became chaotic or irregular. The systematic interpretation of the vibroacoustic data, even regardless of the PIV measurements, provides valuable information on the dynamical behavior of the system.

First of all, the natural vibration of the model without flow was measured. The silicone profile was deflected from equilibrium, released and left to exhibit damped oscillation. The waveform and spectra of the acceleration in Fig. 3.8 reveal a dominant spectral frequency of 11.0 Hz, corresponding to the natural frequency of the prevailing translational mode.

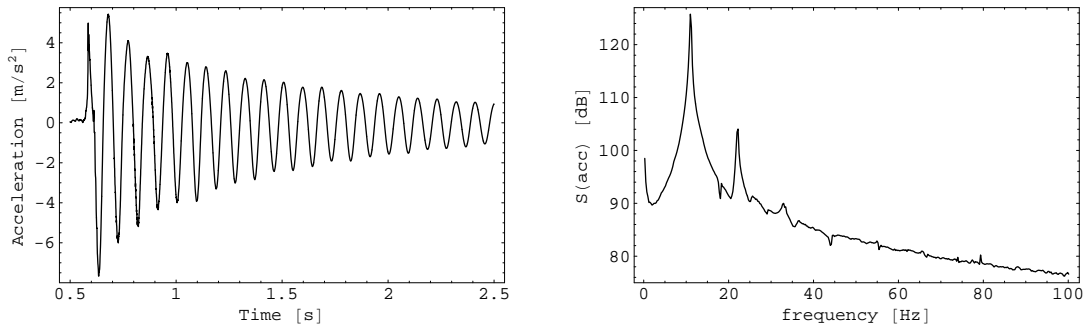


Figure 3.8: Waveform and spectra of the damped natural vibration of the physical model. The first peak in the spectrum at 11.0 Hz corresponds to the natural frequency of the translational mode. The second peak at 21.9 Hz is most likely the natural frequency of the torsional mode (which was undesirable).

Fig. 3.9 shows dependence of the frequency of vibration on the flow rate. It demonstrates a behavior typical for nonlinear dynamic systems, where a small change of the driving parameter (the flow rate in this case) may cause a substantial alteration of some vibrational characteristic, i.e. invoke a turnover of the mode of vibration. Tracking the frequency with increasing flow rate allows to distinguish four modes of vibration: mode I, where small flow rates induce impactless low-amplitude vibration, whose frequency does not change significantly. At critical flow $Q_{crit} = 7.6$ l/s, this regime suddenly turns into mode II and further mode III, which are characterized by large-amplitude regular vibrations with impacts in each cycle. Subjectively, these modes represent the ideal energy transfer from the flow to the mechanical vibrations, and correspond best with normal voice production. The nature of vibration in modes II and III does not differ noticeably; they were distinguished only on the basis of the frequency jump evident in Fig. 3.9. The acoustic pressures emitted in mode II/III vibration significantly exceed those measured in mode I. Finally, high flow rates induce partially irregular or even chaotic mode IV vibration with high noise level in the acoustic output.

The transition between mode III and mode IV showed evident hysteresis - the jump occurred at 13.6 l/s when increasing flow rate, while at 11.3 l/s when decreasing. The hysteresis of the mode

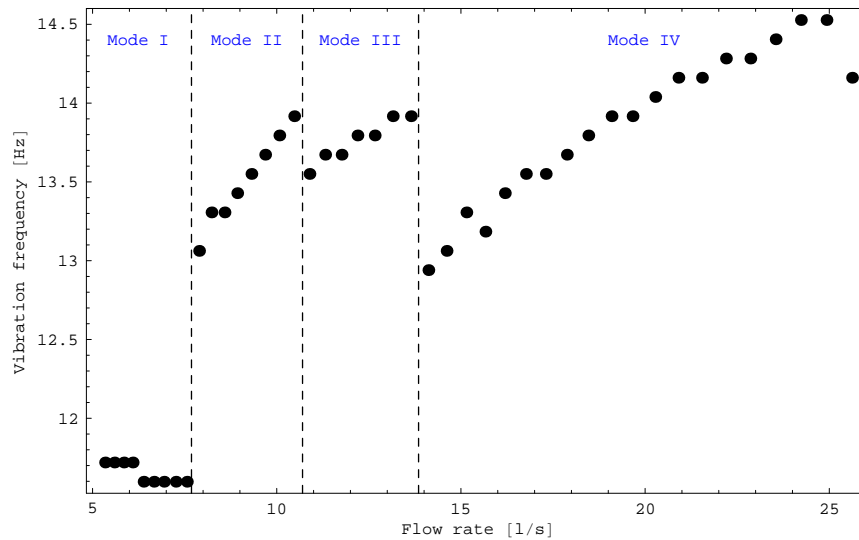


Figure 3.9: Frequency of vocal fold vibration as a function of increasing flow rate. Mode I: low flow rate, impactless vibration with low amplitude, frequency does not change significantly. Mode II,III (medium flow rate): at critical flow $Q_{crit} = 7.6$ l/s, regular vibrations with large amplitudes and impacts begin to develop. The frequency of vibration steadily increases with the flow, despite a sudden drop at $Q = 10.7$ l/s. Mode IV (high flow rate): at $Q = 13.8$ l/s, the character of vibration changes completely – partially irregular, low-amplitude vibrations arise. The data were drawn from Fourier analysis with a spectral resolution of $\Delta f = 0.12$ Hz.

transition I-II was much less distinct. Since the difference between modes II and III was hardly noticeable, the hysteresis was not measured.

The next important vibrational parameter is the maximum positive and negative acceleration over the oscillation cycle, i.e. the peak values on the acceleration waveforms. These values provide important information about the amplitude and intensity of vibration, and are of particular interest for voice specialists, since the maximum acceleration and impact intensity are often considered as the principal factors causing certain traumatic vocal fold changes, such as vocal fold nodules.

The dependence of the maximum acceleration on the flow rate is demonstrated in Figs. 3.10, 3.11 – to interpret the meaning it is necessary to realize that the positive peaks on the acceleration waveform correspond to the impact intensity (see also Figs. 3.13 – 3.15), while the negative peaks are related to the overall vibration amplitudes. In mode I vibration, the peak positive and peak negative accelerations are similar. In mode II and mode III, the positive, impact peaks are higher, while in mode IV, the acceleration is higher during the opening phase.

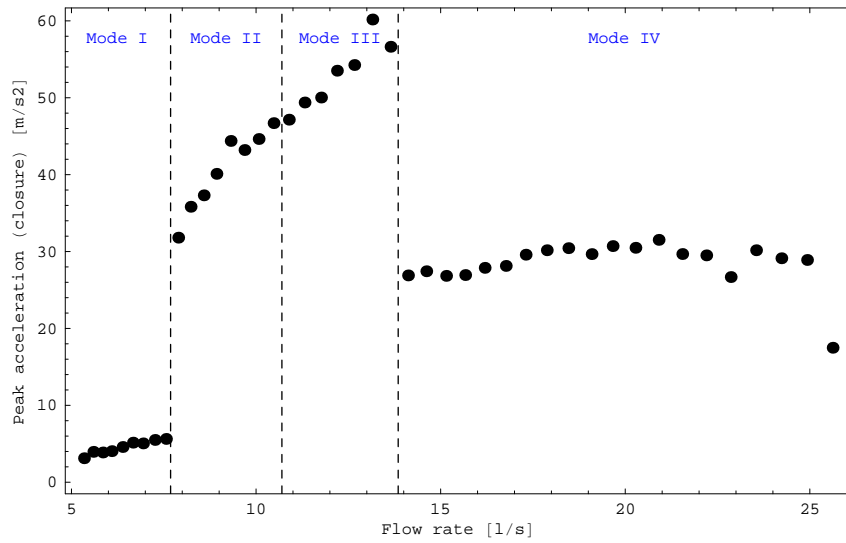


Figure 3.10: Maximum positive acceleration (impact intensity) versus flow rate. Mode I: low flow rate, impactless low-amplitude vibrations. Mode II,III: medium flow rate, regular vocal fold vibration with impacts whose intensity rises with increasing airflow. Mode IV: high flow rate, maximum acceleration does not change significantly.

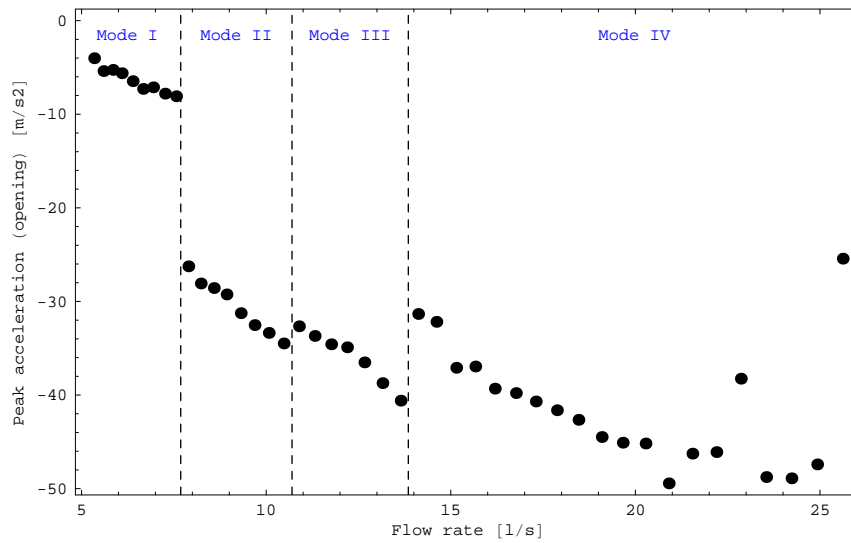


Figure 3.11: Maximum negative acceleration (peak acceleration during opening phase) versus flow rate. Mode I: low flow rate, impactless low-amplitude vibrations. Mode II,III: medium flow rate, regular vocal fold vibration with impacts. Mode IV: high flow rate, absolute value of the peak acceleration continues to increase slightly.

In the rest of this section, Figs. 3.12, 3.13, 3.14 and 3.15 show the measured waveforms and their spectra for four example flow rate values: low rate $Q = 5.59$ l/s (mode I), which induces impactless small-amplitude vibrations, medium flow rate $Q = 8.58$ l/s and $Q = 10.47$ l/s (mode II and III - regular vibrations with impacts) and high flow rate $Q = 17.87$ l/s (mode IV), where the vibrations become irregular and the acoustic signal very noisy due to high turbulence level in the flow. The complete set of measurements is available on the DVD.

The acceleration signals presented here come from the accelerometer (numbered 7 in Fig. 3.5) mounted below the downstream edge of the vibrating vocal fold. The subglottal pressure was measured by a dynamic pressure transducer, while two measuring microphones monitored the acoustic signals. See Figs. 3.5, 3.6 for details regarding the measurement setup and wiring.

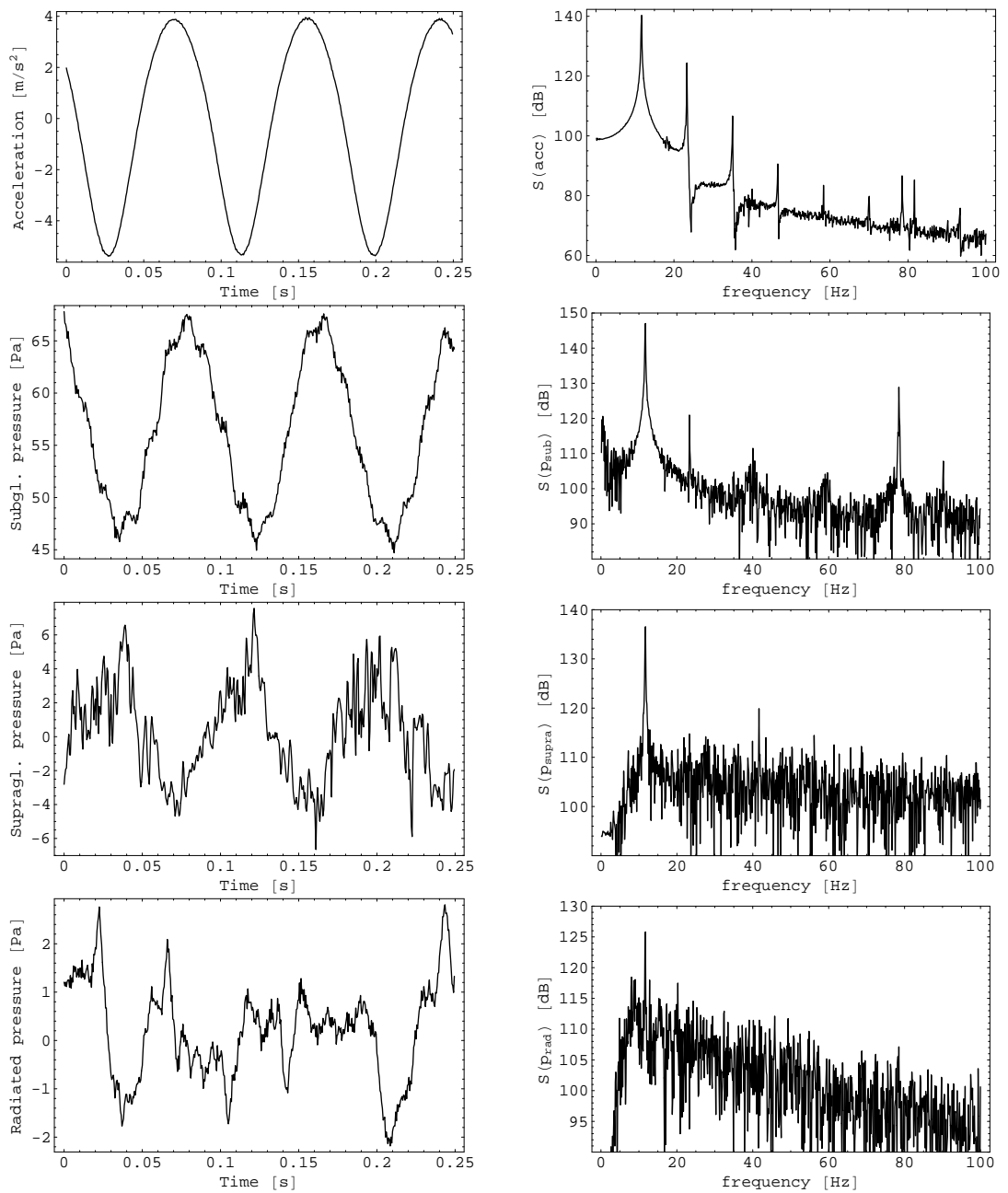


Figure 3.12: Waveforms and frequency spectra of the acceleration, subglottal pressure, supraglottal pressure and pressure radiated at the channel exit. Measurement No. 002 (mode I) – low flow rate $Q = 5.59$ l/s, impactless vocal fold vibration with a fundamental frequency of 11.7 Hz. The mechanical vibrations are nearly sinusoidal. The non-harmonic spectral frequency of 78.5 Hz, seen also in the spectrum of the subglottal pressure, corresponds probably to the rotational mode (with respect to z-axis, see Fig. 3.2) or to subglottal acoustic resonance. In the waveforms of the microphone signals prevails broadband noise, caused by the turbulent flow.

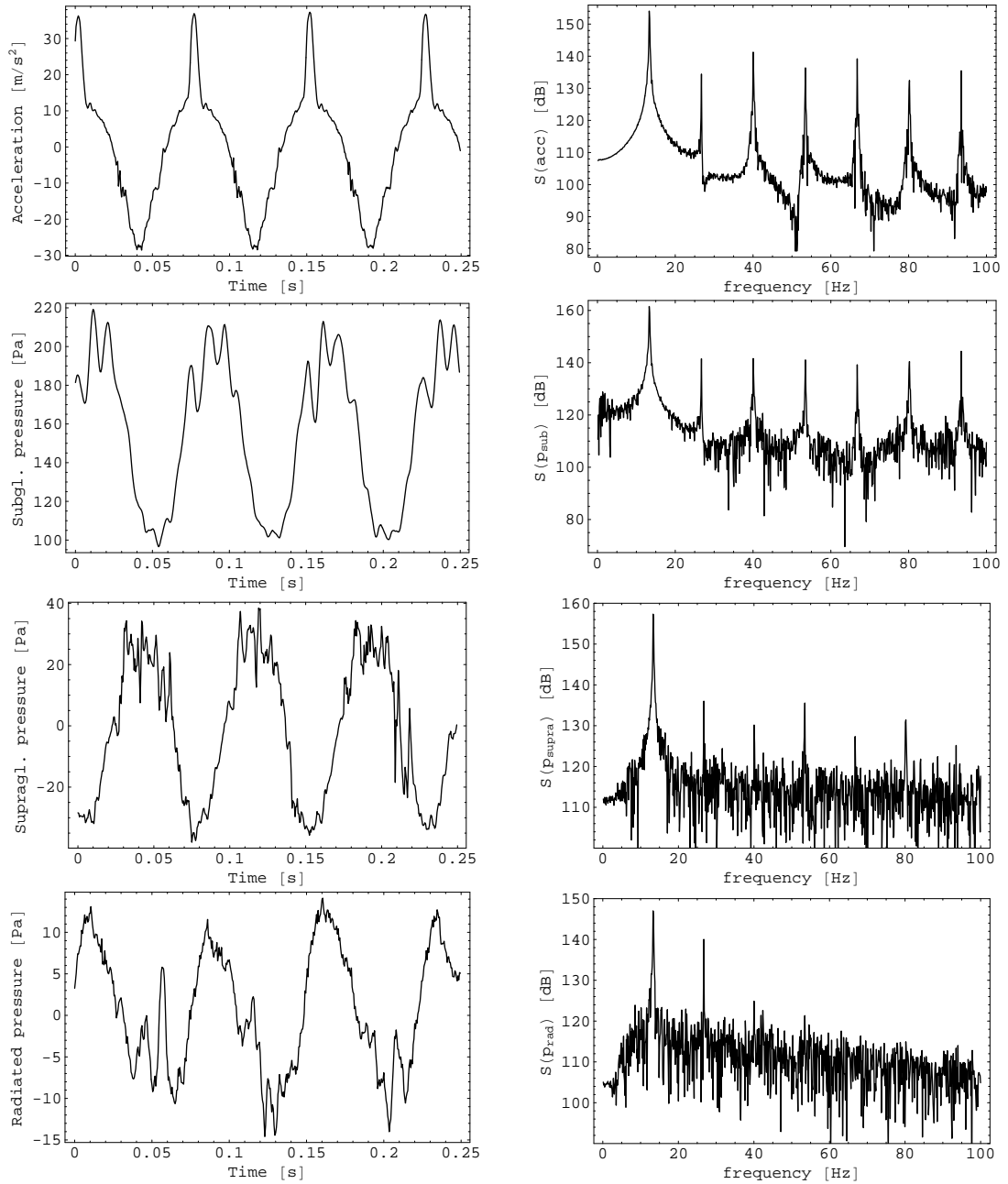


Figure 3.13: Waveforms and frequency spectra of the acceleration, subglottal pressure, supraglottal pressure and pressure radiated at the channel exit. Measurement No. 012 (mode II) – medium flow rate $Q = 8.58$ l/s, ideal for regular vocal fold vibration with an impact in each cycle. Fundamental frequency 13.2 Hz. On the acceleration waveform, the impact is clearly visible as a peak on the positive half-wave. The acoustic signals now show periodic structure, with harmonic frequencies in their spectra.

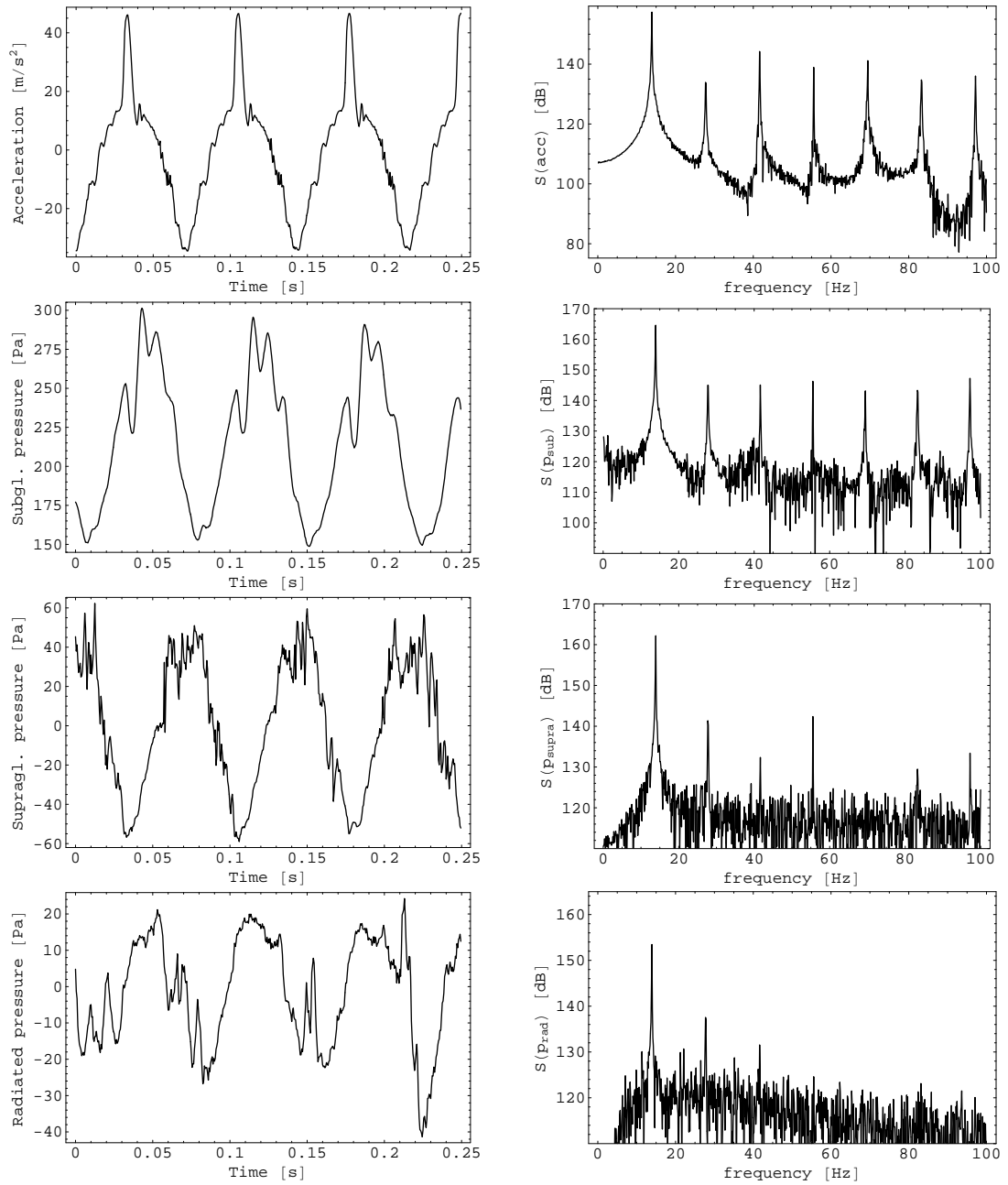


Figure 3.14: Waveforms and frequency spectra of the acceleration, subglottal pressure, supraglottal pressure and pressure radiated at the channel exit. Measurement No. 017 (mode III) – medium flow rate $Q = 10.47$ l/s, ideal for regular vocal fold vibration with an impact in each cycle. Fundamental frequency 13.8 Hz. The character of vibration does not differ substantially from mode II vibrations.

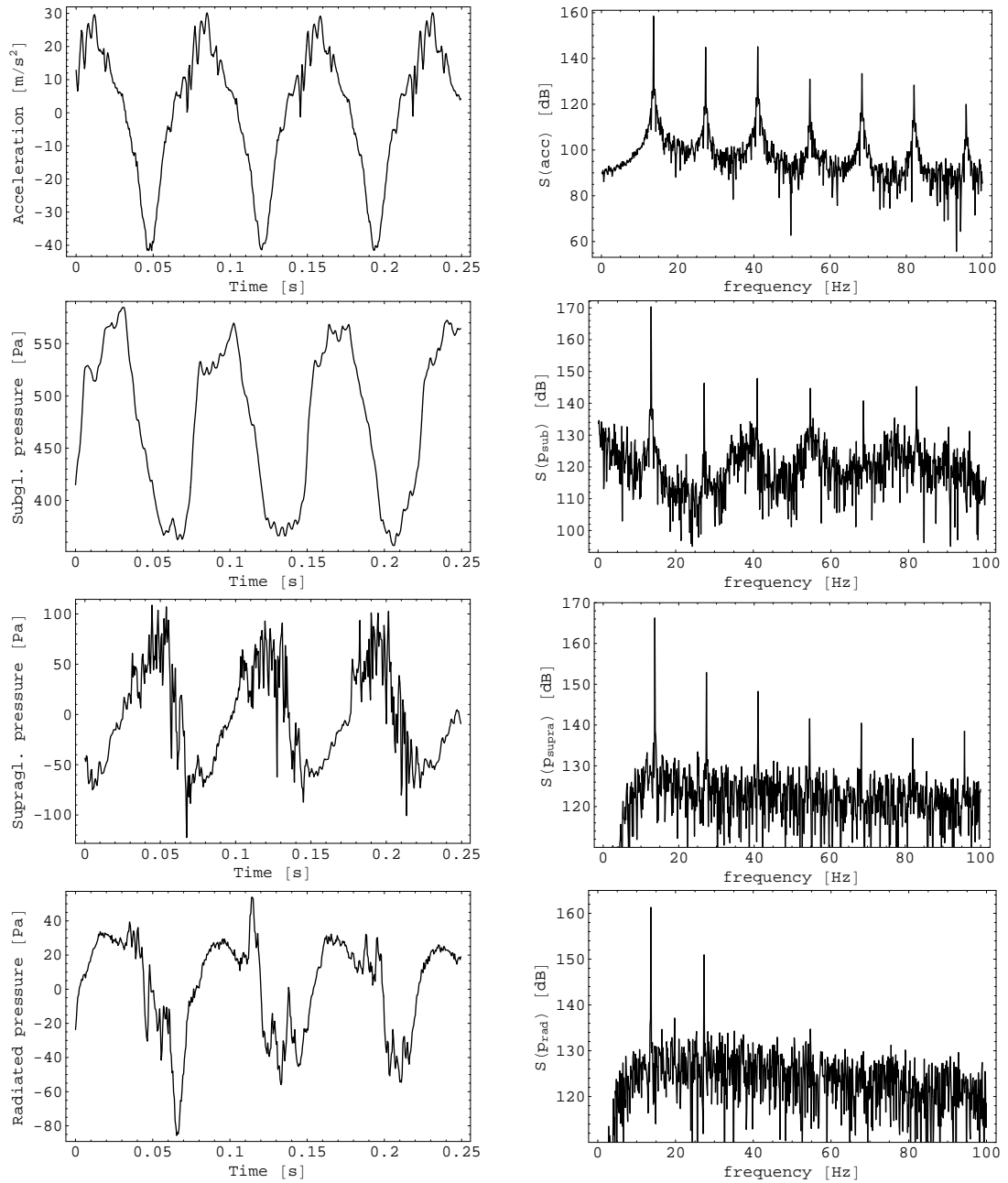


Figure 3.15: Waveforms and frequency spectra of the acceleration, subglottal pressure, supraglottal pressure and pressure radiated at the channel exit. Measurement No. 032 (mode IV) – high flow rate $Q = 17.87$ l/s induces partially irregular vibrations with lower accelerations and increased noise level in the acoustic signals. Fundamental frequency 13.5 Hz. The pressure and microphone waveforms are not perfectly periodical.

3.5 Results of the PIV measurements

An extensive series of PIV measurements was performed on the vibrating vocal fold model. The flow rate was gradually increased from $Q = 5.33$ l/s (measurement No.001) to $Q = 25.61$ l/s (measurement No.044). Within each of the 44 measurements, approximately 25 PIV records, corresponding to 25 distinct phases of the vocal fold oscillation cycle, were taken. This was realized using the synchronization signal (accelerometer signal converted to TTL) and the time-delay function of the laser control software. Each PIV record consisted of ten PIV measurements of the same phase within ten successive vibration cycles. Considering the total number of PIV measurements performed and taking into account the camera resolution of 1600×1200 pix, there is no surprise that the volume of the measured and post-processed data finally reached 40GB.

Basically, the post-processing comprised standard PIV calculation of the instantaneous velocity fields (division of the image into interrogation windows, cross-correlation, peak identification – as explained in section 3.1) and further the calculation of the phase-averaged velocity field. It is necessary to discern well between the *instantaneous* and the *phase-averaged* velocity fields. The instantaneous fields (which were ten for each flow rate and each phase, in our case) represent the real velocity distribution and capture all the flow structures (jet, vortices) of sufficiently large scale, i.e. comparable to the interrogation window size. The phase-averaged velocity field, on the other hand, provides statistic information about the mean flow for each phase chosen. It is calculated by a simple arithmetic average of the instantaneous fields related to the particular phase of vocal fold motion. Due to the fact, that the flow is not perfectly periodic, the phase-averaged fields usually do not show the small-scale vortices. In some cases, where the instantaneous velocity fields differ substantially (e.g. a free jet attached alternately to the top and bottom channel walls), the phase-averaged image may show completely useless information.

The examples of PIV camera images together with the resulting instantaneous velocity field are shown in Fig. 3.16. Fig. 3.17 demonstrates the calculation of the phase-averaged velocity fields. In all PIV images, the x and y axis labels correspond to the real dimensions (in mm). The measured flow velocities range from 0 to 35 m/s.

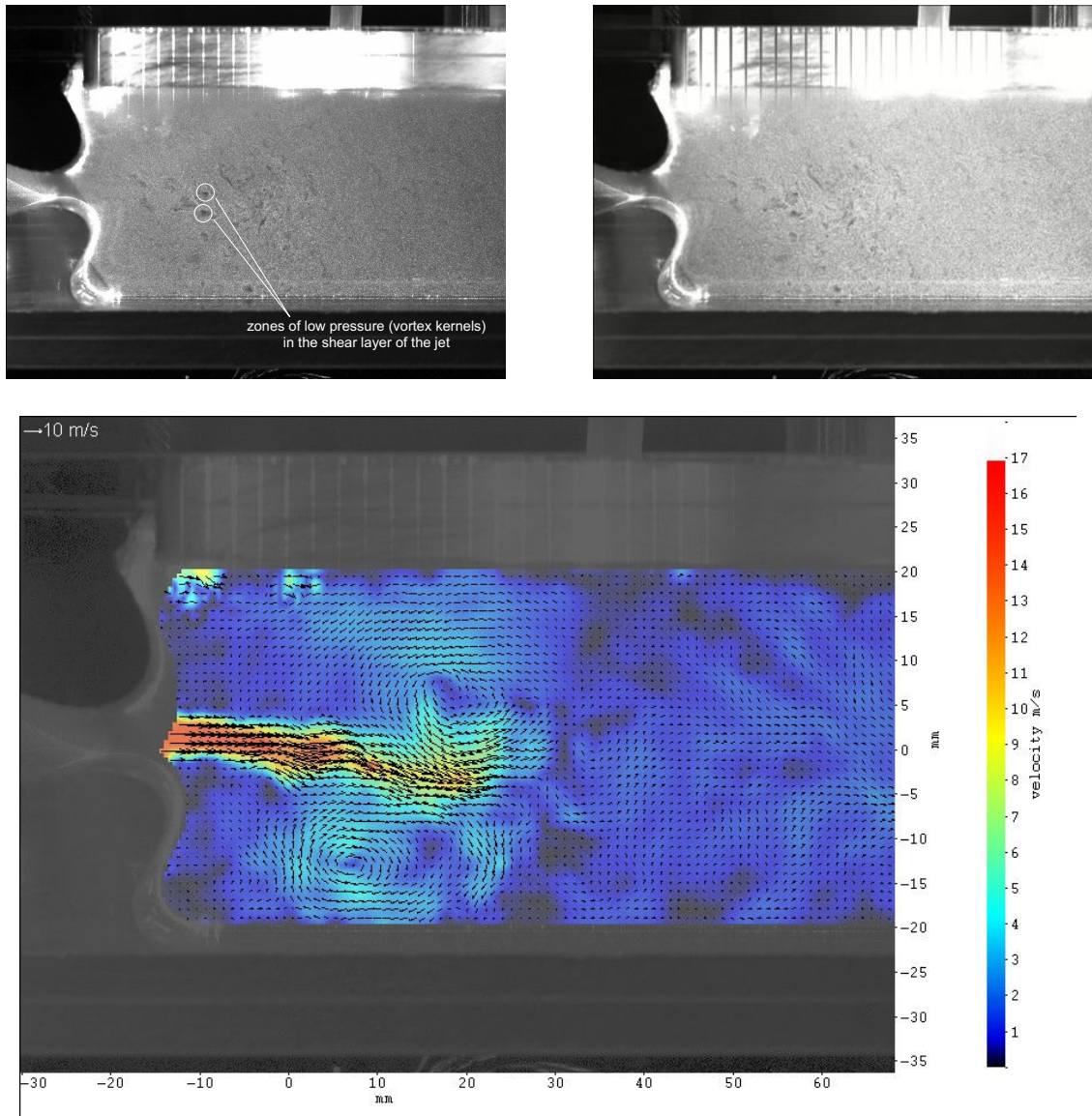


Figure 3.16: Instantaneous velocity field downstream the glottis. Two camera images with a time delay of $50 \mu\text{s}$ (top) acquired by illuminating the oil particles by the double-pulsed laser system. The small, dark circular zones (zones of low pressure) correspond to small-scale vortices developing in the boundary layer of the jet. Cross-correlation of the image signals gives the instantaneous velocity field (bottom). The vocal folds are on the left - the bottom one is fixed, the upper one is moving (the image is reversed vertically with respect to the real setup). The flow direction is from the left to the right. Example taken from measurement No.012, phase $t = 0 \text{ ms}$ (short after glottis opening). The velocity modulus is in color, arrows show the velocity direction and magnitude. A free jet with a maximum flow velocity of $U \approx 17 \text{ m/s}$ forms between the vocal folds. Two large-scale vortices develop at the sides of the jet front.

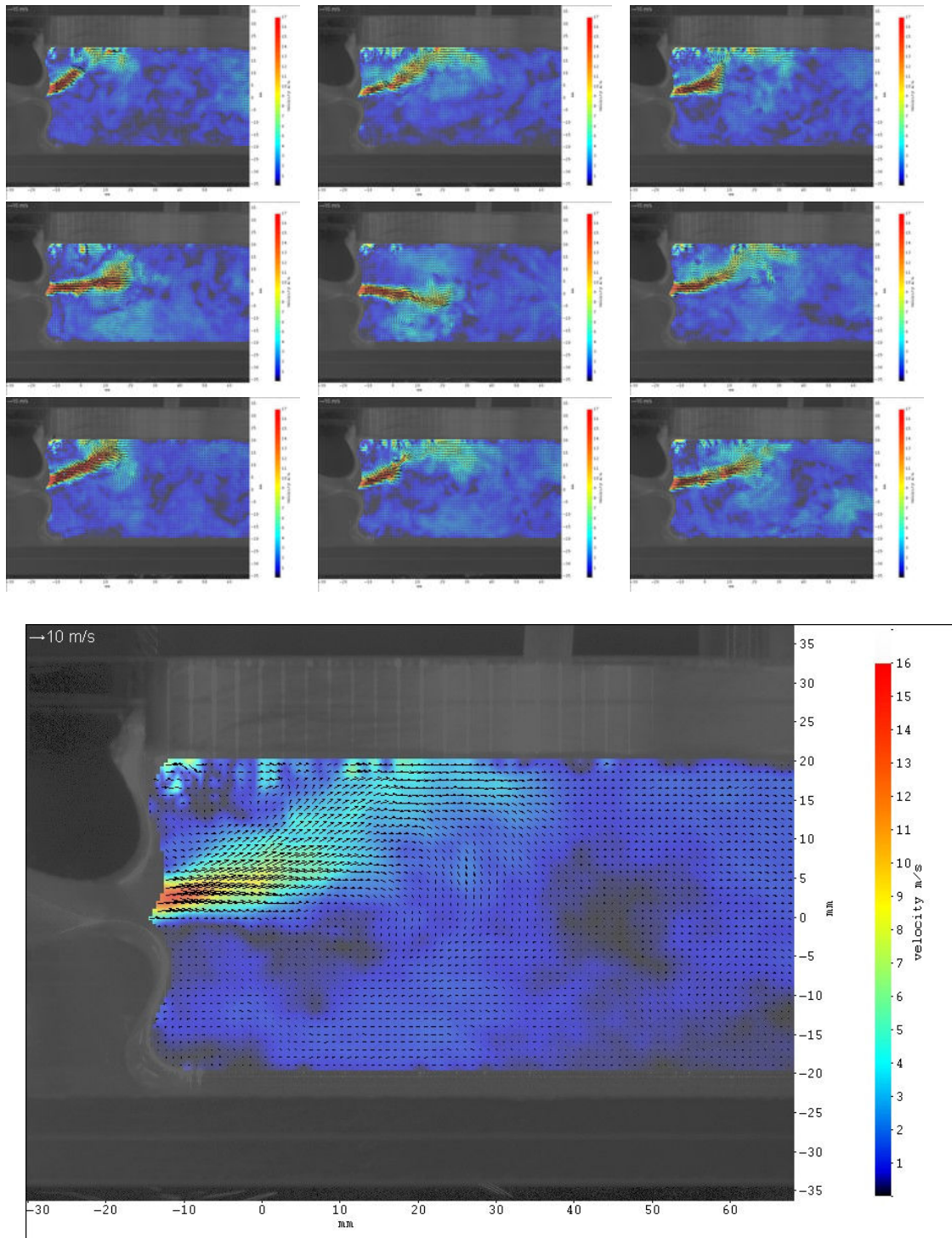


Figure 3.17: Calculation of the phase-averaged velocity field. Nine instantaneous velocity fields measured in the same phase of ten successive vibration cycles together with the calculated phase-averaged velocity field. Note the jet direction in the fifth instantaneous field, which is different from all the other cases. Example taken from measurement No.012.

The following figures demonstrate in detail the results of three selected measurements (out of 44 in total): measurement No.002, 012 and 032. These measurements were recorded at three different modes of vibration of the vocal fold: the first one was taken at low flow velocity, where the vocal fold vibrates with low amplitude without collisions (mode I); measurement No.012 was chosen as a representative case of medium flow rate, large-amplitude regular oscillations (mode II), which subjectively correspond the best to normal voice production; the last case, No.032, is an example of partially irregular oscillations induced by high flow rates (mode IV). The velocity fields for mode III (which is very similar to mode II) can be found on the DVD enclosed, which comprises the exported PIV images and calculated velocity fields in full resolution for all the cases measured.

The major difference between the velocity fields measured is first the maximum flow velocity of the free jet, which reaches 13 m/s, 18 m/s and 36 m/s, respectively. Considering the 3 ms delay between two successive vocal fold oscillation phases, one can estimate the distance which a particle may travel within the time which separates the phases. The second important difference is that in the first case (measurement No.002), the vocal folds do not collide and the jet is only slightly modulated. In the measurements No.012 and 032, on the other hand, the glottis closes completely and the flow is periodically interrupted.

In the majority of velocity fields measured, the jet is attached to the upper channel wall. This asymmetry is probably caused by the fact that the silicone molds of the upper and lower vocal folds were not perfectly identical in shape, and that only the upper vocal fold vibrated. Due to these asymmetries, the direction of the jet sorting glottis could already be inclined upwards, which would obviously make the jet attachment to the upper wall preferential.

It can be stated that the flow is not perfectly periodical in general. The turbulent structures, developing mainly due to presence of the boundary layer of the jet, interact mutually and with the jet in a disordered, stochastic way; this is why the flow fields of the same phase in successive oscillation cycles are not necessarily identical. The important flow structures, however, are generated periodically in accordance with the frequency of vibration: within each oscillation cycle, a new jet is created with one pair of large vortices propagating along the jet front. The jet attaches to the channel wall and during the closing phase it fades away and eventually disappears, leaving the turbulence to damp out.

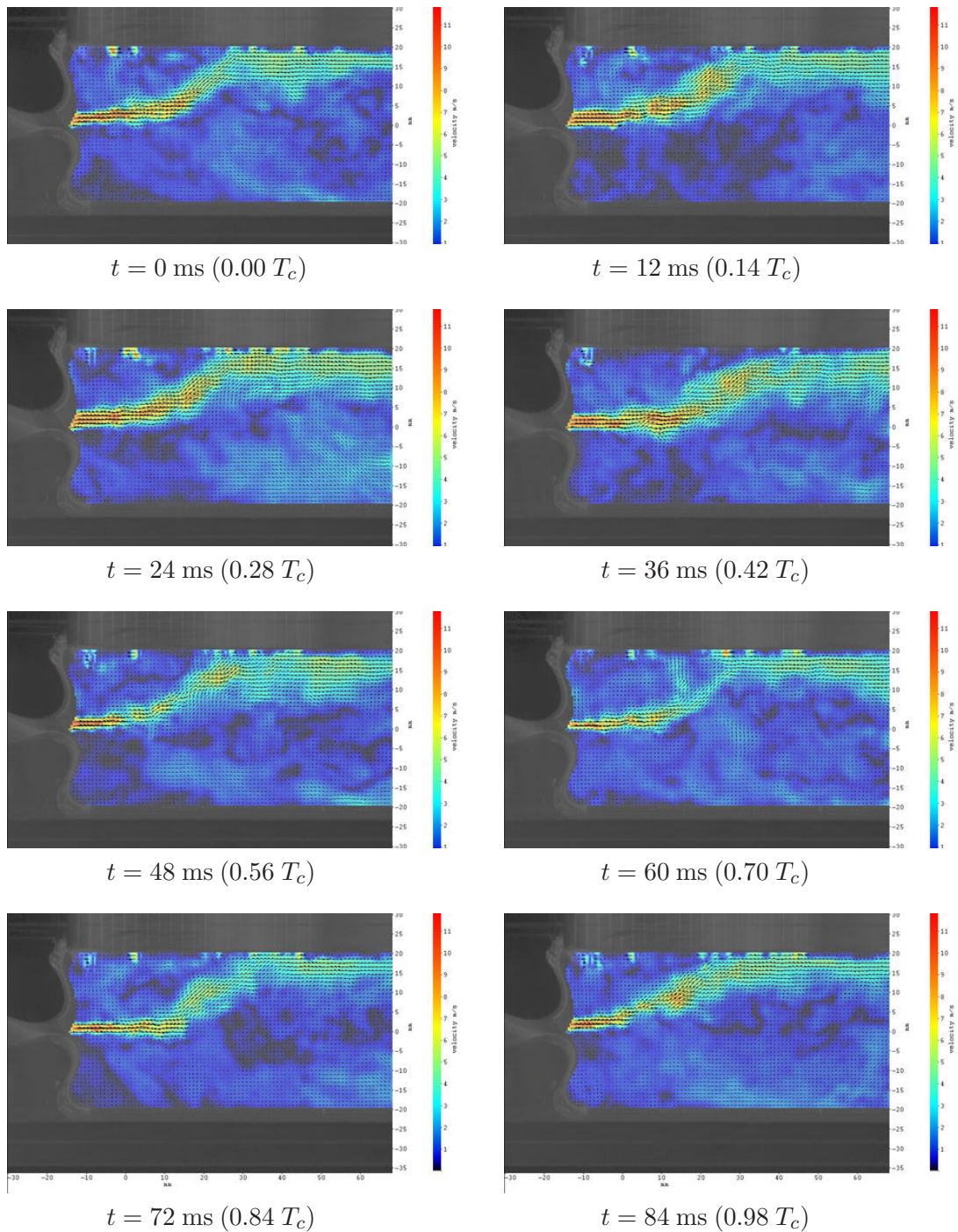


Figure 3.18: Selected instantaneous velocity fields downstream the glottis – measurement No. 002 (low flow rate $Q = 5.59 \text{ l/s}$ – mode I). For low flow rates, the vocal folds do not collide and the channel remains open throughout the entire cycle. The jet is not interrupted and just slightly modulated by the variable glottis aperture.

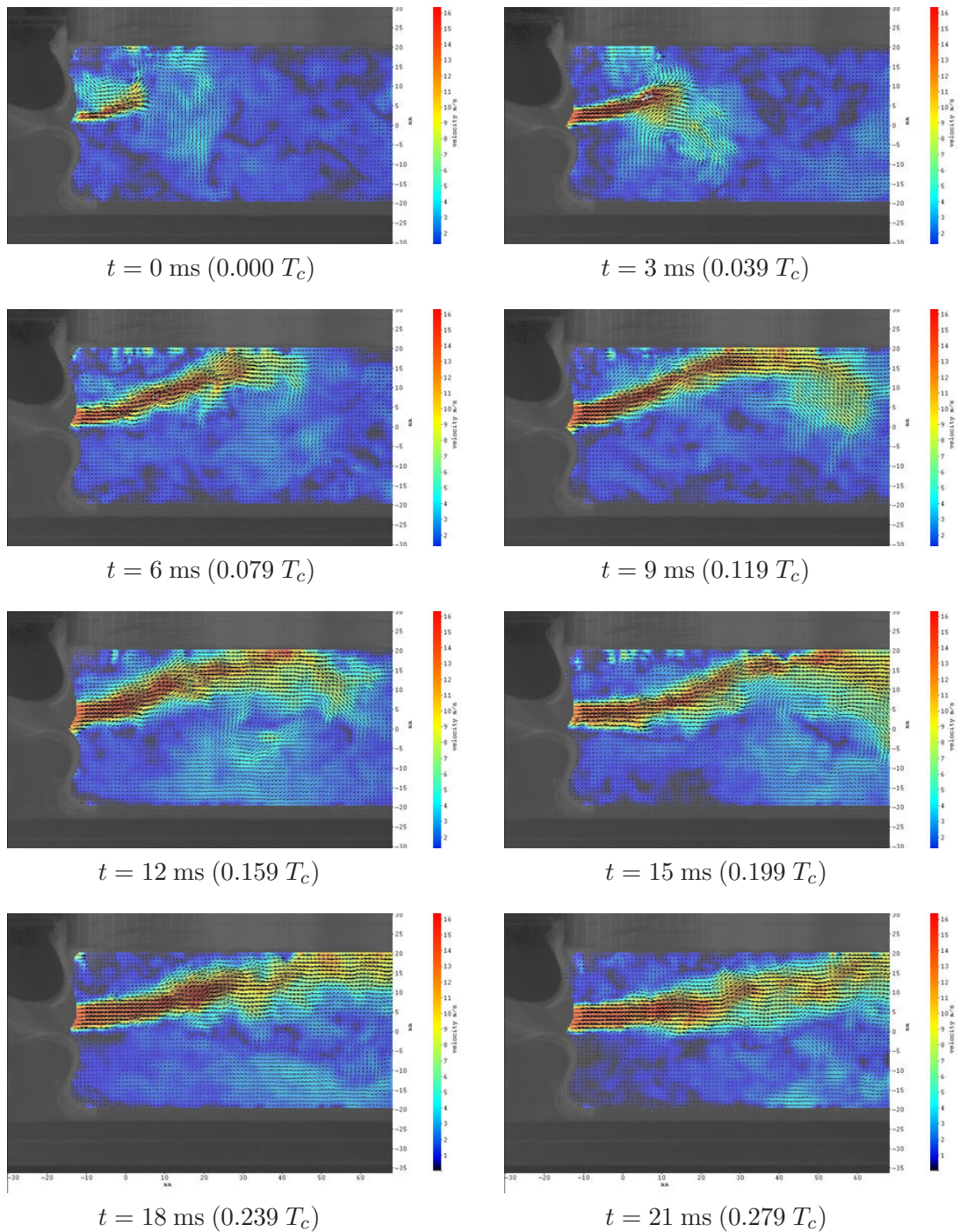


Figure 3.19: Selected instantaneous velocity fields downstream the glottis – measurement No. 012 (medium flow rate $Q = 8.58 \text{ l/s}$ – mode II), glottis opening. The jet forms between the vocal folds and later attaches to the channel wall. Two vortices come along with the jet front (see full-resolution images on the DVD).

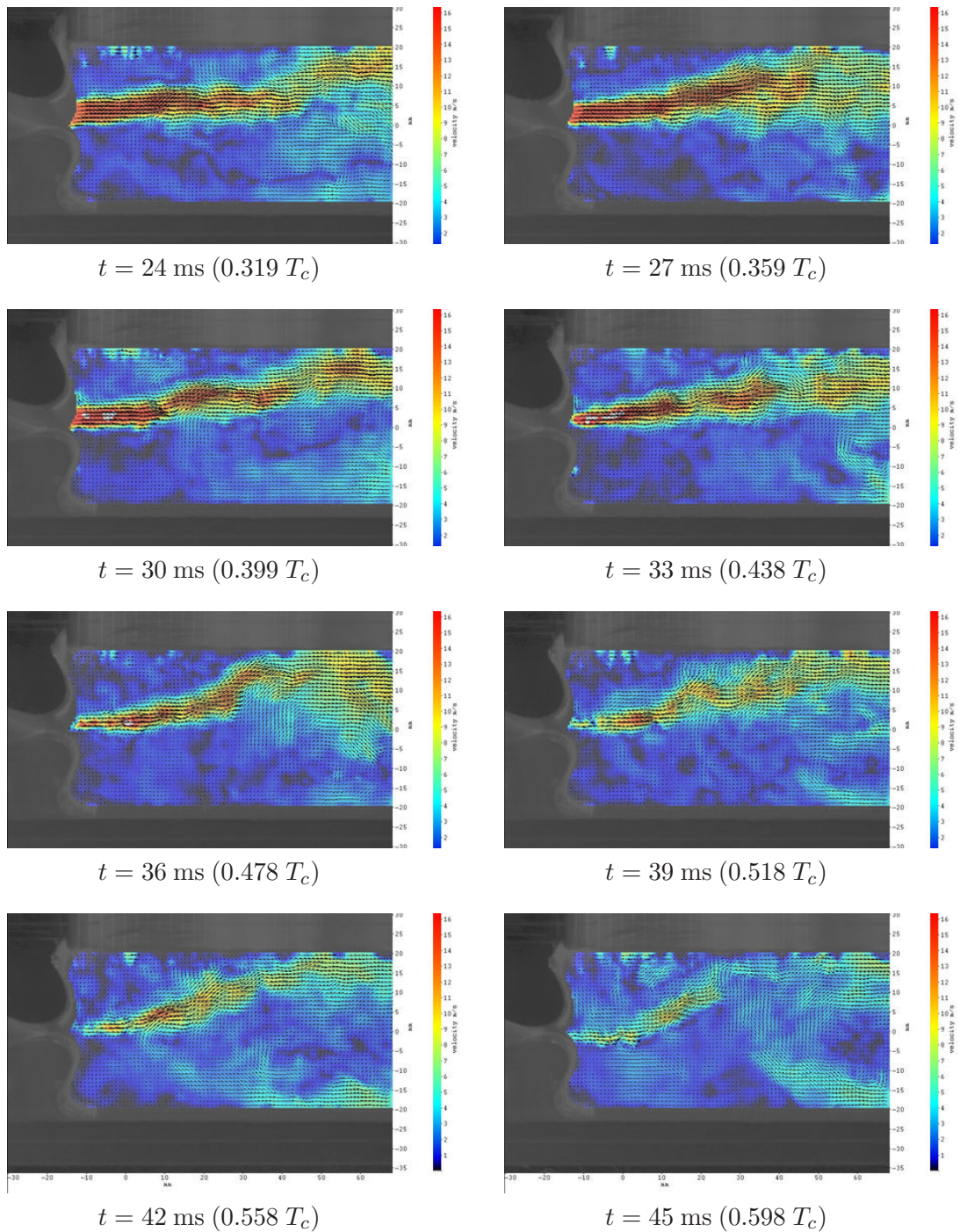


Figure 3.19: (continued) Selected instantaneous velocity fields downstream the glottis – measurement No. 012 (medium flow rate $Q = 8.58 \text{ l/s}$ – mode II), glottis closure. As the vocal folds approach each other, the jet becomes weaker and after $t = 45 \text{ ms}$ it disappears.

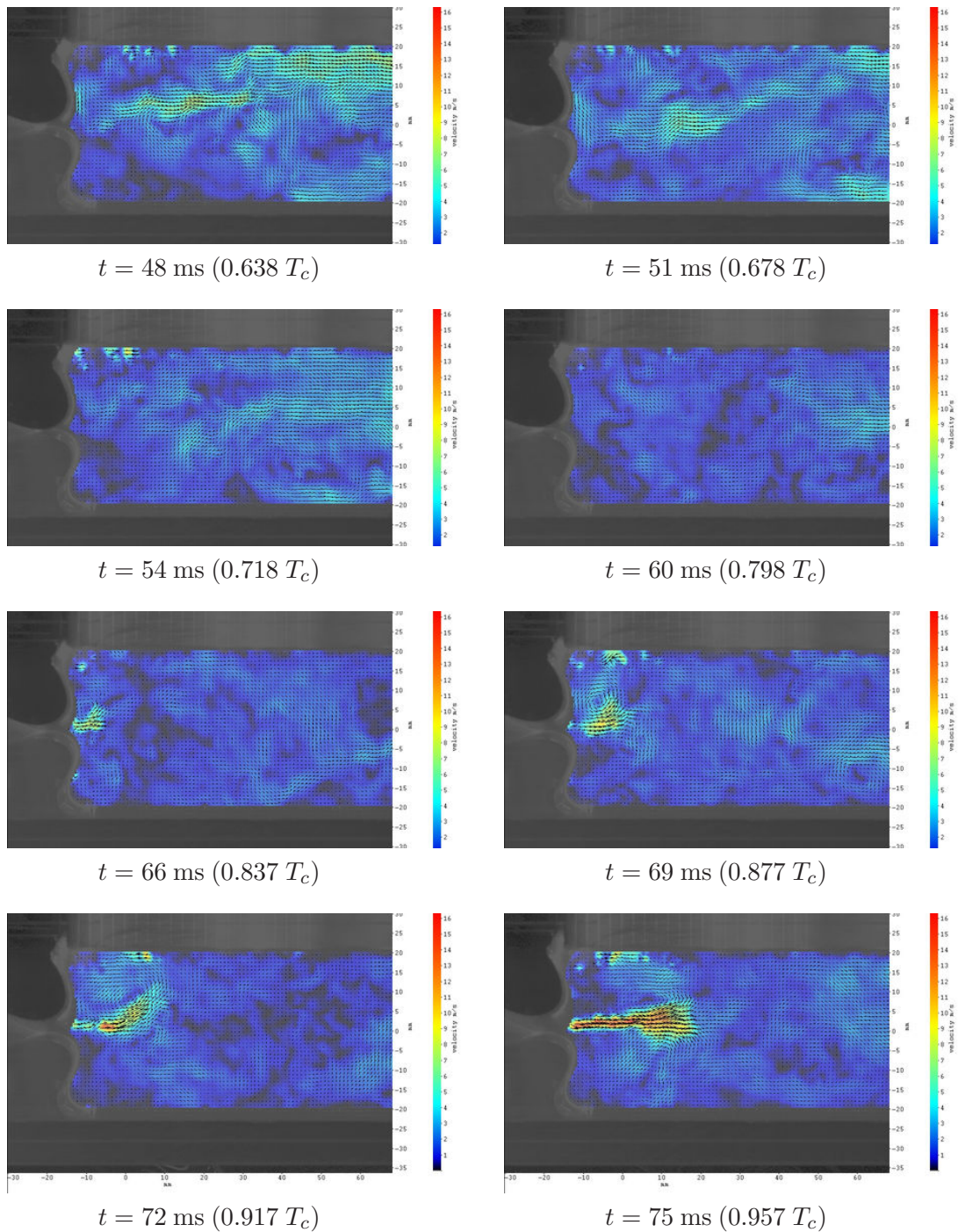


Figure 3.19: (continued) Selected instantaneous velocity fields downstream the glottis – measurement No. 012 (medium flow rate $Q = 8.58 \text{ l/s}$ – mode II), glottis closure, vocal fold collision and glottis reopening. During the closure, no bulk flow is present and only residual turbulence is visible (phases 57 ms and 63 ms similar to images 54 ms and 60 ms are thus omitted). In the last two phases, a new jet develops.

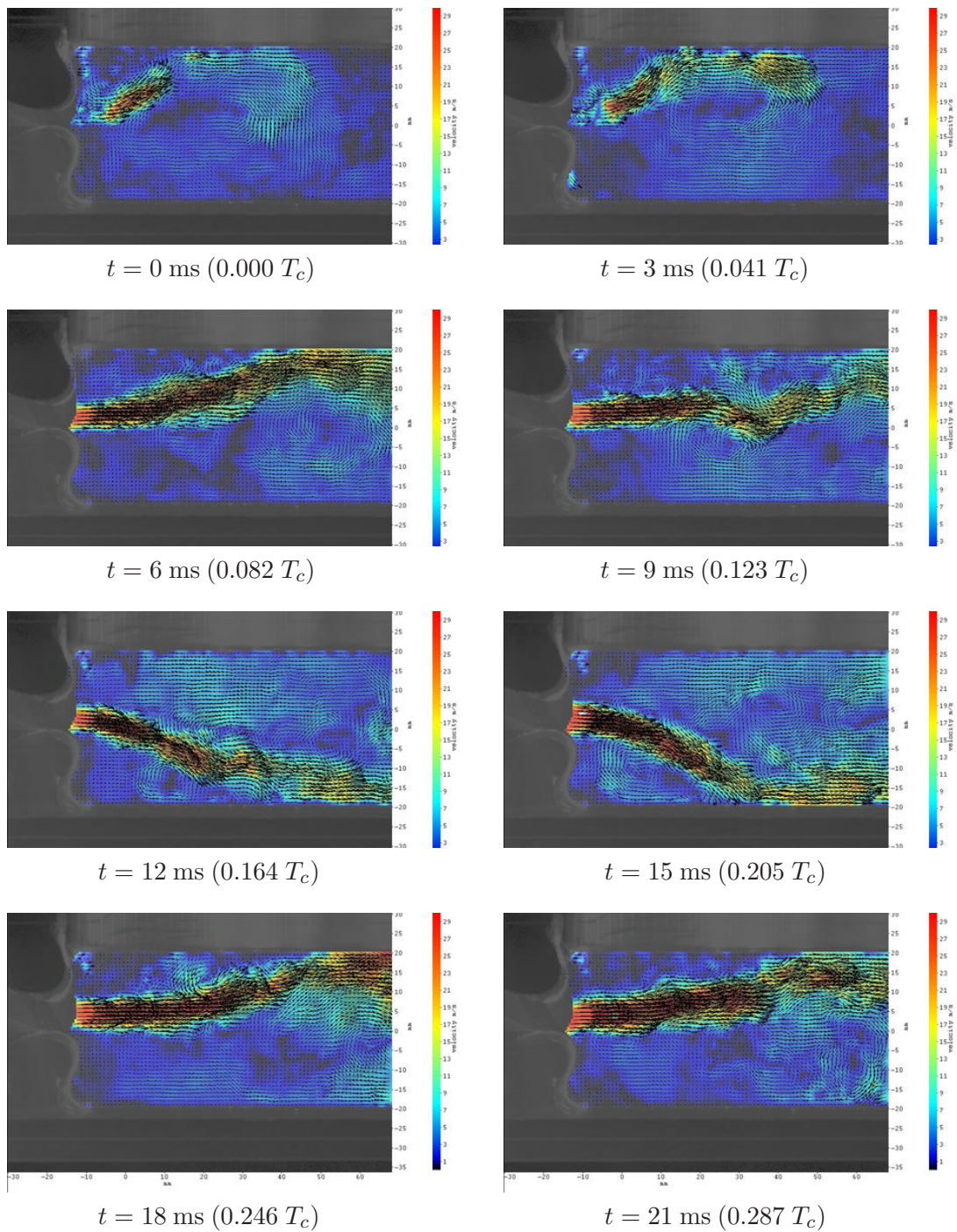


Figure 3.20: Selected instantaneous velocity fields downstream the glottis – measurement No. 032 (high flow rate $Q = 17.87 \text{ l/s}$ – mode IV), glottis opening. The free jet forms and attaches to the channel wall - in the majority of cases to the upper wall, but in some cycles and phases to the bottom one.

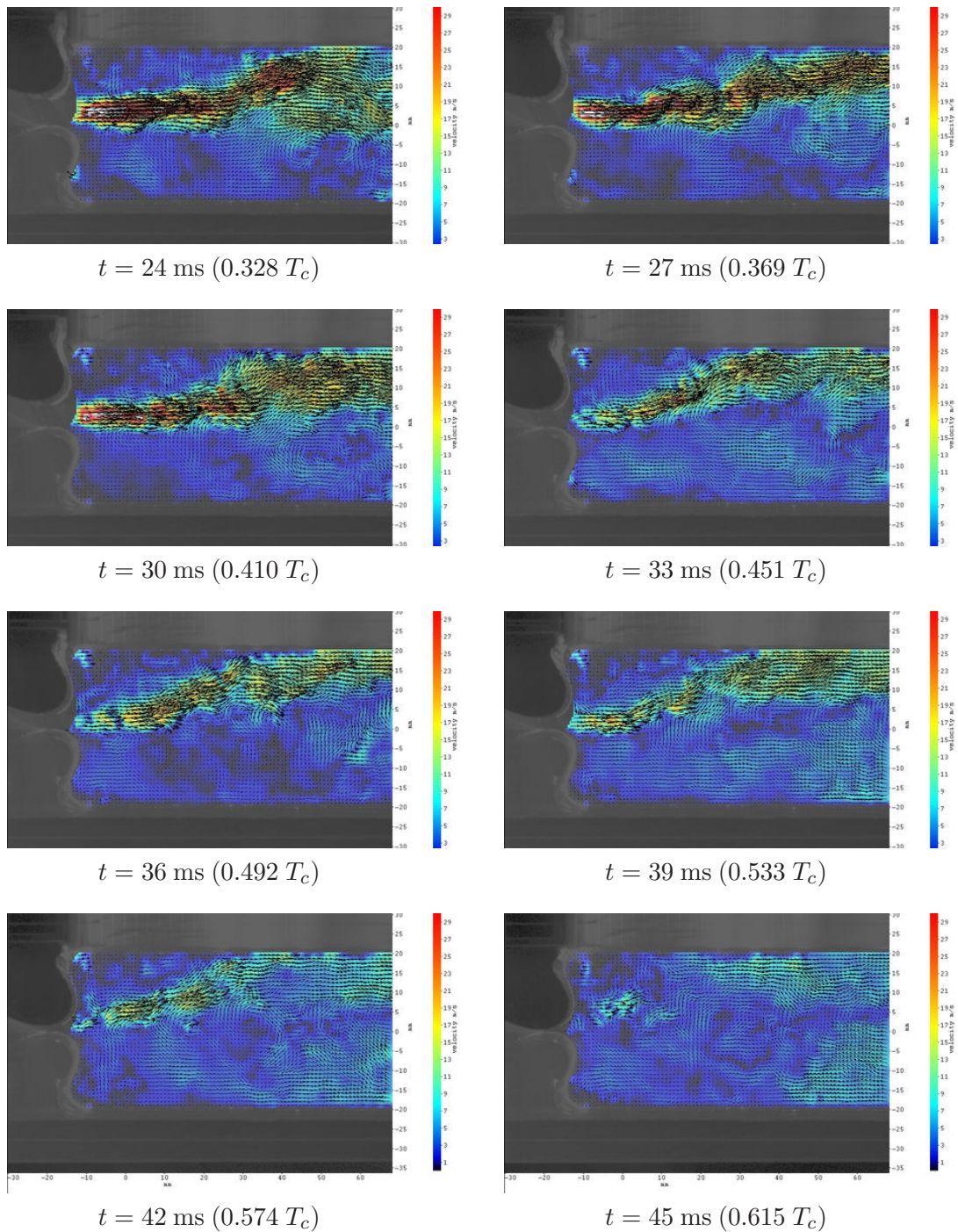


Figure 3.20: (continued) Selected instantaneous velocity fields downstream the glottis – measurement No. 032 (high flow rate $Q = 17.87 \text{ l/s}$ – mode IV), glottis closure. The maximum jet velocity reaches 35 m/s and gradually diminishes until complete jet interruption. In the bottom part of the domain, important recirculation is evident (see also the full-resolution images on the DVD).

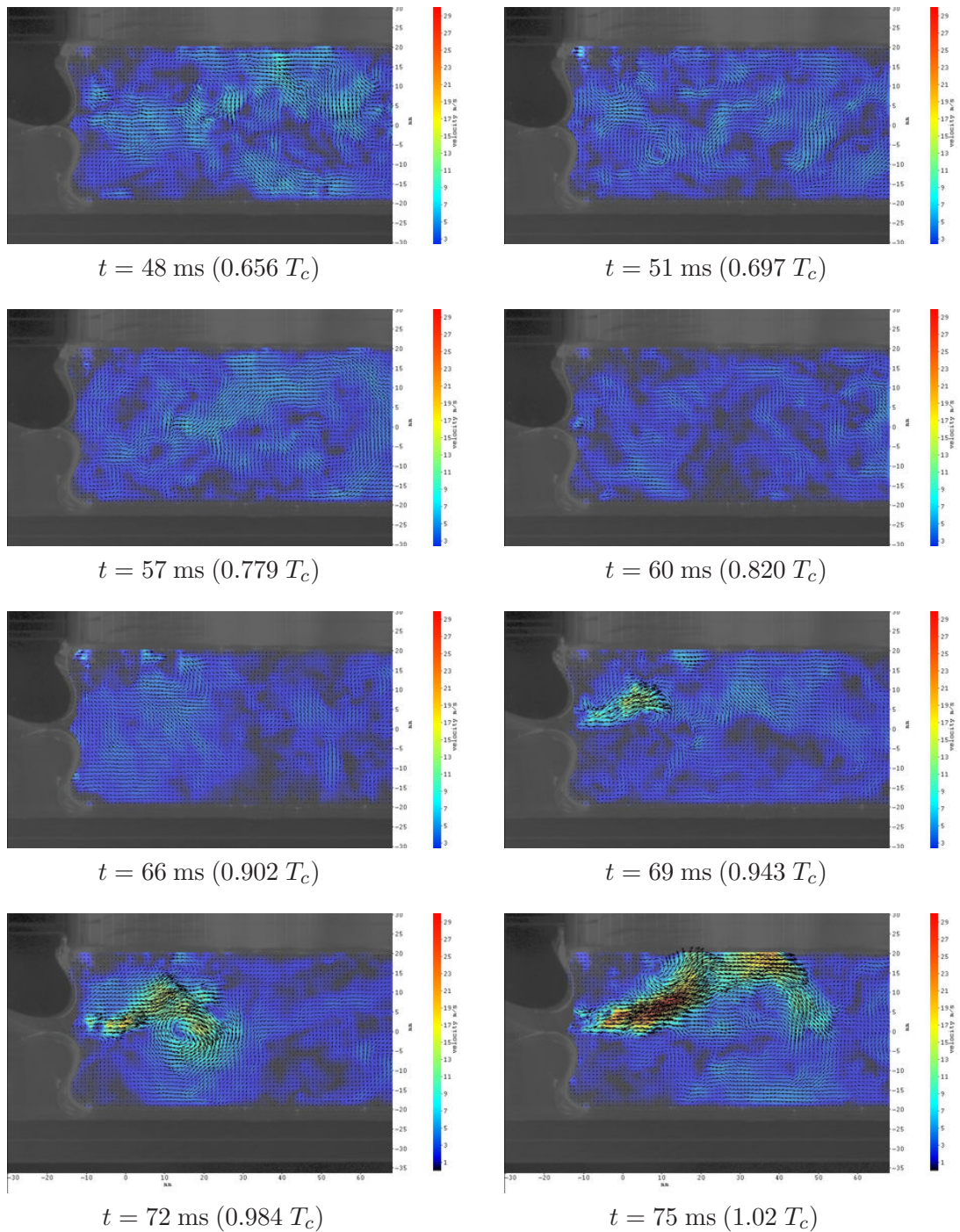


Figure 3.20: (continued) Selected instantaneous velocity fields downstream the glottis – measurement No. 032 (high flow rate $Q = 17.87 \text{ l/s}$ – mode IV), glottis closure, vocal fold collision and glottis reopening. Images 54 ms and 63 ms omitted. Residual turbulence during closure, development of a new jet after opening.

Chapter 4

Discussion and conclusions

A new mathematical model of 2D viscous flow, interacting with an elastic body in the wall of the channel, was developed. The non-stationary incompressible Navier-Stokes equations were derived in the Arbitrary Lagrangian-Eulerian (ALE) approach, which allows to deal with time-dependent (deforming) computational domains. The Navier-Stokes equations were discretized by the Finite element method (FEM), using the Taylor-Hood P^2/P^1 elements for the velocity and pressure functions. The numerical scheme was completely programmed in the Fortran language, making use only of open-source libraries for the finite element discretization and for the numerical solution of the resulting linear system. The code allows to run numerical simulations of flow past vibrating vocal folds, to study the development of the velocity and pressure fields and to observe and quantify the effects like vortex shedding, flow separation and modulation of the jet formed between the vocal folds.

To obtain experimental feedback and to validate the mathematical model, a new 4:1 scaled physical model of vocal folds was designed and fabricated. After an extensive series of computations, tests and modifications, we succeeded to develop a model, where the vocal fold vibrates only due to flow-structure interaction – unlike most of the models developed by other research teams, where the vibration is excited externally. The signals from accelerometers, pressure transducers and measuring microphones mounted on the measuring section make possible to identify the mechanical properties and acoustical output of the model. The wind tunnel was adapted in such a way, that it allows velocity field measurements by the Particle Image Velocimetry (PIV) immediately upstream the vibrating vocal fold. The PIV images from the measurements synchronized with the vibration reveal similar flow structures as the results of numerical simulations.

When modeling vocal fold oscillations or glottal flow, it is tempting to try to compare the model outputs with physiological data known from literature as soon as some results are obtained. It is however necessary to take into account the limitations of the models and not to try to extrapolate beyond the scope for which the models were designed: it is not plausible, for example, to draw systematic conclusions regarding vortex shedding in glottis from a 1D flow model.

Neither the mathematical nor the physical model, described within this thesis, was primarily intended for direct comparison with real human vocal folds. The main goal of the study was to develop a mathematical model of 2D viscous flow in a channel comprising vibrating vocal folds. Since the experimental data regarding velocity fields in glottis are nearly impossible to obtain from living subjects, a mechanical vocal fold model was designed. The strategy is hence first to vali-

date the mathematical model using results of the PIV measurements on the physical model; once a satisfactory correspondence between the computational and physical models will be achieved, the geometry and boundary conditions of the mathematical model can be modified in order to reflect the conditions occurring in real vocal folds. For the validation of the model, it was advantageous to use the configuration with one vocal fold moving and the other fixed.

The results from the mathematical and physical model obtained so far seem to correspond when compared visually. Nevertheless, it should be noted that there are some aspects, which make a systematic comparison difficult for the time being. As regards the physical model, the situation is complicated by the dynamic similarity: due to the 4 : 1 scale, different frequencies of vibration and critical flow velocities, the important dimensionless characteristics (i.e. Reynolds and Strouhal numbers) were close to the real situation, but not identical. Moreover, the leakage alongside the vibrating element, which was inevitable due to technical issues, is obviously not present in real vocal folds; it is not evident whether the leakage represents an effect of secondary importance or whether it can alter the flow regime or the instability type significantly.

The main limitation of the mathematical model is the fact that the vocal folds are not allowed to collide. The processes accompanying glottal closure are complex and from the algorithmic point of view, the separation of the computational domain into two, necessity to introduce additional boundary conditions and to handle pressure discontinuity when reconnecting the domains represent a very complicated problem. Yet it will be necessary to deal with this task in future, if the mathematical model should be employed to model regular loud phonation.

The next issue which should be addressed is to introduce coupling between the flow and the mechanical vibration. In the results shown here, the vibration of the vocal fold was prescribed according to the data measured on the physical model; to model the true interaction it is necessary to evaluate the aerodynamic forces in each time level and perform a timestep in the equations of motion. This represents no principal problem and has already been done within the master thesis [30] in a quasi-1D fluid-structure interaction model. In the 2D model, however, this will require certain technical effort to implement. Moreover, it will be necessary to specify the constants regarding the stiffness and damping of the support, which is not trivial.

There is one more source of discrepancy between the mathematical and physical model. At the beginning of this study, an assumption has been made that the flow fields in glottis are in the first approximation two-dimensional. This is indeed the case for the very proximity of a 2D obstacle, which has a strong capability to bi-dimensionalize the flow (provided that the channel is sufficiently wide to suppress the influence of the lateral walls and corners of the channel, which introduce peripheral 3D flow structures). As regards the channel further upstream a barrier, however, the vortex dynamics in 2D and in 3D are substantially different. In the 2D situation, which does not actually exist in reality and which represents only a conceptual simplification, the vorticity vector

$$\boldsymbol{\omega} = \text{curl } \boldsymbol{u} \equiv \nabla \times \boldsymbol{u}$$

is always perpendicular to the flow plane (i.e. parallel to the obstacle axis) and the only mechanism of vortex vanishing are the viscous effects. In the real, 3D case, on the contrary, the large-scale vortices, whose axis is originally also parallel to the obstacle orientation, tend to slew into the flow direction. As a result, the vortices detected in the PIV plane of the 3D vocal fold model seem to

“disappear” much faster than the eddies predicted by the 2D mathematical model. The computational model could be improved by introducing some kind of turbulence modeling (e.g. Reynolds Averaged Navier-Stokes equations, Large Eddy Simulations), but this does not solve the problem completely. The turbulence models are designed rather as an approximate, computationally more effective alternative to direct numerical simulations which fail to predict the influence of small, sub-grid eddies; they are not intended to model the 3D effects in 2D. Moreover, the specific turbulence models were mostly derived for specific configurations and their validity is not guaranteed universally. The only reliable method is thus the simulation in 3D. Both the mathematical description and the computer code are ready for the 3D case; the full three-dimensional modeling, however, will require much more computational power and also specification of the 3D vocal tract geometry.

As explained in the previous paragraphs, a thorough verification of the mathematical model by means of the measured data is difficult at the current state; yet the results obtained are promising and important from the methodological point of view. The mathematical model was originally based on the works of Feistauer, Sváček and Horáček [40, 39] on numerical solution of flow-induced airfoil vibrations. It was adapted for low Reynolds numbers and for a body vibrating in the channel wall, and completely reprogrammed in the Fortran language using the numerical library *Mélina*. The new implementation has several advantages – mainly the possibility to use triangular, quadrangular, tetrahedral, prismatic and hexahedral meshes and higher-order interpolations (up to P6 or Q20) in 2D or 3D. Furthermore, a different algorithm was used for the calculation of the ALE-mapping, which is crucial for the deformation of the computational mesh during vocal fold oscillations. Unlike the latter studies, where the ALE-mapping was expressed from geometrical considerations or from the solution of the elastic problem, here it was obtained as the solution of the Laplace equation.

The next feature of the mathematical model, which could be improved, is the mechanical part of the model. So far, the vocal fold has been modeled as a two-degree-of-freedom rigid body supported by linear springs and dampers. In future, the deformations of the soft elastic tissue could be modeled by the finite element method, too. This will, however, require to supply a number of geometrical and material data regarding the diverse tissue structures, which form the vocal fold; this appears to be the stumbling-block of the currently existing FE vocal fold models found in literature [15, 42, 46].

As regards the physical model, it seems to be a promising alternative to the vocal fold models developed by other scientific teams over the world [8, 42, 22]. To the best knowledge of the author, there are not many mechanical self-oscillating vocal fold models which have been employed so far to measure the supraglottal flow fields; hopefully, the model will allow us to perform further interesting measurements and help to disclose some of the not completely understood features of voice production in human vocal folds.

References

- [1] ALIPOUR, F., AND TITZE, I. R. Combined simulation of two-dimensional airflow and vocal fold vibration. In *Vocal fold physiology: controlling complexity and chaos* (San Diego, 1996), pp. 17–29.
- [2] BARNEY, A., SHADLE, C. H., AND DAVIES, P. Fluid flow in a dynamic mechanical model of the vocal folds and tract. Measurements and theory. *Journal of the Acoustical Society of America* 105 (1999).
- [3] BLEVINS, R. D. *Flow-induced vibration*. Van Nostrand Reinhold Company, New York, N.Y., USA, 1977.
- [4] BUNCH, M. *Dynamics of the singing voice*. Vienna: Springer-Verlag, 1982.
- [5] CIHLÁŘ, J., ANGOT, P., AND FEISTAUER, M. On the discretization and iterative solvers for viscous incompressible flow. In *Proceedings of conference Numerical Modelling in Continuum Mechanics* (Prague, Czech Republic, 1997).
- [6] DANTEC DYNAMICS A/S. Measurement Principles of PIV, 1997–2005. <http://www.dantecdynamics.com/piv/princip> [Online; accessed 21 September 2006].
- [7] DAVIS, T. A. UMFPack: unsymmetric multifrontal sparse LU factorization package. University of Florida, Gainesville, FL, USA. <http://www.cise.ufl.edu/research/sparse/umfpack/> [Online; accessed 29 November 2006].
- [8] DEVERGE, M., PELORSON, X., VILAIN, C., LAGREE, P., CHENTOUF, F., WILLEMS, J., AND HIRSCHBERG, A. Influence of collision on the flow through in-vitro rigid models of the vocal folds. *Journal of the Acoustical Society of America* 114 (2003), 3354–3362.
- [9] DOLEJŠÍ, V. Angener v3.1. Department of Numerical Mathematics of the Charles University, Prague, Czech Republic. <http://www.karlin.mff.cuni.cz/~dolejsi/angen/angen3.1.htm> [Online; accessed 29 November 2006].
- [10] DOWEL, E. *A modern course in aeroelasticity*. Sijthoff & Noordhoff International Publishers B. V., Alphen aan den Rijn, 1978.
- [11] FEISTAUER, M. *Mathematical methods in fluid dynamics*. Longman, Harlow, 1993.
- [12] FEISTAUER, M., FELCMAN, J., AND STRAŠKRABA, I. *Mathematical and computational methods for compressible flow*. Clarendon Press, Oxford, 2003.

- [13] GIRAULT, V., AND RAVIART, P.-A. *Finite element methods for the Navier-Stokes equations*. Springer-Verlag, Berlin, 1986.
- [14] GOTO, K. Goto BLAS. Texas Advanced Computing Center, University of Texas, Austin, TX, USA. <http://www.tacc.utexas.edu/resources/software/> [Online; accessed 29 November 2006].
- [15] GUNTER, H. E. A mechanical model of vocal-fold collision with high spatial and temporal resolution. *Journal of the Acoustical Society of America* 113 (2003), 994–1000.
- [16] HEYWOOD, J., RANNACHER, R., AND TUREK, S. Artificial boundaries and flux and pressure conditions for the incompressible Navier-Stokes equations. *International Journal for Numerical Methods in Fluids* 22 (1996), 352–352.
- [17] HORÁČEK, J., ŠIDLOF, P., AND ŠVEC, J. G. Numerical simulation of self-oscillations of human vocal folds with Hertz model of impact forces. *Journal of Fluids and Structures* 20 (2005), 853–869.
- [18] HORÁČEK, J., ŠVEC, J. G., VESELÝ, J., VILKMAN, E., AND KLEPÁČEK, I. Measurement of the vocal-fold vibration behaviour in excised human larynges. In *International Workshop on Models and Analysis of Vocal Emissions for biomedical Applications* (Firenze, Italy, 13 – 19 September 2001), pp. 1–6.
- [19] HORÁČEK, J., VESELÝ, J., AND URUBA, V. Aeroelastic instability of a plate flexibly mounted in the channel wall (Aeroelastická nestabilita pružně uložené desky ve stěně kanálu, in Czech). *Engineering Mechanics* (1997), 335–348.
- [20] ISHIZAKA, K., AND FLANAGAN, J. Synthesis of voiced sounds from a two-mass model of the vocal cords. *The Bell System Technical Journal* 51 (1972), 1233–1268.
- [21] JOHNS HOPKINS MEDICINE, THE CENTRE FOR LARYNGEAL AND VOICE DISORDERS. The larynx and voice: Basic anatomy and physiology. <http://www.hopkinsmedicine.org/voice/anatomy.html> [Online; accessed 22 January 2007].
- [22] KOB, M., KRÄMER, S., PRÉVOT, A., TRIEP, M., AND BRÜCKER, C. Acoustic measurement of periodic noise generation in a hydrodynamical vocal fold model. In *Proceedings of Forum Acusticum* (Budapest, Hungary, 29 August – 2 September 2005), pp. 2731–2736.
- [23] LILJENCANTS, J. A translating and rotating mass model of the vocal folds. Quarterly progress and status report 1/1991, Speech transmission laboratory, Stockholm, Sweden, 1991.
- [24] LOUS, N., HOFMANS, G., VELDHUIS, R., AND HIRSCHBERG, A. A symmetrical two-mass vocal-fold model coupled to vocal tract and trachea, with application to prosthesis design. *Acta Acustica* 84 (1998), 1135–1150.
- [25] LUCERO, C. L. Chest and falsetto-like oscillations in a two-mass model of the vocal folds. *Journal of the Acoustical Society of America* 100 (1996), 3355–3359.
- [26] MARTIN, D. Finite element library Mélima. Université de Rennes, Unité de Mathématiques Appliquées, ENSTA Paris, France. <http://perso.univ-rennes1.fr/daniel.martin/melina/> [Online; accessed 29 November 2006].

- [27] NOMURA, T., AND HUGHES, T. J. An arbitrary Lagrangian-Eulerian finite element method for interaction of fluid and a rigid body. *Computer methods in applied mechanics and engineering* 95 (1992), 115–138.
- [28] PELORSON, X., HIRSCHBERG, A., VAN HASSEL, R., AND WIJNANDS, A. Theoretical and experimental study of quasisteady flow separation within the glottis during phonation. Application to a modified two-mass model. *Journal of the Acoustical Society of America* 96, 6 (1994), 3416–3431.
- [29] QUARTERONI, A. Lecture notes from Euro summer school in simulation of fluid and structure interaction, 2001. Prague, Czech Republic.
- [30] ŠIDLOF, P. Numerical simulation of vibrations of an elastic body in flow and analysis of its stability (Numerické simulace kmitání pružného tělesa v proudící tekutině a analýza jeho stability, in Czech). Master's thesis, Czech Technical University in Prague, Faculty of Nuclear Sciences and Physical Engineering, 2003.
- [31] ŠIDLOF, P. Measurement of vibroacoustic properties of hydrogel lips for use in voice prostheses (Měření vibroakustických vlastností hydrogelových jazýčků pro použití v hlasivkových protézách, in Czech). Tech. Rep. Z 1363/05, Institute of Thermomechanics, Academy of Sciences of the Czech Republic, 2005.
- [32] ŠIDLOF, P., FRIC, M., VESELÝ, J., ŠVEC, J. G., ŠRAM, F., AND HORÁČEK, J. Videokymographic and acoustic analysis of vibration of silicone lips for use in tracheo-esophageal shunt valves. In *International Congress on Surgical and Prosthetic Rehabilitation after Laryngectomy* (Groningen, The Netherlands, 17 – 20 April 2005).
- [33] ŠIDLOF, P., AND HORÁČEK, J. Vocal fold motion and voice production: mathematical modelling and experiment. In *Proceedings of Forum Acusticum* (Budapest, Hungary, 29 August – 2 September 2005), pp. 2737–2742.
- [34] ŠIDLOF, P., ŠVEC, J. G., HORÁČEK, J., VESELÝ, J., KLEPÁČEK, I., AND HAVLÍK, R. Determination of vocal fold geometry from excised human larynges: Methodology and preliminary results. In *International Conference on Voice Physiology and Biomechanics* (Marseille, France, 18 – 20 August 2004).
- [35] STEIN, E., DE BORST, R., AND HUGHES, T. J., Eds. *Encyclopedia of Computational Mechanics*. John Wiley & Sons, Ltd., 2004, ch. 14 – Arbitrary Lagrangian-Eulerian Methods (by J. Donea, A. Huerta, J.-Ph. Ponthot and A. Rodríguez-Ferran).
- [36] STEINECKE, J., AND HERZEL, H. Bifurcations in an asymmetric vocal fold model. *Journal of the Acoustical Society of America* 97 (1995), 1874–1884.
- [37] STORY, B. H., AND TITZE, I. R. Voice simulation with a body-cover model of the vocal folds. *Journal of the Acoustical Society of America* 97 (1995), 1249–1260.
- [38] SVÁČEK, P., AND FEISTAUER, M. Application of a stabilized FEM to problems of aeroelasticity. In *The Fifth European Conference on Numerical Mathematics and Advanced Applications ENUMATH* (Berlin, Germany, 2003), Springer.

- [39] SVÁČEK, P., FEISTAUER, M., AND HORÁČEK, J. Numerical simulation of flow induced airfoil vibrations with large amplitudes. *Journal of Fluids and Structures* (2006). (in press).
- [40] SVÁČEK, P., AND HORÁČEK, J. On application of stabilized higher order finite element method on unsteady incompressible flow problems. In *The Sixth European Conference on Numerical Mathematics and Advanced Applications ENUMATH* (Santiago de Compostela, Spain, 2005), pp. 897–905.
- [41] ŠVEC, J. G., HORÁČEK, J., ŠRAM, F., AND VESELÝ, J. Resonance properties of the larynx: In vivo laryngoscopic investigation of the externally excited laryngeal vibrations. *Journal of the Acoustical Society of America* 108, 4 (2000), 1397–1407.
- [42] THOMSON, S. L., MONGEAU, L., AND FRANKEL, S. H. Aerodynamic transfer of energy to the vocal folds. *Journal of the Acoustical Society of America* 113 (2005), 1689–1700.
- [43] TITZE, I. R. The human vocal cords: A mathematical model, Part I. *Phonetica* 28 (1973).
- [44] TITZE, I. R. The human vocal cords: A mathematical model, Part II. *Phonetica* 29 (1974).
- [45] TITZE, I. R. *Principles of Voice Production*. National Center for Voice and Speech, Denver, 2000.
- [46] TITZE, I. R. *The myoelastic aerodynamic theory of phonation*. National Center for Voice and Speech, Denver, 2006.
- [47] TUREK, S. *Efficient solvers for incompressible flow problems : An algorithmic and computational approach*. Springer-Verlag, Berlin, 1999.